PHYSICS

ფიზიკა

40

PHYSICS
ფიზიკა

40

Publishing House "Meridian"
© გამომცემლობა "მერიდიანი", 2006

BOUND qqq-SYSTEMS IN THE FRAMEWORK OF THE DIFFERENT VERSIONS OF THE THREE-DIMENSIONAL REDUCTIONS OF THE BETHE-SALPETER EQUATION

T. Babutsidze, T. Kopaleishvili, D. Kurashvili, V. Skhirtladze

ABSTRACT. Three different versions of 3D-reduction of the Bethe-Salpeter equation for bound qqq-systems taking into account both two- and three-body interaction potentials has been considered. The normalization condition for wave function is derived. Using the solutions of non-relativistic limit of above mentioned equations with oscillator type two-particle potential as a basis, system of algebraic equations for expansion coefficients are obtained. Next it will be investigated the dependence of existence of the stable solutions of obtained system of equations on Lorentz (spin) structure of two- and three-quarks confining potentials.

1. INTRODUCTION

The properties of baryons in the framework of the constituent quark model (bound qqq-systems) at first stage were studied in non-relativistic approach. Exhaustive review of such an approach is given in [1] and will not be discussed below. The necessity of the relativistic treatment of bound qqq-systems is apparent (well known) for baryons ($N, \Sigma, \Lambda, \Xi, \Delta, \Omega$) with constituent quarks from light sector (u, d, s). The natural basis of such investigation is Bethe-Salpeter (BS) equation for three-fermion bound systems which were used e.g. in [2-11]. The main approximation used in the BS-equation is instantaneous (static) approximation for the kernel or its Lorentz-invariant version (null-plane approximation). Below it will be used the instantaneous approximation for the kernel of the BS-equation and some additional approximation for the free two-particle Green functions in the 3-particle system for the formulation two different

3

versions of the 3D-reduction of the BS-equation. These versions then will be compared to the Salpeter type versions formulated in [11].

2. THE 3D-REDUCTION OF BS-EQUATION FOR BOUND qqq-SYSTEMS AND NORMALIZATION CONDITION FOR CORRESPONDING WAVE FUNCTION

The BS-equation for bound qqq-systems has well-known form:

$$\varphi_P(p, q) = G_0(P; p, q) \int \frac{d^4 p'}{(2\pi)^4} \frac{d^4 q'}{(2\pi)^4} K(P; p, q; p', q') \varphi_P(p', q'), \quad (1)$$

where $P = P(\sqrt{M^2 + \vec{P}^2}, \vec{P})$ are total 4-momenta of the system under consideration and (p, q) are one of three equivalent pairs of Jacoby variables,

$$p_{ij} = \mu_{ji} p_i - \mu_{ij} p_j, \quad q_n = (\mu_i + \mu_j) p_n - \mu_n(p_i + p_j), \quad P = p_i + p_n,$$

$$\mu_i = \frac{m_i}{m_1 + m_2 + m_3}, \quad \mu_{ij} = \frac{m_i}{m_i + m_j}, \quad ijn = 123, \ 231, \ 312 = cycl(ijn), \quad (2)$$

$$p_i = \mu_i P + p_{ij} - \mu_{ij} q_n, \quad p_j = \mu_j P - p_{ij} - \mu_{ji} q_n, \quad p_n = \mu_n P + q_n;$$

$$G_0(P; p, q) = G_0(p_1) \otimes G_0(p_2) \otimes G_0(p_3) = G_{0ij}(P; p_{ij}, q_n) \otimes S_n(p_n),$$
$$\quad (3a)$$

$$S_j(p_l) = i(p_l \gamma_l - m_l)^{-1};$$

$$K(P; p, q; p', q') = K^{(3)}(P; p, q; p', q') + [K^{(2)}(P; p, q; p', q') =$$

$$= \sum_{cycl(ijn)} K_{ij}(p_i + p_j; p_{ij}, p'_{ij})(2\pi)^4 \delta(p_n - p'_n)(S_n(p_n))^{-1}]. \quad (3b)$$

4

For the 3D-reduction of the equation (1) the following approximations are used:

$$K^{(3)}(P; p, q; p', q') \rightarrow \tilde{K}^{(3)}(\tilde{p}, \tilde{q}; \tilde{p}', \tilde{q}') = -i\tilde{V}^{(3)}(\tilde{p}, \tilde{q}; \tilde{p}', \tilde{q}')$$

$$K_{ij}(p_i + p_j; p'_{ij}) \rightarrow \tilde{K}_{ij}(\tilde{p}_{ij}, \tilde{p}'_{ij}) = -i\tilde{V}_{ij}(\tilde{p}_{ij}, \tilde{p}'_{ij}), \quad (4)$$

i.e. the instantaneous approximation for the kernels corresponding to two- and three-body forces, and (c.m., $\tilde{P} = 0$)

$$G_{0ij}(M; p_{ij}, q_n) \rightarrow [G_{0ij}(M; p_{ij}, q_n) +$$

$$(G_{0ij}(M; p_i, p_j^{cr} = \mu_j M + p_0^0 - \mu_{ji} q_n^0, \tilde{p}_j) \equiv \quad (5)$$

$$\equiv G_{0ij}^{cr}(M; p_{ij}, q_n)]^{p_n^0 = m_n - \mu_n} = G_{0ijneff}(M; p_{ij}, \tilde{q}_n),$$

i.e. in the ij free-particle Green function before two-body interaction potential the third (non-interacting) particle (n) is taken on mass-shell suggested in [12] and used in [10], where the 3D-reduction of BS-equation without three-body force and G_{0ij}^{cr} term was formulated. Below term this version will be mentioned as the IKLR version. Then the additional term G_{0ij}^{cr} in (5) (suggested and used in [13] for the 3D-reduction of BS-equation for bound $q\bar{q}$ system) will be called as the IKLR+MW version.

Now using the approximation (4) and (5) after integrating over p_0 and q_0 the BS-equation (1) for the wave function

$$\tilde{\varphi}_M(\tilde{p}, \tilde{q}) = \int \frac{dp_0}{2\pi} \frac{dq_0}{2\pi} \varphi_0(p, q), \quad (6)$$

we obtain the equation

5

$$\bar{\Phi}_M(\bar{p}, \bar{q}) = \int \frac{d^3 \bar{p}'}{(2\pi)^3} \frac{d^3 \bar{q}'}{(2\pi)^3} \bar{G}_0(M; \bar{p}, \bar{q}) \bar{V}^{(3)}(\bar{p}, \bar{q}; \bar{p}', \bar{q}') \bar{\Phi}_M(\bar{p}', \bar{q}') +$$

$$+ \sum_{cycl(ijn)} \int \frac{d\bar{p}'}{(2\pi)^3} \frac{d\bar{q}'}{(2\pi)^3} \bar{G}_{0ijneff}(M; \bar{p}, \bar{q}) \bar{V}_{ij}(\bar{p}, \bar{q}; \bar{p}', \bar{q}') \bar{\Phi}_M(\bar{p}', \bar{q}'),$$

(7)

where

$$\bar{G}_0(M; \bar{p}, \bar{q}) = \left[\frac{\Lambda_{123}^{(+++)}(\bar{p}, \bar{q})}{M - \omega_1 - \omega_2 - \omega_3 + i0} + \right.$$

$$\left. + \frac{\Lambda_{123}^{(---)}(\bar{p}, \bar{q})}{M + \omega_1 + \omega_2 + \omega_3} \right] \gamma_1^0 \otimes \gamma_2^0 \otimes \gamma_3^0,$$

(8)

$$\bar{G}_{0ijneff}(M; \bar{p}, \bar{q}) = \left[\left(\frac{\Lambda_{ij}^{(++)}(\bar{p}, \bar{q})}{M - \omega_n - (\omega_i + \omega_j) + i0} - \right. \right.$$

$$\left. - \frac{\Lambda_{ij}^{(--)}(\bar{p}, \bar{q})}{M - \omega_n + \omega_i + \omega_j - i0} + \frac{\Lambda_{ij}^{(-+)}(\bar{p}, \bar{q})}{(\mu_{ji} - \mu_{ij})(M - \omega_n) + \omega_i + \omega_j + i0} + \right.$$

$$\left. + \frac{\Lambda_{ij}^{(+-)}(\bar{p}, \bar{q})}{(\mu_{ij} - \mu_{ji})(M - \omega_n) + \omega_i + \omega_j + i0} \right) \right] \gamma_i^0 \otimes \gamma_j^0 \otimes I_n,$$

(9)

$$\Lambda_{123}^{(\alpha_1 \alpha_2 \alpha_3)} = \Lambda_1^{(\alpha_1)} \otimes \Lambda_2^{(\alpha_2)} \otimes \Lambda_3^{(\alpha_3)},$$

$$\Lambda_{ij}^{(\alpha_i \alpha_j)} = \Lambda_i^{(\alpha_i)} \otimes \Lambda_j^{(\alpha_j)}, \quad \Lambda_i^{(\alpha_i)} = \frac{\omega_i + \alpha_i h_i}{2\omega_i},$$

(10)

$$h_i = \gamma_i^0 (\bar{\gamma}_i \bar{p} + m_i).$$

6

Note that the first term in (9) corresponds to the IKLR version, as to the additional term in (9) appears in the IKLR+MW version.

For derivation of the normalization condition for the wave function $\tilde{\varphi}_M(\tilde{p},\tilde{q})$ in the IKLR and IKLR+MW versions we use the procedure suggested in [10]. We begin with the equation for total Green operator

$$G(P) = G_0(P) + G_0(P)[K(P) = K^{(3)}(P) + K^{(2)}(P)]G(P), \quad (11)$$

from which in (4) and (5) approximations it follows the equation for the Green's operator in 3D-space (c.m.)

$$\tilde{G}(M) = i\tilde{G}_0(M) + \left[i\tilde{G}_0(M)\tilde{K}^{(3)}(M) + \right.$$

$$\left. + \sum_{cycl(ijn)} i\tilde{G}_{0ijneff}(M)\tilde{K}_{ij}^{(2)}(M) \right] \tilde{G}(M). \quad (12)$$

This equation can be rewritten as

$$\tilde{G} = ig_0\Pi_+\Gamma^0 + g_0\tilde{U}\tilde{G}, \quad (13)$$

where

$$g_0 = [M - (h_1 + h_2 + h_3)]^{-1}, \ \Gamma^0 = \gamma_1^0 \otimes \gamma_2^0 \otimes \gamma_3^0, \ \Pi_+ = \Lambda_{123}^{(+++)} + \Lambda_{123}^{(---)}, \quad (14)$$

$$\tilde{U} = g_0^{-1}\left[\tilde{G}_0\tilde{V}^{(3)} + \sum_{cycl(ijn)} \tilde{G}_{0ijneff}(M)\tilde{V}_{ij} \right]. \quad (15)$$

Then the equation (7) can be written in the vector form (c.m.):

$$|\tilde{\varphi}_M\rangle = g_0\tilde{U}|\tilde{\varphi}_M\rangle. \quad (16)$$

7

Now it can be easily checked that if Green's operator satisfies the equation (13), then the following relation holds:

$$\hat{G}\Gamma^0\Pi_+[\hat{g}_0^{-1}-\tilde{U}]\hat{G}\Gamma^0\Pi_+\Gamma^0 = i\hat{G}\Gamma^0\Pi_+\Gamma^0. \qquad (17)$$

Noting that the equation (13) holds for arbitrary reference frame $P=(P_0,\vec{P})$, the Green operator $\hat{G}(P)$ has the following representation:

$$\hat{G} = i\sum_M \frac{\left|\bar{\tilde{\varphi}}_M\right\rangle\langle\bar{\tilde{\varphi}}_M|}{P_0^2-M_M^2+i0} + \hat{R}, \ \langle\bar{\tilde{\varphi}}_M\right| = \langle\tilde{\varphi}_M|\Gamma^0. \qquad (18)$$

Substituting this expression in the relation (17) after extracting the bound state poles in the operator $\hat{G}$, the following condition can be obtained (c.m.):

$$\left\langle\bar{\tilde{\varphi}}_M\right|\Pi_+[1-\frac{\partial}{\partial M}\tilde{U}(M)]\left|\tilde{\varphi}_M\right\rangle = 2M, \qquad (19)$$

which is normalization condition for the wave function $\tilde{\varphi}_M(\vec{p},\vec{q})$ satisfying equation (7).

3. 3D-EQUATIONS FOR THE "FREQUENCY COMPONENTS" OF THE WAVE FUNCTION AND CORRESPONDING NORMALIZATION CONDITION

Introducing the "frequency components" of wave function

$$\tilde{\varphi}_M^{(\sigma_1\sigma_2\sigma_3)}(\vec{p},\vec{q}) = \Lambda_{123}^{(\sigma_1\sigma_2\sigma_3)}\tilde{\varphi}_M(\vec{p},\vec{q}), \qquad (20a)$$

and taking into account the relation

8

$$\sum_{\alpha_1\alpha_2\alpha_3} \tilde{\varphi}_M^{(\alpha_2\alpha_3)}(\bar{p}, \bar{q}) = \tilde{\varphi}_M(\bar{p}, \bar{q}), \tag{20b}$$

from (7) equation it can be obtained the following system of equations

$$[M \mp (\omega_1 + \omega_2 + \omega_3)]\tilde{\varphi}_M^{(\pm\pm\pm)}(\bar{p}, \bar{q}) =$$

$$= \sum_{\alpha'_2\alpha'_3\alpha'_1} \int \frac{d^3\bar{p}'}{(2\pi)^3} \frac{d^3\bar{q}'}{(2\pi)^3} \Lambda_{123}^{(\pm\pm\pm)}(\bar{p}, \bar{q})\{\gamma_1^0 \otimes \gamma_2^0 \gamma_3^0 \hat{V}^{(1)}(\bar{p}, \bar{q}; \bar{p}', \bar{q}') +$$

$$+ \sum_{cycl(ijm)} \left[-(1 + \frac{2\omega_n}{M + \omega_i + \omega_j - \omega_m} \equiv f_{ijn}(M; \bar{p}, \bar{q})) \right] \times \tag{21a}$$

$$\times \gamma_i^0 \otimes \gamma_j^0 \hat{V}_{ij}^{(2)}(\bar{p}, \bar{q}; \bar{p}', \bar{q}') \} \tilde{\varphi}_M^{(\alpha'_2\alpha'_3\alpha'_1)}(\bar{p}', \bar{q}');$$

$$[M \mp (\omega_1 + \omega_2) - \omega_3)]\tilde{\varphi}_M^{(\pm\pm+)}(\bar{p}, \bar{q}) =$$

$$= \sum_{\alpha'_2\alpha'_3\alpha'_1} \int \frac{d^3\bar{p}'}{(2\pi)^3} \frac{d^3\bar{q}'}{(2\pi)^3} \Lambda_{123}^{(\pm\pm+)}(\bar{p}, \bar{q})(\pm1)\left\{\gamma_1^0 \otimes \gamma_2^0 \hat{V}_{12}(\bar{p}, \bar{q}; \bar{p}', \bar{q}') + \right.$$

$$[M \mp (\omega_1 + \omega_2) - \omega_3)] \times \left[\frac{\gamma_2^0 \otimes \gamma_3^0 \hat{V}_{23}(\bar{p}, \bar{q}; \bar{p}', \bar{q}')}{(\mu_{23} - \mu_{23})(M - \omega_1) \pm (\omega_2 + \omega_3) + i0} + \right. \tag{21b}$$

$$\left. \times \frac{\gamma_3^0 \otimes \gamma_1^0 \hat{V}_{31}(\bar{p}, \bar{q}; \bar{p}', \bar{q}')}{(\mu_{31} - \mu_{13})(M - \omega_2) \pm (\omega_3 + \omega_1) - i0} \right] \tilde{\varphi}_M^{(\alpha'_2\alpha'_3\alpha'_1)}(\bar{p}', \bar{q}');$$

$$[M \mp (\omega_2 + \omega_3) - \omega_1)]\tilde{\varphi}_M^{(\mp\pm\pm)}(\bar{p}, \bar{q}) =$$

$$= \sum_{\alpha'_2\alpha'_3\alpha'_1} \int \frac{d^3\bar{p}'}{(2\pi)^3} \frac{d^3\bar{q}'}{(2\pi)^3} \Lambda_{123}^{(\mp\pm\pm)}(\bar{p}, \bar{q})(\pm1)\{\gamma_2^0 \otimes \gamma_3^0 \hat{V}_{23}(\bar{p}, \bar{q}; \bar{p}', \bar{q}') +$$

$$+[M \mp (\omega_2 + \omega_3) - \omega_1] \times \left[\frac{\gamma_3^0 \otimes \gamma_1^0 \hat{V}_{31}(\bar{p}, \bar{q}; \bar{p}', \bar{q}')}{(\mu_{13} - \mu_{31})(M - \omega_3) \pm (\omega_3 + \omega_1) + i0} + \right.$$

$$\left. + \frac{\gamma_1^0 \otimes \gamma_2^0 \hat{V}_{12}(\bar{p}, \bar{q}; \bar{p}', \bar{q}')}{(\mu_{12} - \mu_{21})(M - \omega_3) \pm (\omega_1 + \omega_2) - i0} \right] \right\} \bar{\varphi}_M^{(\alpha_1'\alpha_2'\alpha_3')}(\bar{p}', \bar{q}'). \tag{21c}$$

$$[M \mp (\omega_1 + \omega_3) - \omega_2] \bar{\varphi}_M^{(\pm\pm\pm)}(\bar{p}, \bar{q}) =$$

$$= \sum_{\alpha_1'\alpha_2'\alpha_3'} \int \frac{d^3\bar{p}'}{(2\pi)^3} \frac{d^3\bar{q}'}{(2\pi)^3} \Lambda_{123}^{(\pm\pm\pm)}(\bar{p}, \bar{q})(\pm1)\{\gamma_3^0 \otimes \gamma_1^0 \hat{V}_{31}(\bar{p}, \bar{q}; \bar{p}', \bar{q}')$$

$$+[M \mp (\omega_1 + \omega_3) - \omega_2] \times \left[\frac{\gamma_1^0 \otimes \gamma_2^0 \hat{V}_{12}(\bar{p}, \bar{q}; \bar{p}', \bar{q}')}{(\mu_{21} - \mu_{12})(M - \omega_3) \pm (\omega_1 + \omega_2) + i0} + \right.$$

$$\left. + \frac{\gamma_2^0 \otimes \gamma_3^0 \hat{V}_{23}(\bar{p}, \bar{q}; \bar{p}', \bar{q}')}{(\mu_{23} - \mu_{32})(M - \omega_3) \pm (\omega_2 + \omega_3) - i0} \right] \right\} \bar{\varphi}_M^{(\alpha_1'\alpha_2'\alpha_3')}(\bar{p}', \bar{q}'). \tag{21d}$$

Now the normalization condition (19) takes the form:

$$\int \frac{d^3\bar{p}}{(2\pi)^3} \frac{d^3\bar{q}}{(2\pi)^3} \left[\left| \bar{\varphi}_M^{(+++)}(\bar{p}, \bar{q}) \right|^2 + \left| \bar{\varphi}_M^{(---)}(\bar{p}, \bar{q}) \right|^2 \right] -$$

$$- \int \frac{d^3\bar{p}}{(2\pi)^3} \frac{d^3\bar{q}}{(2\pi)^3} \frac{d^3\bar{p}'}{(2\pi)^3} \frac{d^3\bar{q}'}{(2\pi)^3} \sum_{cycl(ijn)} \left[\frac{\partial f_{ijm}(M; \bar{p}, \bar{q})}{\partial M} \times \right.$$

$$\left. \times \bar{\varphi}_M^{+(---)}(\bar{p}, \bar{q}) \Lambda_{123}^{(---)}(\bar{p}, \bar{q}) \hat{V}_{ij}(\bar{p}, \bar{q}; \bar{p}', \bar{q}') \sum_{\alpha_1'\alpha_2'\alpha_3'} \bar{\varphi}_M^{(\alpha_1'\alpha_2'\alpha_3')}(\bar{p}', \bar{q}') = \right] = 2M. \tag{22}$$

Note that the Salpeter type equation derived in the [11] from 3D-reduction of BS-equation (LKMP version) can be obtained from the equation (21a) if $f_{ijn} \to 1$ and put $(\alpha'_1\alpha'_2\alpha'_3) = (\pm\pm\pm)$, i.e. the components $\widehat{\varphi}_M^{(+++)}$, $\widehat{\varphi}_M^{(\pm\mp\pm)}$, $\widehat{\varphi}_M^{(\mp\mp\mp)}$ are zeros. As to corresponding normalization condition for the wave function it follows from (22) putting $f_{ijn} = 1$.

Now we represent function $\widehat{\varphi}_M^{(\alpha_1\alpha_2\alpha_3)}(\bar{p}, \bar{q})$ as

$$\widehat{\varphi}_M^{(\alpha_1\alpha_2\alpha_3)}(\bar{p}, \bar{q}) = N_{123}^{(\alpha_1\alpha_2\alpha_3)}(\bar{p}, \bar{q}) \prod_{i=1}^{3} \left(\frac{1}{\omega_i} \frac{\alpha_i \bar{\sigma}_i \bar{p}_i}{\omega_i + \alpha_i m_i}\right) \chi_M^{(\alpha_1\alpha_2\alpha_3)}(\bar{p}, \bar{q}), \quad (23)$$

$$N_{123}^{(\alpha_1\alpha_2\alpha_3)}(\bar{p}, \bar{q}) = \prod_{i=1}^{3} \sqrt{\frac{\omega_i + \alpha_i m_i}{2\omega_i}}$$

and the Lorentz structure of the three-body confining interaction potential we take the form [14]:

$$\hat{\mathcal{V}}^{(3)} = \nu_0^{(3)} L_+ + \left\{\begin{array}{c} L_- \\ L_+ \end{array}\right\} \nu_c^{(3)}, \qquad \begin{array}{l} \text{model A} \\ \text{model B} \end{array} \quad (24a)$$

where

$$\nu_0^{(3)} = 3a, \qquad L_{\mp} = \left\{\begin{array}{c} 1/2 \\ 1/4 \end{array}\right\} (\mp I_1 \otimes I_2 \otimes I_3 + \sum_{cycl(ijn)} \gamma_i^0 \otimes \gamma_j^0 \otimes I_n)$$

and a is negative constant, $\nu_c^{(3)}$ is increasing positive function of quarks coordinates.

As to the two-body interaction operator it is taken in the form given in the review paper [15] concerning bound $q\bar{q}$-systems problem:

$$\hat{V}_{ij} = \gamma_i^0 \otimes \gamma_j^0 V_{ij}^{vg} + [x\gamma_i^0 \otimes \gamma_j^0 + (1-x) I_i \otimes I_j] V_{ij}^c +$$

11

$$+[I_i \otimes I_j + r_i^5 \otimes r_j^5]V_{ij}^T, \quad 0 \le x \le 1, \tag{24b}$$

where "og", "c" and "T" means "one gluon", "confinement" and "t-Hooft", accordingly.

Then the system of equations for wave functions $\chi_M^{(\alpha_i^{'}\alpha_2'\alpha_3')}(\bar{p}, \bar{q})$ can be obtained from the equations (21) and has the form:

$$[M \mp (\omega_1 + \omega_2 + \omega_3)]\chi_M^{\pm\pm\pm}(\bar{p}, \bar{q}) =$$

$$= \int \frac{d^3\bar{p}'}{(2\pi)^3} \frac{d^3\bar{q}'}{(2\pi)^3} \left[\sum_{\alpha_2'\alpha_3'} V_{eff}^{(1)(\pm\pm\pm;\alpha_1'\alpha_2'\alpha_3')}(\bar{p}, \bar{q}; \bar{p}', \bar{q}') \chi_M^{(\alpha_1'\alpha_2'\alpha_3')}(\bar{p}', \bar{q}') + \right.$$

$$+ \sum_{cycl(ijn)} \left[\frac{1}{-f_{ijn}(M; \bar{p}, \bar{q})} \right] \times$$

$$\left. \times \sum_{\alpha_i'\alpha_3'} V_{ijeff}^{(\pm\pm;\alpha_i'\alpha_3')}(\bar{p}, \bar{q}; \bar{p}', \bar{q}') \chi_M^{(\alpha_i'\alpha_n'=\pm)}(\bar{p}', \bar{q}') \right]; \tag{25a}$$

$$[M \mp (\omega_1 + \omega_2 - \omega_3)]\chi_M^{\pm\pm\mp}(\bar{p}, \bar{q}) =$$

$$= \int \frac{d^3\bar{p}'}{(2\pi)^3} \frac{d^3\bar{q}'}{(2\pi)^3} (\pm 1) \left\{ \sum_{\alpha_2'\alpha_3'} V_{12eff}^{(\pm\mp;\alpha_2'\alpha_3')}(\bar{p}, \bar{q}; \bar{p}', \bar{q}') \chi_M^{(\pm\pm\mp)}(\bar{p}', \bar{q}') + \right.$$

$$+[M \mp (\omega_1 + \omega_2) - \omega_3] \left[\sum_{\alpha_2'\alpha_3'} \frac{V_{23eff}^{(\pm\mp;\alpha_2'\alpha_3')}(\bar{p}, \bar{q}; \bar{p}', \bar{q}')}{(\mu_{32} - \mu_{23})(M - \omega_1) \pm (\omega_2 + \omega_3) - i0} \chi_M^{(\pm\pm\mp)}(\bar{p}', \bar{q}') + \right.$$

$$\left. \left. + \sum_{\alpha_2'\alpha_3'} \frac{V_{31eff}^{(\mp\pm;\alpha_2'\alpha_3')}(\bar{p}, \bar{q}; \bar{p}', \bar{q}')}{(\mu_{31} - \mu_{13})(M - \omega_2) \pm (\omega_3 + \omega_1) + i0} \chi_M^{(\alpha_1'\pm\pm\mp)}(\bar{p}', \bar{q}') \right] \right\}; \tag{25b}$$

$$[M \mp (\omega_2 + \omega_3) - \omega_1]\chi_M^{\mp\pm\pm}(\bar{p}, \bar{q}) =$$

$$= \int \frac{d^3\vec{p}'}{(2\pi)^3} \frac{d^3\vec{q}'}{(2\pi)^3} (\pm 1) \Bigg\{ \sum_{\alpha_2'\alpha_1'} V_{23eff}^{(\pm\pm\alpha_2'\alpha_1')}(\vec{p}, \vec{q}; \vec{p}', \vec{q}') \chi_M^{(\mp\alpha_2'\alpha_1')}(\vec{p}', \vec{q}') +$$

$$+ [M \mp (\omega_2 + \omega_3) - \omega_1)] \Bigg[\sum_{\alpha_2'\alpha_1'} \frac{V_{12eff}^{(\pm\pm\alpha_2'\alpha_1')}(\vec{p}, \vec{q}; \vec{p}', \vec{q}') \chi_M^{(\alpha_2'\pm\alpha_1')}(\vec{p}', \vec{q}')}{(\mu_{12} - \mu_{21})(M - \omega_3) \pm (\omega_1 + \omega_2) + i0} +$$

$$+ \sum_{\alpha_2'\alpha_1'} \frac{V_{31eff}^{(\pm\mp\alpha_2'\alpha_1')}(\vec{p}, \vec{q}; \vec{p}', \vec{q}') \chi_M^{(\alpha_1'\pm\alpha_2')}(\vec{p}', \vec{q}')}{(\mu_{13} - \mu_{31})(M - \omega_2) \pm (\omega_3 + \omega_1) - i0} \Bigg] \Bigg\}; \qquad (25c)$$

$$[M \mp (\omega_1 + \omega_3) - \omega_2)] \chi_M^{(\mp\mp\pm)}(\vec{p}, \vec{q}) =$$

$$= \int \frac{d^3\vec{p}'}{(2\pi)^3} \frac{d^3\vec{q}'}{(2\pi)^3} (\pm 1) \Bigg\{ \sum_{\alpha_2'\alpha_1'} V_{13eff}^{(\pm\pm\alpha_2'\alpha_1')}(\vec{p}, \vec{q}; \vec{p}', \vec{q}') \chi_M^{(\alpha_2'\mp\alpha_1')}(\vec{p}', \vec{q}') +$$

$$+ [M \mp (\omega_1 + \omega_3) - \omega_2)] \Bigg[\sum_{\alpha_2'\alpha_1'} \frac{V_{12eff}^{(\mp\pm\alpha_2'\alpha_1')}(\vec{p}, \vec{q}; \vec{p}', \vec{q}') \chi_M^{(\alpha_2'\mp\alpha_1')}(\vec{p}', \vec{q}')}{(\mu_{12} - \mu_{21})(M - \omega_3) \pm (\omega_1 + \omega_2) - i0} +$$

$$+ \sum_{\alpha_2'\alpha_1'} \frac{V_{23eff}^{(\pm\pm\alpha_2'\alpha_1')}(\vec{p}, \vec{q}; \vec{p}', \vec{q}') \chi_M^{(\pm\alpha_2'\alpha_1')}(\vec{p}', \vec{q}')}{(\mu_{23} - \mu_{32})(M - \omega_1) \pm (\omega_2 + \omega_3) - i0} \Bigg] \Bigg\}, \qquad (25d)$$

where

$$V_{eff}^{(3)(\pm\pm\pm,\alpha_2'\alpha_1')}(\vec{p}, \vec{q}; \vec{p}', \vec{q}') =$$

$$= N_{123}^{(\pm\pm)}(\vec{p}, \vec{q}) [\nu_0^{(3)}(\vec{p}, \vec{q}; \vec{p}', \vec{q}') B_+^{(\pm\pm\pm,\alpha_2'\alpha_1')}(\vec{p}, \vec{q}; \vec{p}', \vec{q}') +$$

13

$$+ \left\{ \begin{matrix} B_{+}^{(\pm\pm\pm,\alpha'\alpha'_2\alpha'_3)}(\bar{p},\ \bar{q};\ \bar{p}',\ \bar{q}') \\ B_{+}^{(\pm\pm\pm,\alpha'\alpha'_2\alpha'_3)}(\bar{p},\ \bar{q};\ \bar{p}',\ \bar{q}') \end{matrix} \right\} v_{c}^{(3)}(\bar{p},\ \bar{q};\ \bar{p}',\ \bar{q}') N_{123}^{(\alpha'\alpha'_2\alpha'_3)}(\bar{p}',\bar{q}'), \quad \begin{matrix} A \\ B \end{matrix}$$

$$\tag{26a}$$

$$V_{ij,eff}^{(\alpha_i\alpha'_j)}(\bar{p},\ \bar{q};\ \bar{p}',\ \bar{q}') =$$

$$= N_{ij}^{(\alpha_i\alpha_j)}(\bar{p},\ \bar{q})[\ _1V_{ij}(\bar{p},\ \bar{q};\ \bar{p}',\ \bar{q}')\ _1B_{ij}^{(\alpha_i\alpha_j,\alpha'\alpha'_j)}(\bar{p},\ \bar{q};\ \bar{p}',\ \bar{q}') +$$

$$+\ _2V_{ij}(x;\ \bar{p},\ \bar{q};\ \bar{p}',\ \bar{q}')\ _2B_{ij}^{(\alpha_i\alpha_j,\alpha'\alpha'_j)}(\bar{p},\ \bar{q};\ \bar{p}',\ \bar{q}') + \quad \tag{26b}$$

$$+\ _TV_{ij}(\bar{p},\ \bar{q};\ \bar{p}',\ \bar{q}')\ _TB_{ij}^{(\alpha_i\alpha_j,\alpha'\alpha'_j)}(\bar{p},\ \bar{q};\ \bar{p}',\ \bar{q}')]N_{ij}^{(\alpha'\alpha'_j)}(\bar{p}',\bar{q}'),$$

$$_1V = V^{og} + V^c, \quad\quad _2V(x) = V^{og} + (2x-1)V^c,$$

$$B_{+}^{(\pm\pm\pm,\alpha'\alpha'_2\alpha'_3)}(\bar{p},\ \bar{q};\ \bar{p}',\ \bar{q}') =$$

$$= 1 + \sum_{i=1}^{3} f_i^{(\pm)} f_i^{(\alpha'_i)\gamma} - \sum_{i<j=1}^{3} f_i^{(\pm)} f_j^{(\pm)} f_i^{(\alpha'_i)\gamma} f_j^{(\alpha'_j)\gamma} - \prod_{i=1}^{3} f_i^{(\pm)} f_i^{(\alpha'_i)\gamma},$$

$$\tag{26c}$$

$$B_{+}^{(\pm\pm\pm,\alpha'\alpha'_2\alpha'_3)}(\bar{p},\ \bar{q};\ \bar{p}',\ \bar{q}') =$$

$$= 1 - \prod_{i=1}^{3} f_i^{(\pm)} f_i^{(\alpha'_i)\gamma}, \quad f_i^{(\alpha_i)} = \frac{\alpha_i \bar{\sigma}_i \bar{p}_i}{\omega_i + \alpha_i m_i}, \quad f_i^{(\alpha'_i)\gamma} = \frac{\alpha'_i \bar{\sigma}_i \bar{p}'_i}{\omega'_i + \alpha_i m_i},$$

$$_1B_{ij}^{(\alpha_i\alpha_j,\alpha'\alpha'_j)}(\bar{p},\ \bar{q};\ \bar{p}',\ \bar{q}') = 1 + f_i^{(\pm)} f_i^{(\alpha'_i)\gamma} f_j^{(\pm)} f_j^{(\alpha'_j)\gamma},$$

$$_2B_{ij}^{(\alpha_i\alpha_j,\alpha'\alpha'_j)}(\bar{p},\ \bar{q};\ \bar{p}',\ \bar{q}') = f_i^{(\alpha_i)} f_i^{(\alpha'_i)\gamma} + f_j^{(\alpha_j)} f_j^{(\alpha'_j)\gamma}, \quad \tag{26d}$$

$$_TB_{ij}^{(\alpha_i\alpha_j,\alpha'\alpha'_j)}(\bar{p},\ \bar{q};\ \bar{p}',\ \bar{q}') =$$

$$= (1 + f_i^{(\alpha_i)} f_j^{(\alpha_j)})(1 + f_i^{(\alpha_i')} f_j^{(\alpha_j')}) - (f_i^{(\alpha_i)} + f_j^{(\alpha_j)})(f_i^{\alpha_i')} + f_j^{\alpha_j')})_.$$

As to the normalization condition for the functions $\chi_M^{(\alpha_1\alpha_2\alpha_3)}(\bar{p}, \bar{q})$ it can be obtained from the condition (22) substituting (23) expression. As a result we have:

$$\int \frac{d^3\bar{p}}{(2\pi)^3} \frac{d^3\bar{q}}{(2\pi)^3} \sum_{\alpha = +,-} \left| \chi_M^{(\alpha\alpha\alpha)}(\bar{p}, \bar{q}) \right|^2 -$$

$$- \sum_{\alpha_1'\alpha_2'\alpha_3' \, cycl(ijn)} \int \frac{d^3\bar{p}'}{(2\pi)^3} \frac{d^3\bar{q}'}{(2\pi)^3} \frac{d^3\bar{p}}{(2\pi)^3} \frac{d^3\bar{q}}{(2\pi)^3} [\chi_M^{*(---)}(\bar{p}, \bar{q}) \frac{\partial f_{jn}(M; \bar{p}, \bar{q})}{\partial M}$$

$$\times V_{ij,eff}^{(---\alpha_1'\alpha_2'\alpha_3')}(\bar{p}, \bar{q}; \bar{p}', \bar{q}') \chi_M^{(\alpha_1'\alpha_2'\alpha_3')}(\bar{p}', \bar{q}')] = 2M, \qquad (27)$$

from which it follows the normalization condition for the LKMP version of 3D-reduction of BS-equation if $f_{jn} \to 1$.

4. THE SOLUTION PROCEDURE FOR OBTAINED EQUATION

Main problem which must be considered below is dependence of existence of the stable solution of the system of equations (25) on Lorentz structure of the two and three quarks confining interaction potentials. For this (ij) quarks confining interaction potential is taken in the form used in [16] for investigation mass spectra of bound $q\bar{q}$ systems

$$\mathcal{V}_{ij}(\bar{r}_i, \bar{r}_j) = -a_{ij} + b_{ij} |r_i - r_j|^2, \qquad (28a)$$

$$a_{ij} = \frac{2}{3}\alpha_S(m_{ij}^2)V_0, \ b_{ij} = \frac{2}{3}\alpha_S(m_{ij}^2)\frac{m_i m_j}{2m_{ij}}, \ \alpha_S(m_{ij}^2) =$$

15

$$= \frac{12\pi}{33 - 2n_f} \left(\ln \frac{m_{ij}^2}{\Lambda^2} \right)^{-1}, \quad m_{ij} = m_i + m_j \qquad (28)$$

with free parameters: ω_0, Λ and n_f (number of flavours). Note that $\frac{2}{3}$ appearing in a_{ij} and b_{ij} instead of $\frac{4}{3}$ for $q\bar{q}$ systems is related to color depending part of wave function. As to three-quark confining interaction potential $v_c^{(3)}$ we take the form suggested in [14], but instead of linear type interaction we use oscillator type interaction

$$v_c^{(3)}(\vec{r}_1, \ \vec{r}_2, \ \vec{r}_3) = b\big(|\vec{r}_1 - \vec{r}_2|^2 + |\vec{r}_2 - \vec{r}_3|^2 + |\vec{r}_3 - \vec{r}_1|^2\big), \qquad (29)$$

which is practically more easily solvable and compatible with two-body model.

Below we consider bound qqq -systems with $m_1 = m_2 = m$, which included all observable baryons mentioned in the introduction N, Σ, Λ, Ξ, Δ, Ω and use variables $\vec{p} = \vec{p}_{12}$, $\vec{q} = \vec{q}_3 = \vec{p}_3$ (c.m.). Then in the momentum space from (28a) and (29) we have:

$$\mathcal{Y}_{ij}(\vec{p}, \ \vec{q}; \ \vec{p}', \ \vec{q}') = -(2\pi)^6 \left\{ a_{ij} + b_{ij} \left(\left(\frac{1}{4} + \frac{3}{4} \delta_{(ij)}^{(12)} \right) \frac{\partial}{\partial \vec{p}'} \frac{\partial}{\partial \vec{p}'} + \right. \right.$$

$$+ (1 - \delta_{(ij)}^{(12)}) \left[\frac{\partial}{\partial \vec{q}'} \frac{\partial}{\partial \vec{q}'} + \frac{1}{2} (-)^{i+j+1} \left(\frac{\partial}{\partial \vec{p}'} \frac{\partial}{\partial \vec{q}'} + \right. \right.$$

$$\left. \left. \left. + \frac{\partial}{\partial \vec{q}'} \frac{\partial}{\partial \vec{p}'} \right) \right] \right) \right\} \delta^{(3)}(\vec{p} - \vec{p}') \delta^{(3)}(\vec{q} - \vec{q}'), \qquad (30a)$$

$$v_c^{(3)}(\vec{p}, \ \vec{q}; \ \vec{p}', \ \vec{q}') =$$

16

$$= -(2\pi)^4 b \left\{ \frac{3}{2} \frac{\partial}{\partial \vec{p}'} \frac{\partial}{\partial \vec{p}'} + 2 \frac{\partial}{\partial \vec{q}'} \frac{\partial}{\partial \vec{q}'} \right\} \delta^{(3)}(\vec{p} - \vec{p}') \delta^{(3)}(\vec{q} - \vec{q}'), \quad (30b)$$

$$v_0^{(3)}(\vec{p}, \vec{q}; \ \vec{p}', \ \vec{q}') = (2\pi)^4 3 a \delta^{(3)}(\vec{p} - \vec{p}') \delta^{(3)}(\vec{q} - \vec{q}').$$

If we put the expressions (30a,b) in the right side of the systems of equations (25) then there will appear the following type of integrals:

$$I(\vec{c}, \ \vec{d}) = \int \frac{\partial}{\partial \vec{c}'} \frac{\partial}{\partial \vec{d}'} \{\delta^{(3)}(\vec{c} - \vec{c}') \delta^{(3)}(\vec{d} - \vec{d}') B(\vec{c}, \ \vec{d}; \ \vec{c}', \ \vec{d}') \times$$

$$\times N(\vec{c}', \ \vec{d}') \chi_M(\vec{c}', \ \vec{d}') \} d^3\vec{c}' d^3\vec{d}', \quad (31a)$$

which taking into account the boundary condition for the bound state wave functions $\chi(c_{x,y,z}, \ d_{x,y,z} = \pm\infty) = 0$ are reduced expression:

$$I(\vec{c}, \ \vec{d}) = \frac{\partial}{\partial \vec{c}'} \frac{\partial}{\partial \vec{d}'} B(\vec{c}, \ \vec{d}; \ \vec{c}', \ \vec{d}') N(\vec{c}', \ \vec{d}') \chi_M(\vec{c}', \ \vec{d}') \Big|_{\vec{d}' = \vec{d}}^{\vec{c}' = \vec{c}} \quad (31b)$$

As a result the second system of equation (25) will be reduced to the system of the second order differential equations (nonlinear over M) for wave functions $\chi_M^{(a_1 a_2 a_3)}(\vec{p}', \ \vec{q}')$.

For the wave functions we use the partial wave expansion:

$$\chi_M^{(a_1 a_2 a_3)}(\vec{p}, \ \vec{q}) =$$

$$= \sum_{l_p l_q L S_{12} S J M_J} \left\langle \hat{p}, \ \hat{q} \middle| (l_p l_q \frac{1}{2}) L (S_{12} \frac{1}{2}) S J M_J \right\rangle_M R_{l_p l_q S_{12}}^{(a_1 a_2 a_3) L S J}(p, q), \quad (32)$$

where l_p and l_q are orbital momenta corresponding to moments $\vec{p}$ and $\vec{q}$, respectively, S_{12} is total spin for the two particles system

17

(12), L and S are total orbital momenta and spin of the system (123). As a result from above mentioned system of differential equations for the function $\chi_M^{(\alpha_1\alpha_2\alpha_3)}(\bar{p}, \bar{q})$ it can be obtained the system of differential equations for radial wave functions $_M R_{l_p l_q S_{12}}^{(\alpha_1\alpha_2\alpha_3)LSJ}(p, q)$.

For calculation of the mass spectrum of bound (u, d, s) quark systems $(N, \Sigma, \Lambda, \Xi, \Delta, \Omega)$ baryons) we will use the solutions of the differential equations obtained from system of equations (21a,b) in the non-relativistic limit. For this reason it must be used the approximations:

$$\omega_i \rightarrow m_i + \frac{\bar{p}_i^2}{2m_i}; \qquad \text{(in left side)}$$

$$\omega_i \rightarrow m_i, \ \ \gamma_i^0 \rightarrow 1, \ \ h_i \rightarrow m_i, \ \ \gamma_i^5 \rightarrow 0; \quad \text{(in right side)} \quad (33)$$

$$\bar{\varphi}_M^{(+++)} \rightarrow \chi_{MNR}^{(+++)}, \text{ other components are equal to zero.}$$

As a result taking into account only qq -interaction confinement potential we obtain well known equations $(m_1 = m_2 = m)$

$$[(\varepsilon_{B_p} + \varepsilon_{B_q}) - \frac{\bar{p}^2}{2m_p} + \frac{\bar{q}^2}{2m_q}) + \frac{\mu_p \omega_p^2}{2} \Delta_p + \frac{2}{3}\alpha_S(4m^2)V_0 +$$

$$+ \frac{\mu_q \omega_q^2}{2} \Delta_q + \frac{4}{3}\alpha_S((m+m_3)^2)V_0]\chi_{MNR}(\bar{p}, \bar{q}) = 0, \quad (34)$$

where

$$M - (2m + m_3) \equiv \varepsilon_{B_p} + \varepsilon_{B_q}, \ \mu_p = \frac{m}{2}, \ \mu_q = \frac{2mm_3}{2m + m_3}, \quad (35)$$

$$\omega_p = \omega_0 \sqrt{\frac{2}{3}[\alpha_S(4m^2) + \alpha_S((m+m_3)^2)\frac{m_3}{m+m_3}]},$$

$$\omega_q = \omega_0 \sqrt{\frac{2}{3}\frac{2m+m_3}{m+m_3}\alpha_S((m+m_3)^2)}.$$

The wave function $\chi_{MNR}(\vec{p}, \vec{q})$ is represented analogously to (32)

$$\chi_{MNR}(\vec{p}, \vec{q}) = \sum_{n_p n_q l_p l_q m_p m_q} \left\langle \vec{p} \middle| l_p m_p \right\rangle \left\langle \vec{q} \middle| l_q m_q \right\rangle R_{n_p l_p}(p) R_{n_q l_q}(q), \quad (36)$$

$$R_{n_p l_p}(p) = p_0^{-3/2} R_{n_p l_p}(x), \ x = \frac{p}{p_0}, \ p_0 = \sqrt{\mu_p \omega_p}, \quad (37a)$$

$$R_{n_q l_q}(q) = q_0^{-3/2} R_{n_q l_q}(y), \ y = \frac{q}{q_0}, \ q_0 = \sqrt{\mu_q \omega_q};$$

$$R_{nl}(u) = \frac{1}{\Gamma(l+\frac{3}{2})}\sqrt{\frac{2\Gamma(n+l+\frac{3}{2})}{\Gamma(n+1)}}u^l \exp(-\frac{1}{2}u^2){}_1F_1(-n,l+\frac{3}{2};u^2);$$
$$(37b)$$

$$\varepsilon_{n_p l_p} + \frac{2}{3}\alpha_S(4m^2)V_0 = (2n_p + l_p + \frac{3}{2})\omega_p, \ \varepsilon_{n_q l_q} +$$

$$+\frac{2}{3}\alpha_S((m+m_3)^2)V_0 = (2n_q + l_q + \frac{3}{2})\omega_q, \quad (37c)$$

Now using the radial wave functions (37a) as a basis functions the unknown functions $_M R_{l_p l_q S_{12}}^{(\alpha_2\alpha_1)LSJ}(p, q)$ can be written as

$$_M R_{l_p l_q S_{12}}^{(\alpha_2\alpha_1)LSJ}(p, q) = \sum_{n_p n_q} C_{n_p n_q S_{12}}^{(\alpha_2\alpha_1)LSJ}(M) R_{n_p l_p}(p) R_{n_q l_q}(q), \quad (38)$$

19

and putting it in the system of equation mentioned above we obtain the system of algebraic equation (nonlinear over M) for coefficients $C_{n_p n_q S_{12}}^{(\sigma_1 \sigma_2 \sigma_3) LSJ}(M)$, solution of which gives mass we are looking for.

REFERENCES

1. Jean-Mare Richard. Phys. Rev. **212**, 1972, 1.
2. A.N. Mitra. Z. Phys. **C8**, 1981, 25.
3. N.N. Singh, Y.K. Mathur, A.N. Mitra. Few-Body Systems. **1**, 1986, 47.
4. M. Chachkhunashvili and T. Kopaleishvili. Contributions Few-Body, XI, Tokyo/Sandai, August 1986, Supplement to Research Report of Laboratory of Nuclear Science Tohoros University, **12**, 1986, 98.
5. D.S. Kulshreta, A.N. Mitra. Phys. Rev **D37**, 1988,1268.
6. A.N. Mitra, I. Sonthanom. Few-Body Systems. **12**, 1992, 41.
7. F. Schlumpf. Phys. Rev. **D47**, 1993, 4114.
8. Yu-Bing Dong, Jun-Chen Su, Shi-Shu Wo. J. Phys. G: Nucl. Part. Phys. **20**, 1994, 73.
9. Ansu Sharma, S.R. Chondhure, A.N. Mitra. Phys. Rev. **D50**, 1994, 454.
10. M.A. Ivanov, J.G. Körner, V.F. Lyubivitsky, A. Rusetsky. Phys. Rev. **D59**, 1999, 0740161.
11. U. Löring, K. Kretzscmar, B.Ch. Metch, H.R. Petry. Eur. Phys. J. **A10**, 2001, 309.
12. S. Chakrabarty et al. Prog. Part. Nucl. Phys. **22**, 1979, 43.
13. V.B. Mandelzweig, S.I. Wallace. Phys. Lett. **B174**, 1987, 469.
14. U. Löring, B.Ch. Metch, H.R. Petry. Eur. Phys. J. **A10**, 2001, 395.
15. T. Kopaleishvili. Phys. Nucl. **32**, 2001, 560.
16. T. Babutsidze, T. Kopaleishvili, A. Rusetsky. Phys. Lett. **B426**, 1998, 139; Phys. Rev. **C59**, 1999, 976.

Tbilisi State University

თ. ბაბუციძე, თ. კოპალეიშვილი, ვ. სხირტლაძე,
დ. კურაშვილი

ბზედ qqq-სისტემებისათვის ბეტ3-სოლიპტერის
განრიგების სამგაზხმიანობიან განრიგებაზე დაყვანის
სამი სხვადასხვა ვარიანტი

გასცემ

განხილულია ბზედ qqq-სისტემისათვის ბეტ3-სოლიპ-
ტერის განრიგების სამგაზხმიანობიან განრიგებაზე
დაყვანის სამი სხვადასხვა ვარიანტი, ორ-და სამძზი-
ლიკუუდიან ურთიერთქმედებით პოტენციალის გათვალისწი-
ნებით. მიღებული რადიალური ფუნქციისათვის ნორმირების
პირობა. მიღებული განრიგების არარელატივისტური
ზღვრის ირნგლიკაციია კონფაინმენტური ურთიერთქმე-
დების ოსცილატორული პოტენციალისათვის ამოხსნილი
(როგორც საბაზისო ფუნქციით) გამოიყენებით დადგე-
ნილია ალგებრულ განრიგებათა სისტემის გაზლის
კოეფიციენტებისათვის. შემდეგში გამოკვლეული იქნება
ბზედ მდგომარეობის არსებობის გამოკიდებულება ორ-
და სამძზილიკუუდიან კონფაინმენტში (დაჭიმულობის) პოტენ-
ციალების ლორენც (სინერ) სტრუქტურაზე.

STUDY OF TRANSFORMATION OF AIR STREAM ON THE TERRITORY OF WEST GEORGIA CONSIDERING THE INFLUENCE OF THE BOUNDARY LAYER PARAMETERS.

Z. Khvedelidze, N. Cheishvili, T. Shalamberidze, R. Aplakov.

ABSTRACT. It is natural that physiographic location of an investigated region determines the dynamics of atmospheric processes in it. In particular, air mass blows from the Blak Sea and peculiarities of the terrain make study of airblow transformation processes very interesting on the territory of West Georgia. Investigation of these processes is an important issue when air mass blows from one type of an underlayer, such as sea surface, to another one – earth surface. A new parameter, which reflects the influence of the relief on the air stream transformation, we have included into the famous equation system.

Comparing calculated values with the factual, an important conclusion can be made that consideration of the parameter of the relief influence on the air-stream transformation makes the calculated speed closer to the factual by 3-4%.

Especially it concerns the influence of a relief, although this region is not distinguished with distinct orography. Naturally, farther from the coast height of the orography increases and thus makes the relief influence. Mostly, mountain ridges of Likhi and Kharagauli make humid air move back to West Georgia. This result is a confirmation of the fact that there is a tendency for the fall of temperature against the global warming.

It is natural that physiographic location of the investigated region determines the dynamics of atmospheric processes in it. In particular, air mass flow from Black Sea and peculiarities of the terrain make study of airflow transformation processes on the territory of West Georgia very interesting. Investigation of these processes is an

important issue when air mass blows from one type of an underlayer, such as sea surface, to another one - earth surface.

The time needed for formation of quasistationary regime in the boundary layer of the atmosphere is assumed as duration of the air stream transformation process. At these conditions, the system of hydro-thermodynamic equations are simplified [1-3] as heat, radial and phase effects are excluded. Thus, the problem comes down to the following system:

$$u \frac{\partial u}{\partial x} + w \frac{\partial u}{\partial z} = \frac{\partial}{\partial z} \left(k \frac{\partial u}{\partial z} \right), \tag{1}$$

$$\frac{\partial u}{\partial x} + \frac{\partial v}{\partial z} = 0 \tag{2}$$

$$u \frac{\partial b}{\partial x} + w \frac{\partial b}{\partial z} = k \left(\frac{\partial u}{\partial z} \right)^2 - c \frac{b^2}{k}, \tag{3}$$

$$k = \chi c^{\frac{1}{4}} \sqrt{b} \frac{\frac{\partial u}{\partial z}}{\frac{\partial^2 u}{\partial z^2}}, \tag{4}$$

where u and w are the components of wind velocity on ox and oy coordinate axes correspondingly; k is a turbulence factor; b - turbulence energy; χ - the Karman constant; c – the constant value [4-6].

It is assumed that we have horizontally homogeneous layer that meets the following conditions: when $x < 0$, the movement is ordered; when $x > 0$, movement velocity and impulse are continuous. In this arrangement, the next boundary conditions for the solution of system (1-4) are required [1]:

$$u = \frac{v'_a}{\chi} \ln \frac{z}{z_0}, \qquad b = c^{-\frac{1}{2}} v_*^2, \tag{5}$$

at $x = 0$ and $z > z_0'$;

$$u = w = 0, \qquad k = \chi z_0^* v_*^*(x), \qquad k \frac{\partial u}{\partial z} = v_*^{*2}, \tag{6}$$

at $z = z_0^*$ and $x > 0$;

23

$$u = \frac{v_*'}{\varkappa} \ln \frac{h}{z_0'} , \qquad k \frac{\partial u}{\partial z} = v_0^{*2} , \qquad (7)$$

at $z = h$ and $x > 0$.

where h is the height of the layer; z_0' - height of the land surface "roughness" at $x < 0$; z_0' is the same as $x > 0$; v_*' and v_*'' are the magnitudes of dynamic speed at $x < 0$ and $x > 0$ respectively.

With dimensionless quantities, the system (1) – (4) will appear in the form:

$$\alpha \left(u_n \frac{\partial u_n}{\partial x_n} + w_n \frac{\partial u_n}{\partial z_n} \right) = \frac{\partial}{\partial z_n} k_n \frac{\partial u_n}{\partial z_n} , \qquad (8)$$

$$\frac{\partial u_n}{\partial x_n} + \frac{\partial w_n}{\partial z_n} = 0, \qquad (9)$$

$$\frac{\varkappa^2}{c^{\frac{1}{2}}} \alpha \left(u_n \frac{\partial b_n}{\partial x_n} + w_n \frac{\partial b_n}{\partial z_n} \right) = k_n \left(\frac{\partial u_n}{\partial z_n} \right)^2 - \frac{b_n^2}{k_n} , \qquad (10)$$

$$k_n = -\sqrt{b_n} \frac{\frac{\partial u_n}{\partial z_n}}{\frac{\partial^2 u_n}{\partial z_n^2}} . \qquad (11)$$

The corresponding boundary conditions may be written as:

$$u_n = \ln z_n, \quad b_n = 1, \qquad (12)$$

at $x_n = 0$ and $z_n \geq 1$;

$$u_n = w_n = 0, \quad k_n = mp, \quad k_n \frac{\partial u_n}{\partial z_n} = p^2 , \qquad (13)$$

at $z_n = m$ and $x_n > 0$;

$$u_n = \ln h_n, \quad k_n \frac{\partial u_n}{\partial z_n} = 1 , \qquad (14)$$

at $z_n = h$ and $x_n > 0$.

where $\alpha = \frac{v_*' - v_*''}{v_*'}$ is the "roughness" parameter, $m = \frac{z_0''}{z_0'}$

24

$$p = \frac{v_*''(x)}{v_*'}. \tag{15}$$

If α is a small value, convective system may be solved in the form of sequences:

$$u_n = u_{n_0} + \alpha u_{n_1} \qquad w_n = w_{n_0} + \alpha w_{n_1} \tag{16}$$

$$k_n = k_{n_0} + \alpha k_{n_1} \qquad b_n = b_{n_0} + \alpha b_{n_1}$$

Solution of the given problem in zero-order approximation is described in detail in [1-3]. For a wind profile and vertical component the following relations are obtained:

$$u = p \ln \frac{z}{m}, \tag{17}$$

$$w = -\frac{dp}{dx}\left(z \ln \frac{z}{m} - z + m\right) \tag{18}$$

Within the same problem, we have considered the terrain features using streamlining conditions of a mountain. Thus, instead of the vertical coordinate z we have introduced z_1, which is expressed as [3,4]:

$$z_1 = \frac{z - \zeta(x,y)}{H - \zeta(x,y)} H, \tag{19}$$

where $\zeta(x,y)$ is the function describing a surface; H – the height, where the air stream is horizontal. Considering (19), in the zero-order approximation (8) - (15) we will obtain:

$$\frac{\partial}{\partial z_1}\left(k_0 \frac{\partial u_0}{\partial z_1}\right) = 0, \tag{20}$$

25

$$\frac{\partial u_0}{\partial z_1} + d \frac{\partial u_0}{\partial z_1} = 0, \tag{21}$$

$$k_0 \left(\frac{\partial u_0}{\partial z_1} \right)^2 = \frac{b_0^2}{d^2}, \tag{22}$$

$$k_0 = \frac{-\sqrt{b_0}}{d} \frac{\frac{\partial u_0}{\partial z_1}}{\frac{\partial^2 u_0}{\partial z_1^2}}. \tag{23}$$

The boundary conditions are:

$$u_0 \frac{\partial u_0}{\partial z_1} = \frac{p^2}{d}. \tag{24}$$

at $z_1 = m_1 = \frac{z_0^{\sigma}}{z_0'}, \quad x > 0; \quad u_0 = 0, \quad k_0 = m_1 p;$

$$u_0 = \ln h, \tag{25}$$

at $z = h$ and $x > 0$.

where $d = \dfrac{H}{H - \zeta(x, y)}$ is a parameter characterizing the terrain.

After integrating equation (20) by z_1 taking into account conditions (24) and (25) we will get:

$$b_0^2 = p^2 d \tag{26}$$

Let us rewrite equation (20) in the expanded form:

$$\frac{\partial k_0}{\partial z_1} \frac{\partial u_0}{\partial z_1} + k_0 \frac{\partial^2 u_0}{\partial z_1} = 0. \tag{27}$$

Using equation (23), we can exclude $\frac{\partial^2 u_0}{\partial z_1}$ factor from (27). So, it gets the following form:

$$\frac{\partial k_0}{\partial z_1} = \frac{p}{\sqrt{d}}. \tag{28}$$

Integrating (28), we obtain:

$$k_0 = \frac{p}{\sqrt{d}} z_1. \tag{29}$$

After using condition (24) and integrating from m_1 to z_1:

$$u_0 = \frac{p}{\sqrt{d}} \ln \frac{z_1}{m_1}. \tag{30}$$

Using the continuity equation for w_0, we get:

$$w_0 = -\frac{1}{d} \frac{dp}{dx} \left(z_1 \ln \frac{z_1}{m_1} - z_2 + m_1 \right). \tag{31}$$

Equations (31) and (30) differ from corresponding (17) and (18) ones by presence of parameter d, that reflects the influence of the relief on the air stream transformation.

Magnitudes of the characteristic parameters and sizes of their changing are given in Table 1.

Table 1

Parameter Height(m)	m	p	v_*'	v_*''	z_0' (cm)	z_0'' (cm)
2	0.1 0.5 1.0	1		30		
4	0.1 0.5 1.0	0.83		25		
8	0.1 0.5 1.0	0.69	30	20	2.5	0.2 - 20.0
16	0.1 0.5 1.0	0.33		10		

Value Height	p	u_a			$u_a(p,m)$ average	p	u_s			$u_s(p,m)$ average
		m=0.1	m=0.5	m=1.0			m=0.1	m=0.5	m=1.0	
2	1	2.99	1.38	0.69	1.69	1	2.99	1.38	0.69	1.69
4	0.83	3.07	1.73	1.15	1.98	1	3.68	2.09	1.38	2.38
8	0.69	2.91	1.84	1.34		1	4.33	2.76	2.07	3.06
16	0.33	1.69	1.15	0.92	1.25	1	5.07	3.85	3.68	4.06
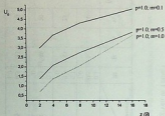
Fig. 1.
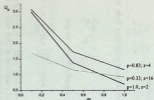
Fig. 2.

Table 3

location	Height (m)	d	√d	W average (cm/wm)				u_d				u_z conc.	w_{max}
				z=2	z=4	z=8	z=16	z=2	z=4	z=8	z=16		
Zugdidi	110	1.123	1.059		2.84	4.80	4.47	1.92	2.68	3.83	4.22	3.17	3.6
Kutaisi	125	1.143	1.069					1.99	2.74	4.04	4.47	3.14	3.1
Sokhumi	140	1.162	1.074					1.99	2.78	4.00	4.38	3.29	2.9
Gali	48	1.050	1.025					1.98	2.77	3.98	4.36	3.27	2.1
Pati	3	1.003	1.001					2.03	2.84	4.08	4.47	3.35	4.3
Kobuleti	5	1.005	1.005					2.03	2.84	4.08	4.47	3.35	2.4
Senaki	28	1.029	1.024					1.98	2.77	4.36	3.27	2.2

The computations can be made at the same altitude for various m and p. Also it is possible with constant p and variables z and m, or with constant m and variable z and p [5,6]. The corresponding values of U_0 and U_0' are given in Table 2.

Dependences of velocities u_0 and u_0' on z for different p and m are given in Figs.1 and 2.
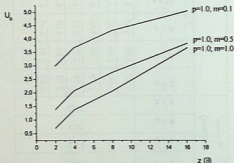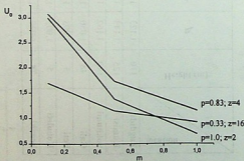

Fig.1.

Fig 2

From Fig.1 follows that in the investigated region wind speed increases almost linearly and it gets logarithmic at increase of m; at constant p, this relation is logarithmic; Fig.2 shows that u_0 depends on m almost exponential. In fact, these results agree with the evaluations given in literature [1,3].

Similar calculations are made taking into account parameter d for the real velocity $u = u_0 v_*$ this time. Here $v_* = 1,2$m/sec, when $z = 2, 4$ or $8(m)$ and $v_* = 1,1$ when $z = 16$m.

The corresponding values of all the parameters by 7 locations of west Georgia are given in Table 3.

For computation of the vertical components w and w_d of velocity, we used arithmetic average of the pointed values. For instance, at $m = 0.5$; $p = 0.75$, then applying equations (8) and (31), we get correspondingly at $\Delta x = 3 \times 10^4$ m:

$w = -3.68 \times 10^{-4}$ m/vom, $w_d = -3.48 \times 10^{-4}$ m/wm, at $\Delta x = 3 \times 10^4$ m

$w = -3.68 \times 10^{-2}$ m/vom, $w_d = -3.48 \times 10^{-2}$ m/wm, at $\Delta x = 3 \times 10^4$ m

For the whole region $u_{av} = 3.35$ m/sec, $u_d = 3.26$ m/sec and average velocity of the actual wind is 3.27 m/sec. Thus, if we take into account parameter d, difference between real and calculated values is just 0.3%, as that between u_{real} and u makes 2.4%. Consequently, an important conclusion can be made that consideration of variations of boundary layer parameters at air stream transformation gets closer the calculated values with their actual magnitudes. Especially it concerns influence of a relief, although this region is not distinguished with distinct orography. Naturally, farther from coast height of the orography increases and so does the relief influence. Mostly, mountain ridges of Likhi and Kharagauli make humid air to trawl backward to west Georgia. This result is a confirmation of the fact that there is a tendency to fall of temperature against the global warming.

REFERENCES

1. Dinamicheskaya Meteorologia. Ed.: D.L. Laikhtman, M., 1976, 500 p (Russian).

2. Z. Khvedelidze. Dinamikuri Meteorologia. Tbilisi, 2002, 525 (Georgian).

3. J. Haltinger, F. Martin. Dynamicheskaya i Fizicheskaya Meteorologya. Transl. from Engl. Ed.: A.S. Monina.M., 1960, 435 (Rissuan);

4. P. N. Velov, E. P. Borisenkov, B. D. Panin. Chislennie Metody Prognoza Pogody. L., 1989, 375 (Russian).

5. Z. Khvedelidze, R. Aplakov, R. Chelidze, N. Cheishvili, D. Gogatishvili, G. Erqomaishvili. Metsniereba da Teqnologiebi, 4-6, 2005, 37 (Georgian).

6. Z. Khvedelidze, N. Pavlenishvili. Meteorologia I Gidrologya. 1996, **2**, 48.

ზ. ხვედელიძე, ნ. ჭიჭშველი, თ. მალამბრიძე, რ. აპლაკოვ

ჰაერის ნაკადის ტრანსფორმაციის გამოკვლევა დასავლეთ საქართველოს ტერიტორიაზე მიწისპირა ფენის პარამეტრების გაველების გათვალისწინებით

დასკვნა

დასავლეთ საქართველოს ტერიტორიაზე შავი ზღვის ზედაპირიდან ჰაერის მასათა შემოდინებისას მკვდა ექსტ-ალურება ამ ნაკადის ტრანსფორმაციის შესწავლა დევდმიანი ზედაპირის მოსდცივისას და ოროგრაფიის გავლენის გათვალისწინებით. სტატიაში თეორიულად მიღებული ჰიდროთერმოდინამიკის განტოლებათა სისტემაში შემ-ცდანილი დევდმიანი ოროგრაფიის ამსახველი პარამეტრის ან მოხდებიდ შესაბამია გათვილბი. გამოვენება მიწდ ხვედდ ქდ მექდართლოდუტუ ელემდირქდამ მრცადსლოთდდ სიც შდ დ ზდუალქდამი ჰდრის მას ბადგდცდდ მია სიცქ ჰორისზორტდ დ ვდრტდდ მდდდ.

გამოვლილია მნიშვნელოვნების ფაქტიურთან შედარებით ამცირებდა, რომ დღევანდელ რელიეფში გავდების პარამეტრისთან გადათანებისას, პაულოს ნაკადის ტრანსპორტამაგვალოსის ქარის სისქისაი მნიშვნელოვანი რეცეფტორ 34% უფრო ახლოსაა, ვიდრე ამ პარამეტრის გათვალისწინებით გარეშე.

ამ რეგიონში ზღვისგან დაშორებით იზრდება ორთოგრაფიის სიმაღლე და შესაბამისად რელიეფის გავდება. ხარიაგულისა და ლისის ქედისა კი უმეტეს შემთხვევაში აიღლისდება პაულოს ნიისს იმასაი დამრეცდდ უკან დასაცდ ცალი საქართველესკი. ეს შედეგი ერთგვარი დადასტურებაა იმ პირისსა, რომ დასავლეთ საქართველოში გავდებ ავლისა ქერცედგისა გლოსალური დათბობის ფონსე.

CHAOS IN POLYATOMIC MOLECULES

A. Ugulava, L. Chotorlishvili, T. Gvarjaladze and S.Chkhaidze

ABSTRACT. Polyatomic molecules can perform internal rotational motion of two types: torsional oscillation and free rotation of one part of the molecule with respect to the other part. On the phase plane these two types of motions are separated by the separatrix. Phase trajectories, originated as a result of periodical external force action on the system have stochastic nature. At the quantum consideration of the motion near to the classical separatrix, transition from the pure quantum-mechanical state to the mixed one takes place. Originated at mixed state, it must be considered as the quantum analogue of the classical dynamic stochasticity and named as the quantum chaos. This work is devoted to the investigation of the quantum chaos manifestation, in the polyatomic molecules, which have property to perform internal rotation. For the molecule of ethane C_2H_6, the emergence of quantum chaos and possible ways of its experimental observation have been studied. It is shown, that radio-frequency field can produce the non-direct transitions between rotational and oscillatory states. These transitions, being the sign of the existence of quantum chaos, are able to change levels population sizeably and due to this phenomenon experimental observation of the infrared absorption is possible.

1. INTRODUCTION

The traditional notion of an area, where the laws of statistical physics are effective, consists in the assumption that the number of interacting particles is sufficiently large. However, a lot of examples of systems with a small number of degrees of freedom, where chaotic motions occur, had become known [1,2] by the end of the last century. A new stage in the development of notions about a chaos and its origin appeared in the last two decades of the past century. It turned

out that classical Hamiltonian system may experience special kind of instability. Because of this instability various dynamic characteristics of the system randomly change with time. Such a property of the system to perform random motion is called dynamic stochasticity. Dynamic stochasticity is an internal property of the system and is not associated with the action of some a priori random forces. Stochasticity as an internal property of the system is rather frequently encountered in physical problems. The difficulty of revealing it is due to the fact that it occurs either in a very narrow range of parameters or manifests itself on very large time intervals or is veiled by other stronger processes. Quantum analogue of dynamic stochasticity is usually called quantum chaos. By a quantum chaos we understand a quantum state appearing when the ratios of the parameters of a system are the same as those at which, in the case of classical consideration, dynamic stochasticity takes place.

2. A PHASE PORTRAIT OF THE PENDULUM AND FORMATION OF A STOCHASTIC LAYER

In the general theory of stochasticity of Hamiltonian systems the dominating role is played by the problem of a pendulum, the function of whose Hamiltonian has the form

$$H = \frac{P_\varphi^2}{2m} + U(\varphi), \qquad (1)$$

where $P_\varphi = m\dot{\varphi}$ is a pulse and

$$U(\varphi) = mgl(1 - \cos\varphi) \qquad (2)$$

is the periodic potential of the point body of mass m, which is suspended by a thread of length l (see Fig.1).
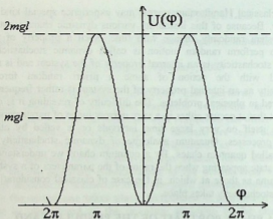
Using the law of energy conservation

Fig.1. The periodic potential of the pendulum. The angle φ is an angle of deviation of the pendulum from the equilibrium state. The equilibrium state of the pendulum is assumed to be a zero value of potential energy.

$$\frac{m\dot{\varphi}^2}{2} + U(\varphi) = E(t=0) = const \qquad (3)$$

we can construct a phase picture of the pendulum (see Fig.2).

Using the energy integral (3) and potential (2), we can obtain an expression for a period of rotational motion of the pendulum

$$T_+ = \frac{m}{2} \int_0^{2\pi} \frac{d\varphi}{\sqrt{E - U(\varphi)}} = \frac{2m}{\sqrt{E}} K(k), \qquad (4)$$

where

$$K(k) = \int_0^{\pi/2} \frac{d\varphi}{\sqrt{1 - k^2 \sin^2 \varphi}} \qquad (5)$$
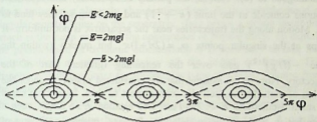
Fig.2. A phase picture of the pendulum. The closed curves $E <$ $2mgl$ correspond to oscillatory motions. The wave curves E $> 2mgl$ correspond to rotational motions. To the energy $E =$ $= mgl$ there corresponds a special trajectory called a separatrix. On the phase plane it separates trajectories with different topology.

is the complete elliptic integral, $k = (2mgl/E)^{1/2}$ is called the module of the integral. For the period T_c of trajectories in the neighborhood of the separatrix ($k \to 1$) we obtain,

$$\lim_{k \to {}^{+}1} T_+ = T_c$$

$$T_c = \frac{2m}{\sqrt{E}} K(k \to {}^{+}1) \approx \frac{2m}{\sqrt{E}} \ln \frac{4}{\sqrt{1-k^2}} = \frac{2m}{\sqrt{E}} \ln 4 \sqrt{\frac{E}{E-2mgl}} . \quad (6)$$

From expression (6) it follows that with the approach to the separatrix from above ($k \to {}^{+}1$) the motion period logarithmically tends to infinity. The oscillatory motion period T_- can be calculated analogously, but we do not do this here. We would like only to note that the approach to the separatrix from below

$$\lim_{k \to {}^{-}1} T_- = T_c$$

is analogous to (6). That is, the periods of oscillatory and rotational motions coincide in the limit $(k \to \pm 1)$ and, in doing so, they tend to T_c. Motion along the trajectories near the separatrix is not uniform. It stops at the singular points $\varphi_n = (2n+1)\pi$, but quickly (within the time $\sim (l/g)^{1/2}$) gets over the remaining (greater) part of the trajectory. Now let us assume that the considered system is under the action of perturbation, periodic with respect to time. In limiting cases of small oscillations $E \ll 2mgl$ and free rotation $E \gg 2mgl$, such a perturbation leads to the modulation of phase trajectories. Points of intersection of a perturbed trajectory with an unperturbed one arise on the phase plane regularly. The position of each point completely depends on the position of the preceding one. The situation changes radically if an unperturbed trajectory lies near the separatrix ($E \approx 2mgl$). Since in that case the motion makes a prolonged, though unstable, stop in the neighborhood of nodal singular points, even small perturbations may strongly affect the trajectory. Then points of intersection of perturbed trajectories with unperturbed ones appear on the phase plane irregularly (randomly). An area of the phase space occupied by random trajectories is called a stochastic layer (see Fig.3). Thus the main condition for the formation of a stochastic layer is motion near separatrix ($E \approx 2mgl$). The stochastic layer width is defined by a difference $E - 2mgl$ and a variable field amplitude.
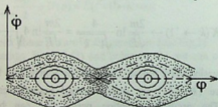

Fig.3. The formation of a stochastic layer near the separatrix.

Note that even at first glance we see that in the considered case, dynamic stochasticity appears in the completely deterministic dynamic system. Motion stochasticity is directly connected with the availability

of the separatrix on the phase plane. On stepping over the separatrix, phase trajectories abruptly change their form. In the neighborhood of singular points, lying on the separatrix, there arises a strong instability which is the main cause for the appearance of stochasticity. To explain the phenomenon of dynamic stochasticity it is necessary to take into consideration a small dispersion of the initial conditions. This dispersion is insignificant for trajectories lying at a large distance from the separatrix ($E >> 2mgl$, $E << 2mgl$), while for trajectories near the separatrix ($E \approx 2mgl$), the initial dispersion grows so that, with a lapse of time, motion becomes completely unpredictable. A detailed study of the criterion of stochasticity formation in classical nonlinear systems can be found in [1,2]. We do not discuss this issue here.

3. QUANTUM CONSIDERATION. INTERNAL ROTATION IN POLYATOMIC MOLECULES

Let us now consider a quantum analogue of the pendulum (quantum pendulum). The corresponding Hamiltonian can be obtained from (1) if we replace there the pulse P_φ by its operator $\hat{P}_\varphi = i\hbar \partial / \partial \varphi$. Then we have

$$\hat{H} = -\frac{\hbar^2}{2m}\frac{d^2}{d\varphi^2} + U(\varphi) \qquad (7)$$

Note that this form of the Hamiltonian is usually used to describe internal rotation in polyatomic molecules. As is known [3,4], one of the forms of internal motion in polyatomic molecules is torsional oscillation which for sufficiently large amplitudes transforms to rotational motion. In order to describe the corresponding motion in Hamiltonian (7) we assume that φ is the angle of torsion of one part of the molecule with respect to the other part and replace the mass m by the reduced moment of inertia $I = I_1 I_2 / (I_1 + I_2)$, where I_1 and I_2 are the inertia moments of rotation of the parts of the molecule with respect to its symmetry axis. Thus we obtain

$$U(\varphi) = \frac{V_0}{2}(1 - \cos n\varphi),$$

where V_0 defines the height of potential barrier that separates torsional oscillations from the rotation of one part of the molecule with respect to the other part, and n defines the quantity of equilibrium orientations of one part of the molecule with respect to the other part. For the molecule of ethane H_3C-CH_3, dimethylacetylene $H_3C-C\equiv C-CH_3$ and for other organic molecules we have $n = 3$ equilibrium configurations (see Fig.4).
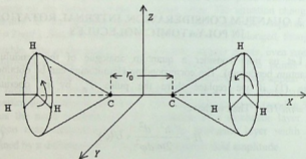

Fig.4. A schematic drawing of the molecular structure of ethane H_3C-CH_3. The circular arrow shows the torsion phase φ, r_0 is the equilibrium distance between two parts of molecule

The configuration shown in Fig.4 corresponds to an energy maximum and is a nonequilibrium configuration (cis-configuration). Other nonequilibrium configurations are obtained by rotating by the angles $\frac{2\pi}{3}$ and $2 \cdot \frac{2\pi}{3}$. Equilibrium configurations (trans-configurations) are obtained by rotating the angles $\frac{\pi}{3}, \frac{\pi}{3} + \frac{2\pi}{3}, \frac{\pi}{3} + 2 \cdot \frac{2\pi}{3}$.

9

Below we give the numerical values [3,4] of other parameters of some organic molecules having the property of internal rotation. Thus for the molecule of ethane C_2H_6 we have $I_1 = I_2 \approx$ $\approx 5.3 \cdot 10^{-47} kg \cdot m^2$, $V_0(C_2H_6) \approx 2.1 \cdot 10^{-20} J$, and for the molecule of dimethylacetylene C_4H_6 we have $I_1 = I_2 \approx 10.6 \cdot 10^{-47} kg \cdot m^2$, $V_0(C_4H_6) \approx 0.34 \cdot 10^{-20} J$.

The Schrodinger equation corresponding to Hamiltonian (7) has the form

$$\frac{d^2\psi}{d\varphi^2} + \frac{2I}{\hbar^2}\left[\varepsilon_k - \frac{1}{2}V_0(1-\cos n\varphi)\right]\psi = 0, \qquad (8)$$

where ε_k is the eigenenergy of the k-th state. Note that $\varepsilon_k = \varepsilon_k(V_0)$ is the function of barrier height V_0. The condition of motion near the separatrix (near a potential maximum) is written in the form $\varepsilon_k \approx V_0$. If we introduce the new variable $\alpha = \frac{n\varphi}{2}$, then equation (8) can be rewritten as

$$\frac{d^2\psi(\alpha)}{d\alpha^2} + \left[E - 2l_0 \cos 2\alpha\right]\psi(\alpha) = 0 \qquad (9)$$

where

$$E = \frac{8I}{n^2\hbar^2}(\varepsilon - V_0/2) \qquad (10)$$

plays the role of energy in dimensionless units, and the parameter

$$l_0 = \frac{2I}{n^2\hbar^2}V_0 \qquad (11)$$

is the half-height of the barrier in dimensionless units and plays the same role as the length of the thread does in the classical pendulum problem. Equations (8) and (9) are called the Mathieu-Schrodinger equations. It describes the dynamics of the "quantum pendulum".

41

The Mathieu-Schrödinger equation (9) is a linear equation, which gives us the grounds to believe that for the quantum evolution no instability, which leads to chaos and the instability of trajectories, might develop as this happens in the classical case. Another property of dynamic stochasticity is a jump-like change of the form of phase trajectories when they pass across the separatrix. In the case of quantum consideration, a smooth transition from the discrete energy spectrum to the continuous one takes place near the maxima of the periodic potential (Fig.1), which is connected with a possible tunneling through the barrier. This fact does not work in favor of chaos either. However, as is shown in [5-7], the basic properties of dynamic stochasticity (in particular the irreversibility of the process) manifest themselves in the case of quantum consideration too. It can be assumed that a mixed state is a quantum analogue of classical stochastic motion. In our problem the transition from the pure state to the mixed one occurs due to special properties of the Mathieu-Schrödinger odinger equation to be described below. A peculiar feature of the Mathieu-Schrödinger odinger equation consists in the specific dependence of eigenvalues $E_n(l)$ and eigenfunctions $\psi_n(\varphi, l)$ on the parameter l (see Fig.5). On the plane (E, l), on which the spectral characteristics (so-called Mathieu characteristics [6]) are drawn, this peculiarity manifests itself in the alternation of areas of twice degenerate G_2 and nondegenerate states G. The boundaries between these areas pass across the branch points of energy terms $E_n(l)$.

The presence of degenerate and nondegenerate states of the quantum mathematical pendulum was established by studying the symmetry properties of the Mathieu-Schrödinger equation. In [5] the eigenfunctions were defined for each one of the areas of degenerate states G_2 and nondegenerate states G:

$$\psi_{2n+1}^{\pm}(\varphi) = \frac{1}{\sqrt{2}}(ce_{2n+1}(\varphi) \pm i se_{2n+1}(\varphi)),$$
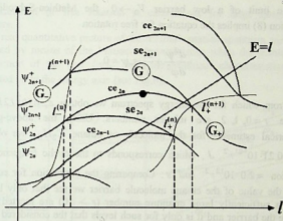
Fig.5. A fragment of a parametrically dependent energy spectrum of the quantum mathematical pendulum. The straight line $E = l$ corresponds to the separatrix of classical motion. By $l_{\pm}^{(m)}$ are denoted the points of branching of energy terms to the left and to the right of the separatrix.

$$\psi_{2n}^{\pm}(\varphi) = \frac{1}{\sqrt{2}}(ce_{2n}(\varphi) \pm ise_{2n}(\varphi)), \qquad (G_-)$$

$$ce_{2n}(\varphi); \quad ce_{2n+1}(\varphi); \quad se_{2n}(\varphi); \quad se_{2n+1}(\varphi), \qquad (G)$$

$$\xi_{2n}(\varphi) = \frac{1}{\sqrt{2}}(ce_{2n}(\varphi) + ise_{2n+1}(\varphi)), \qquad (G_+)$$

$$\zeta_{2n+1}(\varphi) = \frac{1}{\sqrt{2}}(ce_{2n+1}(\varphi) \pm ise_{2n+2}(\varphi)).$$

Here $ce_n(\varphi)$ and $se_n(\varphi)$ denote the periodic Mathieu functions [8]. Let us consider two limiting cases of a low and a high energy barrier.

43

In the limit of a low barrier $V_0 \to 0$, the Mathieu-Schrödinger equation (8) implies the equation for free rotation

$$\frac{d^2\psi}{d\varphi^2} + \frac{2I}{\hbar^2}\varepsilon_r\psi = 0.$$

From which for the energy spectrum we obtain $\varepsilon_r = (\hbar^2/2I)r^2$, where $r = 0, 1, 2...$ are integer numbers. Using the above-given numerical estimates for the molecule of ethane C_2H_6, we obtain $\varepsilon_r \approx 0.21 \cdot 10^{-21} r^2$ J, which corresponds to the cyclic frequency of rotation $\approx 0.2 \cdot 10^{12} r^2$ rad/s. Comparing the expression for energy with the value of the ethane molecule barrier we see that only levels with a sufficiently large quantum number ($r > 10$) are located high above the barrier and it is only for such levels that the considered limit is valid.

In another limiting case of a high barrier V_0 the rotator is most of the time inside one of the potential wells where it performs torsional motions. In that case α can be treated as a small angle. After expanding the potential energy in the Schrödinger equation (9) into small angles $\cos 2\alpha \approx 1 - 2\alpha^2$, we obtain a quantum equation for the oscillator, whose energy spectrum has the form $\varepsilon_r = (r + 1/2)\hbar\omega$, where $\omega = n\sqrt{V_0/2I} \approx 6.0 \cdot 10^{13}$ rad/s. For the energy spectrum of small torsional oscillations we obtain $\varepsilon_r \approx (r + 1/2) \cdot 0.63 \cdot 10^{-20} J$. If we compare the obtained expression for the spectrum with the corresponding numerical value of the barrier, then we can see that only the first three levels $\varepsilon_0 \approx 0.32 \cdot 10^{-20} J$, $\varepsilon_1 \approx 0.95 \cdot 10^{-20} J$ and $\varepsilon_2 \approx 1.58 \cdot 10^{-20} J$ are located in the well but not at a sufficiently large depth that would allow us to assume that passages between them correspond to small oscillations. Thus we can conclude that for internal rotation of the molecule of ethane C_2H_6 the approximation of small oscillations is not carried out sufficiently well, while the

approximation of free rotation is carried out for large quantum numbers.

A real quantitative picture of the internal rotation spectrum can be obtained by means of the Mathieu-characteristics when the points of intersection of the line $l = l_0$ with the Mathieu- characteristics is projected on to the energy axis (see Fig.6).
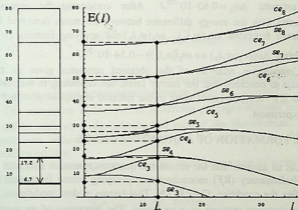

Fig.6. The graphic method of finding energy terms of internal

rotation. For the ethane molecule $l_0 = \dfrac{2I}{9\hbar^2} V_0 \approx 12.4$

These conclusions are in good agreement with experimental data. In particular, in the experiment we observed the infrared absorption by molecules of C_2H_6 at a frequency $\sim 8.7 \cdot 10^{12} Hz$ [9]. For an energy difference between the levels participating in the absorption process we have the estimate $\Delta \varepsilon_{exper} \sim 0.54 \cdot 10^{-20} J$. Comparing the experimental result with the energy difference between two

neighboring levels in the case of approximation of small oscillations, we obtain

$$\Delta\varepsilon_0 = 2\pi\nu_0\hbar,$$

where $\nu_0 = \dfrac{3}{2\pi}\sqrt{V_0/2I}$ is the frequency of small oscillations.

Inserting the parameters values for molecules of C_2H_6, we obtain the estimate $\Delta\varepsilon_0 = 0.63 \cdot 10^{-20} J$. After comparing the obtained estimates with the energy difference between the states described by the wave functions $ce_3(\varphi, l_0)$ and $se_3(\varphi, l_0)$ and applying formula (10), we obtain $\Delta\varepsilon(ce_3(\varphi, l_0) \leftrightarrow se_3(\varphi, l_0)) \sim 0.54 \cdot 10^{-20} J$.

Comparative analysis of the obtained estimates gives us the grounds to conclude that the energy levels corresponding to the states $ce_3(\varphi, l_0)$, $se_3(\varphi, l_0)$ participate in the infrared absorption revealed in the experiment.

4. FORMATION OF A QUANTUM CHAOS

Let us assume that the considered quantum system is subjected to a radiofrequency (RF) monochromatic pumping whose frequency Ω satisfies the condition $\Omega \ll V_0/\hbar$. This causes a slow modulation of quick electron motions in a molecule. The formation of an energy barrier V_0 is a result of the averaging over quick electron motions and thus it is obvious that due to the pumping effect the barrier value is time-dependent,

$$V_0 \rightarrow V_0 + \Delta V \cos\Omega t \qquad (12)$$

The depth of modulation ΔV depends on a pumping power. By replacing (12) we obtain the time-dependent Hamiltonian

$$\hat{H} = \hat{H}_0(\varphi) + \hat{H}'(\varphi, t),$$

$$\hat{H}_0(\varphi) = -\frac{\partial^2}{\partial\varphi^2} + l_0\cos 2\varphi, \qquad (13)$$

$$\hat{H}'(\varphi, t) = \Delta l \cos 2\varphi \cos \Omega l \ ,$$

$$\Delta l = \frac{2I}{n^2 \hbar^2} \Delta V \qquad . \qquad (14)$$

Simple calculations show that the matrix elements of perturbation $\hat{H}'(\varphi, t)$ with respect to the wave functions of the nondegenerate area G are equal to zero

$$< ce_n \left| \hat{H}'(\varphi, t) \right| se_n > \sim \Delta l \int_0^{2\pi} ce_n(\varphi) \ \cos 2\varphi \ se_n(\varphi) \ d\varphi = 0 \qquad (15)$$

where n is any integer number. Therefore perturbation (14) cannot bring about passages between nondegenerate levels.

The interaction $\hat{H}'(\varphi, t)$, not producing passages between levels, should be inserted in the unperturbed part of the Hamiltonian. The Hamiltonian obtained in this manner can be considered as slowly depending on time.

Thus, in the nondegenerate area the Hamiltonian can be written in the form

$$\hat{H} = -\frac{\partial^2}{\partial \varphi^2} + l(t) \ \cos 2\varphi \ . \qquad (16)$$

Because of the modulation of the parameter $l(t)$ the system passes from one area to another, getting over the branch points.

As different from the nondegenerate state area G, in the areas of degenerate states G_- and G_+, the nondiagonal matrix elements of perturbation $\hat{H}'(\varphi, t)$ (14) are not equal to zero. For example, if we take the matrix elements with respect to the wave functions $\psi_{2n+1}^{\pm}(\varphi)$, then for the left degenerate area G_- it can be shown that

$$H'_{+-} = H'_{-+} = < \psi_{2n+1}^{+} \left| \hat{H}(\varphi, t) \right| \psi_{2n+1}^{-} > \sim$$

47

$$\sim \Delta l \int_0^{2\pi} \psi_{2n+1}^{+} \overline{\psi_{2n+1}^{-}} \cos 2\varphi \ d\varphi \neq 0 \qquad (17)$$

Note that the value $H'_{+\ -}$ has order equal to the pumping modulation (14) depth Δl.

Analogously to (17), we can write an expression for even $2n$ states as well.

An explicit dependence of $\hat{H}'(\varphi, t)$ on time given by the factor $\cos \Omega t$, is assumed to be slow as compared with the period of passages between degenerate states than are produced by the nondiagonal matrix elements $H'_{+\ -}$. Therefore below the perturbation $\hat{H}'_{+\ -}(\varphi, t)$ is assumed to be the time-independent perturbation that can bring about passages between degenerate states.

In a degenerate area the system may be in the time-dependent superpositional state

$$\psi_{2n}(t) = \mathbb{C}_n^{+}(t) \ \psi_{2n}^{+} + C_n^{-}(t) \ \psi_{2n}^{-} \qquad (18)$$

The probability amplitudes $C_n^{\pm}(t)$ are defined by means of the fundamental quantummechanical equation, expressing the casuality principle. We write such equations for a pair of doubly degenerate states:

$$\begin{cases} -i\hbar \dfrac{dC_n^{+}}{dt} = (E_{0\,n} + H'_{+\ +}) \ C_n^{+} + H'_{+\ -} C_n^{-}, \\[2mm] -i\hbar \dfrac{dC_n^{-}}{dt} = H'_{-\ +} C_n^{+} + (E_{0\,n} + H'_{-\ -}) \ C_n^{-}, \end{cases} \qquad (19)$$

where the matrix elements are taken with respect to degenerate wave functions (see (17)) and E_{0n} is the energy of the n-th degenerate level near a branch point.

Let us assume that at the initial moment of time the system was in the degenerate state ψ_{2n}^-. Then as initial conditions we should take

$$C_n^+(0) = 1, \quad C_n^+(0) = 0 \qquad (20)$$

Having substituted (18) into (17), for the amplitudes we obtain

$$C_n^+(t) = i \exp\left(\frac{i}{\hbar} Et\right) \sin \omega t,$$

$$C_n^-(t) = \exp\left(\frac{i}{\hbar} Et\right) \cos \omega t, \qquad (21)$$

$$E = E_{0n} + H_{\pm}',$$

where $\omega = \dfrac{2\pi}{\tau} = \dfrac{H_{\pm}'}{\hbar}$ is the frequency of passages between degenerate states, τ is the passage time.

Note that the parameter ω has (like any other parameter) a certain small error $\delta\omega$, which during the time of one passage $t \sim 2\pi/\omega$, leads to an insignificant correction in the phase $2\pi(\delta\omega/\omega)$. However, if during the time $t \sim \Delta T$, when the system is in the degenerate area ($\Delta T < T$, $T = 2\pi/\Omega$) there occurs a great number of passages ($\Delta T \gg \tau$), then for $\Delta T \delta\omega \approx 2\pi$, a small error $\delta\omega$ leads to the phase uncertainty. Then we say that the phase is self-chaotized. The self-chaotization forming in this manner can be regarded as the embryo of a quantum chaos which, as we will see in the sequel, further spreads to other states.

5. SPREAD OF THE QUANTUM CHAOS TO ENERGY TERMS

The spread of the quantum chaos, formed as a result of self-chaotization, can be described in the energy space by means of the density matrix.

Let us introduce the density matrix averaged over a small dispersion $\delta\omega$:

$$\rho_n^{+-}(t) = \begin{pmatrix} \overline{W_n^+(t)} & i\overline{F_n(t)} \\ -i\overline{F_n^*(t)} & \overline{W_n^-(t)} \end{pmatrix} . \qquad (22)$$

where $W_n^{\pm}(t) = \overline{\left|C_n^{\pm}(t)\right|^2}$, $F_n(t) = \overline{C_n^+(t)C_n^{-*}(t)}$. The overline denotes the averaging over a small dispersion $\delta\omega$

$$\overline{A(\omega,t)} = \frac{1}{2\delta\omega}\int\limits_{\omega-\delta\omega}^{\omega+\delta\omega} A(x,t)\,dx . \qquad (23)$$

To solve (21) we can write that

$$W_n^+ = \overline{\sin^2\omega t}, \quad W_n^- = \overline{\cos^2\omega t}, \quad F_n = \frac{1}{2}\overline{\sin 2\omega t} . \qquad (24)$$

After a simple integration of the averaging (23), for the matrix element (24) we obtain

$$W_n^{\pm}(t) = \frac{1}{2}\left(1\mp f(2\delta\omega t)\cos 2\omega t\right),$$

$$F_n(t) = F_n^*(t) = \frac{1}{2} f(2\delta\omega t), \qquad (25)$$

$$f(2\delta\omega t) = \frac{\sin 2\delta\omega t}{2\delta\omega t} .$$

At small values of time $t \ll \overline{\tau}$ ($\overline{\tau} = 2\pi/\delta\omega$), insufficient for self-chaotization ($f(2\delta\omega t) \approx 1$), we obtain

$$W_n^+(t \ll \overline{\tau}) = \sin^2\omega t, \quad W_n^-(t \ll \overline{\tau}) = \cos^2\omega t,$$

$$F_n(t \ll \bar{\tau}) = \frac{1}{2}\sin 2\omega t \; .$$

Comparing these values with the initial values (24) of the density matrix elements, we see that the averaging procedure (23), as expected, does not affect them. Thus, for small times we have

$$\rho_n^+(t \ll \bar{\tau}) = \begin{pmatrix} \sin^2 \omega t & \dfrac{i}{2}\sin 2\omega t \\ -\dfrac{i}{2}\sin 2\omega t & \cos^2 \omega t \end{pmatrix} . \quad (26)$$

One can easily verify that matrix (26) satisfies the condition $\rho^2(t) = \rho(t \ll \bar{\tau})$, which is a necessary and sufficient condition for the density matrix of the pure state.

On relatively large time intervals $t \geq \bar{\tau}$, in which the self-chaotization of phases takes place, for the matrix elements we should use general expressions (25). The substitution of these expressions for the matrix elements (25) into the density matrix (22) gives

$$\rho(t) = \frac{1}{2}\begin{pmatrix} 1 - f(2\delta\omega t)\cos 2\omega t & if(2\delta\omega t)\sin 2\omega t \\ -if(2\delta\omega t)\sin 2\omega t & 1 + f(2\delta\omega t)\cos 2\omega t \end{pmatrix} . \quad (27)$$

Hence, for times $t \geq \bar{\tau}$ during which the phases get completely chaotized after passing to the limit $\delta\omega t \gg 1$ in (27), we obtain

$$\rho_n^+(t) = \frac{1}{2}\begin{pmatrix} 1 - O(\varepsilon) & iO(\varepsilon) \\ -iO(\varepsilon) & 1 + O(\varepsilon) \end{pmatrix} , \quad (28)$$

where $O(\varepsilon)$ is an infinitesimal value of order $\varepsilon = 1/2\delta\omega t$.

The state described by the density matrix (28) is a mixture of two quantum states ψ_{1n}^+ and ψ_{2n}^+ with equal weights. The comparison of the corresponding matrix elements of matrices (28) and (26) shows that they differ in the terms that play the role of quickly changing

fluctuations. When the limit is $t \geq \overline{\tau}$, fluctuations decrease as $\sim 1/2\delta\omega t$.

Thus the system, which at the time moment $t = 0$ was in the pure state with the wave function ψ_{2n}^{-}, gets self-chaotized with a lapse of time $t > \overline{\tau}$ and passes to the mixed state (28). In other words, the initial moment the system had a certain definite "order" expressed in the form of the density matrix $\rho^{+-}(0) = \begin{pmatrix} 0 & 0 \\ 0 & 1 \end{pmatrix}$. With a lapse of time the system got self-chaotized, the correlation terms (27) appeared in the density matrix. For large times $t >> \overline{\tau}$, a new "order" looking like a macroscopic order, is formed, which is defined by matrix (28).

After a halfperiod, the system passes to the area of nondegenerate states G. In passing through the branch point, there are nonzero probabilities for passages both to the state $ce_{2n}(\varphi)$ and to the state $se_{2n}(\varphi)$. Thus, in the nondegenerate area the mixed state is formed, which is defined by the density matrix

$$\rho_{2n}^{ik}\left(t \sim \frac{T}{2} >> \tau\right) = \frac{1}{2}\begin{pmatrix} 1 & 0 \\ 0 & 1 \end{pmatrix},\tag{29}$$

where i and k mean two levels that correspond to the states $ce_{2n}(\varphi)$ and $se_{2n}(\varphi)$.

As follows from (29), at this evolution stage of the system, the populations of two nondegenerate levels were equalized. It should be noted that though the direct passage (15) between the nondegenerate levels is prohibited, perturbation (14) essentially influences "indirect" passages. Under "indirect" passages we understand a sequence of events consisting of a passage $G \rightarrow G_-$ through the branch point, a set of passages between degenerate states in the area G_-, and the reverse passage through the branch point $G_- \rightarrow G$. The "indirect" passages occurring during the modulation halfperiod $T/2$ result in the equalization (saturation) of two nondegenerate levels.

Thus "indirect" passages are directly connected with a quantum chaos. Hence, by fixing "indirect" passages we thereby fix the presence of a quantum chaos.

Let us assume that the investigated molecule is a component of gaseous or liquid state. Then the molecular thermal motion, which tries to establish an equilibrium distribution of populations according to Boltzman's law, will be a competing process for the quantum chaos described above. Using thermodynamic terminology, we can say that the considered quantum system is located between two thermostats. One of them with medium temperature T_0 tries to retain thermal equilibrium in the system, while the other, having an infinite temperature, tries to equalize the populations.

An equation describing the change of populations according to the scheme shown in Fig. 7 has the form

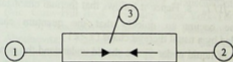$$\frac{dn_i}{dt} = -2W \; n_i - \frac{n_i - n_i^{(0)}}{T_1}, \qquad (30)$$

Fig. 7. A thermodynamic scheme of the process. Subsystem 1 is a usual thermostat having medium temperature T_0; subsystem 2 is a thermostat having an infinite temperature and consisting of the interaction $\hat{H}'(\varphi, \; t)$ (14); the subsystem 3 is the quantum system corresponding to internal rotations of molecules and being able to receive energy from subsystem 2 and to transfer it to subsystem 1.

where $2W$ is probability of indirect passages and T_1 is the time of thermal chaotization. Bloembergen, Parcell and Pound used equation (30) to describe the process of saturation of nuclear magnetic

resonance in solid bodies [11]. For a stationary distribution of populations from (30) we obtain

$$n_i = n_i^{(0)} \frac{1}{1+s} ,$$ (31)

where $s = 2WT_1$ is called the saturation parameter. For $s \gg 1$ indirect passages have a stronger effect on the system than thermal processes.

Thus, along with the conditions $\Omega \ll V_0 / \hbar$, $\Delta T \gg \tau$, $\Delta T \delta \omega \gtrsim 2\pi$, $\delta \omega \ll \omega$, $\Delta T < T$ the condition $s \gg 1$ is a necessary condition for the formation of a quantum chaos.

In the opposite limiting case $s \ll 1$, $n_i \approx n_i^{(0)}$, the quantum chaos will be completely suppressed by thermal motion.

In the case of thermal chaotization time is estimated by the formula $T_1 \approx \frac{d}{\bar{v}}$, where d is the molecule size, $\bar{v} = \sqrt{v^2} = \sqrt{3/2} \cdot (2kT_g / m)^{1/2}$ is a mean motion velocity of molecules. After substituting the numerical values for C_2H_6, we obtain $T_1 \approx 0.3 \cdot 10^{-11} \sqrt{1/T_g}$ s. Hence it follows that thermal chaotization in gaseous ethane occurs so quickly that the quantum chaos is completely veiled by a usual thermal chaos ($s \ll 1$).

In the case of liquid the time T_1 we should understand the mean time of the settled life of a molecule, which is about 10^{-8} s. Relatively large times of relaxation in liquids ensure the fulfilment of the saturation condition ($s \gtrsim 1$). As mentined above, infrared absorption by the molecules of C_2H_6 was observed at frequencies $\sim 289 cm^{-1}$ [9], which corresponds to passages $se_3 \rightarrow ce_3$ between the ground level and the first excited state.

Let us assume that the RF pumping gets involved into the process simultaneously with infrared absorption. If the pumping is so strong that indirect induced by it saturate the working levels $s \gtrsim 1$, then infrared absorption will stop. This is regarded as a manifestation of the quantum chaos.

4

seminar of the theoretical physics chair of Tbilisi State University for valuable suggestions and useful discussions.

REFERENCES

1. R.Z.Sagdeev, D.A.Usikov and G.M.Zaslavsky, Nonlinear Physics.Hardwood, New-York, Acad.Publ., 1988.
2. A.J.Lichtenberg and M.A.Liberman, Regular and Stochastic Motion. Springer-Verlag, New-York, 1983.
3. G.Herzberg, Infrared and Raman Spectra of Polyatomic Molecules. New-York, 1945.
4. W.H.Flyger, Molecular Structure and Dynamics. New-Jersey, 1978.
5. A.Ugulava, L.Chotorlishvili and K.Nickoladze, Phys.Rev. **E70**, 026219, 2004.
6. A.Ugulava, L.Chotorlishvili and K.Nickoladze, Phys.Rev. **E68**, 026216, 2003.
7. A.Ugulava, L.Chotorlishvili and K.Nickoladze, Phys.Rev. **E71**, 056211, 2005.
8. H.Bateman and A.Erdelyi, Higher Transcendental Functions, (Mc. Graw-Hill Book Company, New York-Toronto-London, 1955, **3**, Handbook of Mathematical Functions, edited by M. Abramovitz, National Bureau of Standards Applied Mathematics Series, Doner, New-York, 1964, **55**.
9. T.Shimanouchi, Tables of Molecular Vibrational Frequencies Consolidated, National Bureau of Standards, 1, 1-160, 1972.
10. L.D.Landau and E.M.Lifshitz, Quantum Mechanics, Nonrelativistic Theory. Pergamon Press, Oxford, New York, 1977.
11. N.Bloembergen, E.Parcell and R.Pound, Phys.Rev.**73**, 679, 1948.

Tbilisi State University

ა. უგულავა, ლ. ჭოტორლიშვილი, თ. გვარჯალაძე,
ს. ჩხაიძე

ქაოსი მრავალატომიან მოლეკულებში

დასკვნა

შესწავლილია შინაგანი ბრუნვითი მოძრაობა ეთანის მოლეკულებში რადიოსიხშირული მონოქრომატული დატუმბვის ზემოქმედებისას. ნაჩვენებია, რომ დატუმბვამ შეიძლება გამოიწვიოს გრეხითი რხევებისა და მოლეკულის ნაწილების ერთმანეთის მიმართ რხევის გამმიჯნავი პოტენციური ბარიერის მოდულაცია. ამოცანა დაიყვანება მათიე-შრედინგერის არასტაციონარულ განტოლებაზე. ნაჩვენებია, რომ ბარიერის სიდიდის მოდულაციის გამო შესაძლებელი ხდება არაპირდაპირი გადასვლები შინაგანი ბრუნვითი მოძრაობის ენერგეტიკულ დონეებს შორის, რომელთა შორის პირდაპირი გადასვლები აკრძალულია. ასეთი გადასვლის სიხშირეები შედარებულია ექსპერიმენტზე დამზერილ ინფრაწითელ შთანთქმასთან. ექსპერიმენტული მონაცემები შედარებულია აგრეთვე მცირე რხევების შესაბამის სიხშირეებთან. დამტკიცებულია, რომ ინფრაწითელი შთანთქმა ეთანის მოლეკულების მიერ განპირობებულია არაპირდაპირი გადასვლებით შესაბამის ენერგეტიკულ დონეებს შორის.

CHARGED LEPTON RADIATIVE AND B-MESON DOUBLE RADIATIVE DECAYS IN MODELS WITH UNIVERSAL EXTRA DIMENSIONS

I.I. Bigi[a], G. Chiladze[b], G. Devidze[b], C. Hanhart[b], A. Liparteliani[b], Ulf-G. Meissner[c,d]

ABSTRACT. This paper addresses the role of Large Extra Dimensions in some flavor changing neutral current (FCNC) driven processes. In particular we have investigated radiative decays of charged leptons within models with only one universal extra dimension (UED). Loop contributions with internal fermions and scalars of comparable mass would seem to yield sizeable amplitudes, since the generic quadratic suppression factor is changed into a linear one. Such scenarios can in principle be realized in models with universal extra space dimensions. Yet our calculations of the Kaluza-Klein (KK) contributions to these radiative decays show this expected relative enhancement to disappear due to the near mass degeneracy of the heavy neutrinos from the different generations. In this paper we estimate also the UED contribution to the $B_{s,d} \to \gamma\gamma$ rate and find an enhancement of 3% and 6 %, respectively, over the SM prediction.

1. INTRODUCTION

The highly speculative idea of postulating extra dimensions to explain peculiar features observed in our world with 3+1 space-time dimensions has been revived for a novel reason, namely to provide an alternative approach to the gauge hierarchy problem [1,2]. An interesting feature of this novel insight into the hierarchy problem is that gravitational interactions become sizable not at the Planck scale, but already at the immensely lower scale ~ O(TeV), which in fact

must be considered as the only fundamental scale of nature. TeV scale dynamics in general will be explored directly by the LHC starting in 2007. The renaissance of multidimensional models is mainly due to superstring theories and their generalization, M-theory. It is the only consistent quantum theory known today that incorporates, at least in principle, all interactions including gravity. Both superstring and M-theory most naturally are formulated in $d = 10$ and $d = 11$ dimensions.

Since the extra dimensions can possess very different characteristics, models involving them can lead to vastly different phenomenologies. Those characteristics refer not only to the size and other topological features of the extra dimensions (and whether they are of the space or time variety), but also to the fields that populate them. The options range from where only the graviton can propagate through the extra dimension(s) to where all fields can, in the latter case one talks about universal extra dimensions (UED) [3].

A remarkable feature of UED models [3] is the conservation of the so-called Kaluza-Klein (KK) parity, which leads to the absence of tree-level KK contributions to transitions at low energies, namely at scales $\mu << 1/R$ with R denoting the compactification radius for extra dimensions. KK parity resembles R parity, which is conserved in many supersymmetric models. In particular KK parity prohibits the production of single KK modes off the interaction of ordinary particles.

Transitions driven by FCNC like $K^0 - \bar{K}^0$, $B^0 - \bar{B}^0$ oscillations and $B_{s,d} \to \gamma\gamma$ are highly suppressed in the Standard Model (SM).

Radiative τ and μ decays are even SM forbidden. New Physics contributions in general and KK ones in particular thus have (in principle) a considerably enhanced chance to make their presence felt in such processes.

In this paper we investigate lepton flavor violating radiative decays of charged leptons within models with only one universal extra dimension and also estimate their contributions to $B_{s,d} \to \gamma\gamma$ transitions, which are allowed though suppressed in the SM. The article is organized as follows: after summarizing in Section 2 information about the UED model of Appelquist, Cheng and Dobrescu (ACD) [3] relevant for our calculations we devote Sections

3 and 4 to the study of charged lepton decays $l_i \rightarrow l_j \gamma$ and $B_{s,d} \rightarrow \gamma\gamma$, respectively, in the framework of the same model, before formulating our conclusions in Section 5. Some useful formulas are collected in the Appendix.

2. THE ACD MODEL

Modern models with extra space-time dimensions have received a great deal of attention because the scale at which dimensional effects become relevant could be around a few TeV [1,2,3]. If so, they could be searched for directly at the LHC. The first proposal for using large (TeV) extra dimensions in the SM with gauge fields in the bulk and matter localized on the orbifold fixed points was developed in Ref. [4]. The models with extra space-time dimensions can be built in several ways. Among them the following approaches are the most actively pursued ones: i) The ADD model of Arcani-Hammed, Dimopoulos and Dvali [1], where all elementary fields except the graviton are localized on a brane, while the graviton propagates in the whole bulk. ii) The RS model of Randall and Sundrum with warped 5-dimensional space-time and nonfactorized geometry [2]. iii) The ACD model of Appelquist, Cheng and Dobrescu (also referred to as model with Universal Extra Dimensions (UED)), where all fields can move in the whole bulk [3].

In UED scenarios SM fields are thus described as nontrivial functions of all space-time coordinates. For bosonic fields one simply replaces all derivatives and fields in the SM Lagrangian by their 5-dimensional counterparts. These are the $U(1)_Y$ and $SU(2)_L$ gauge fields as well as the $SU(3)_C$ gauge fields from the QCD sector. The Higgs doublet is chosen to be even under P_5 (P_5 is the parity operator in the five dimensional space) and possesses a zero mode. Note that all zero modes remain massless before the Higgs mechanism is applied. In addition we should note that as a result of action of the parity operator the fields receive additional masses $\sim n/R$ after dimensional reduction and transition to the four dimensional Lagrangians; n is a positive integer denoting the KK mode.

In the five dimensional ACD model the same procedure for gauge fixing is possible as in the models in which fermions are localized on

the 4-dimensional subspace. With the gauge fixed, one can diagonalize the kinetic terms of the bosons and finally derive expressions for the propagators. Compared to the SM, there are additional Kaluza-Klein (KK) mass terms. As they are common to all fields, their contributions to the gauge boson mass matrix is proportional to the unity matrix. As a consequence, the electroweak angle remains the same for all KK-modes and is the usual Weinberg angle θ_W. Because of the KK-contribution to the mass matrix, charged and neutral Higgs components with $n \neq 0$ no longer play the role of Goldstone bosons. Instead, they mix with $W_5^\pm$ and θ_W to form -- in addition to the Goldstone modes θ_W and $G_{(n)}^\pm$ -- three physical states $a_{(n)}^0$ and $a_{(n)}^\pm$. Below we will study the impact of these new *charged* states.

The interactions of ordinary charged leptons with pairs of KK scalars and neutrinos ($a_{(n)}$, $\nu_{k(n)}$) is given by

$$L(l_j\nu_{i(n)}a_{(n)}^+) = \overline{l_j}(c_L P_L + c_R P_R)U_{ij}\nu_{i(n)}a_{(n)}^+ + h.c. \quad (1)$$

with

$$P_{L,R} = \frac{1 \mp \gamma_5}{2}, \quad c_L = -(g_2 nm(l_j))/(\sqrt{2}M_{W(n)}),$$

$$c_R = -(g_2 M_W)/(\sqrt{2}M_{W(n)}),$$

where g_2 is the SU(2) coupling for the weak interactions, n labels the KK towers (e.g. $M_{W(n)}$ is the mass for the n-th KK-mode: $M_{W(n)}^2 = M_W^2 + n^2/R^2$) and U_{ij} is an element in the MNS matrix, the leptonic analogue of the CKM matrix.

The complete list of Feynman rules for models with only one universal extra dimension has been given in [5].

The Lagrangian responsible for the interaction of the charged scalar KK towers $a_{(n)}^-$ with the ordinary down quarks, is as follows

η)

$$L = \frac{g_2}{\sqrt{2}M_{W(n)}} \bar{Q}_{i(n)} \left(C_L^{(1)} P_L + C_R^{(1)} P_R \right) a_{i(n)}^+ d_j +$$

$$+ \frac{g_2}{\sqrt{2}M_{W(n)}} \bar{U}_{i(n)} \left(C_L^{(2)} P_L + C_R^{(2)} P_R \right) a_{i(n)}^+ d_j. \quad (2)$$

with [5]

$$C_L^{(1)} = -m_3^{(i)} V_{ij}, \quad C_L^{(2)} = m_4^{(i)} V_{ij}, \quad C_R^{(1)} = M_3^{(i,j)} V_{ij},$$

$$C_R^{(2)} = -M_4^{(i,j)} V_{ij}$$

$$M_{W(n)}^2 = m^2 (a_n^2) = M_W^2 + \frac{n^2}{R^2}; \quad (3)$$

here V_{ij} are elements of the CKM matrix. The mass parameters in (3) are defined as

$$m_3^{(i)} = -M_W c_{i(n)} + \frac{n}{R} \frac{m_i}{M_W} s_{i(n)}, \quad M_3^{(i,j)} = \frac{n}{R} \frac{m_j}{M_W} c_{i(n)},$$

$$m_4^{(i)} = M_W s_{i(n)} + \frac{n}{R} \frac{m_i}{M_W} c_{i(n)}, \quad M_4^{(i,j)} = \frac{n}{R} \frac{m_j}{M_W} s_{i(n)}; \quad (4)$$

here M_W and the masses of up (down)-quarks $m_i(m_j)$ on the right hand side of (4) are zero mode masses and $c_{i(n)}, s_{i(n)}$ denote the sine and cosine of the fermion mixing angles, respectively

$$tg \, 2\alpha_{f(n)} = \frac{m_f}{n/R}, \quad n \geq 1. \quad (5)$$

The masses for the fermions are calculated as

$$m_{f(n)} = \sqrt{\frac{n^2}{R^2} + m_f^2} \ .$$

(6)

In the phenomenological applications we use the restriction $n/R > 250$ GeV and hence we assume that all the fermionic mixing angles except $\alpha_{t(n)}$ are zero.

3. RADIATIVE DECAYS $L_i \rightarrow l_j \gamma$ OF CHARGED LEPTONS

In [6] a mainly model independent analysis of $\mu \rightarrow e\gamma$ and $\tau \rightarrow \mu \gamma$ on the one-loop level has been performed. An important statement is that when the masses of the internal scalar and fermion masses are comparable, the transition amplitude becomes considerably enhanced over what one usually expect. The authors state that such a situation arises in UED theories. We will analyze the situation in more detail specifically in theories with only one extra dimension [3].

Real decay processes, where the photon has to be on-shell represent a magnetic transition described by two form factors:

$$A(l_i \rightarrow l_j\gamma) = \varepsilon^\mu(k)\bar{u}_j(p_2)\sigma_{\mu\nu}k^\nu(F_{2V} + F_{2A}\gamma_5)u_i(p_1)$$

(7)

$u_{i,j}$ denote the lepton spinors with momenta p_i and $k = p_1 - p_2$ and $\varepsilon^\mu(k)$ the photon polarization vector.

For completeness we give also the amplitude for such transitions with an *off* shell photon (or Z^0), which contains four additional form factors:

$$A(l_i \rightarrow l_j\gamma) = \varepsilon^\mu(k)\bar{u}_j(p_2)[(F_{1V} + F_{1A}\gamma_5)\gamma_\mu +$$

$$+ i\sigma_{\mu\nu}k^\nu(F_{2V} + F_{2A}\gamma_5) + k_\mu(F_{3V} + F_{3A}\gamma_5)]u_i(p_1)$$

(8)

The specifics of the underlying dynamics then determine the form factors $F_{i'}$ and F_{iA}. 'Switching on' one universal extra dimension expands the particle content of the model. In particular, KK-modes of the charged scalar boson are real particles in this case [3,5]. The relevant Feynman diagrams are shown in Fig. 1. Their contributions to $l_i \to l_j \gamma$ are explicitly calculated in this section.
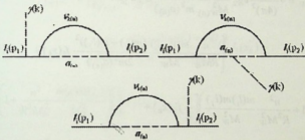

Fig.1. $l_i \to l_j \gamma$ decay in the model with Universal Extra Dimensions (the dashed line in the loops correspond to the charged KK towers $a^\pm_{(n)}$, while the solid lines in the loops are for neutrino KK towers).

One can conclude from the expressions for the masses of the neutrino and physical scalar 'towers'

$$m^2(\nu_{k(n)}) = m^2(\nu_k) + \frac{n^2}{R^2}, \qquad m^2(a_{(n)}) = M_W^2 + \frac{n^2}{R^2} \qquad (9)$$

that they are comparable already for the first excited mode $(n=1)$, because very rough estimates for the compactification radius tell us: $1/R > 250$ GeV.

Explicit calculations yield for the form factors $F_{2V,2A}$ - relevant for $l_i \to l_j \gamma$ - and the other four form factors $F_{W,1A}$ and $F_{W,3A}$ (which become relevant for $l_i \to l_j l \bar{l}$)

$$F_W = -\frac{i}{(4\pi)^2} e g_2 \frac{M_W^2}{M_{W(n)}^2} \frac{k^2}{m^2(a_{(n)})} U_{ik} U_{jk}^* \times$$

$$\times \left\{ \frac{n}{R M_W} \frac{m(\nu_{k(n)})}{M_W} \frac{(m(l_i) + m(l_j))^2}{2 m^2(a_{(n)})} f_1(x_k) + \right. \qquad (10a)$$

$$\left(1 + \frac{n^2}{R^2 M_W^2} \frac{m(l_i) m(l_j)}{M_W^2}\right) \left[\frac{1}{4} f_2(x_k) + \right.$$

$$+ \frac{m^2(l_i) + m(l_i) m(l_j) + m^2(l_j)}{m^2(a_{(n)})} f_3(x_k) + \frac{1}{6} \frac{k^2}{m^2(a_{(n)})} f_4(x_k) \right] \right\},$$

$$F_{2V} = \frac{1}{2} \frac{i}{(4\pi)^2} e g_2 \frac{M_W^2}{M_{W(n)}^2} \frac{m(l_i) + m(l_j)}{m^2(a_{(n)})} U_{ik} U_{jk}^* \times$$

$$\times \left\{ \frac{n}{R M_W} \frac{m(\nu_{k(n)})}{M_W} \left(-f_5(x_k) + \frac{k^2}{m^2(a_{(n)})} f_1(x_k) - \right. \right.$$

$$- \frac{m^2(l_i) + m^2(l_j)}{m^2(a_{(n)})} f_6(x_k) \right) + \left(1 + \frac{n^2}{R^2 M_W^2} \frac{m(l_i) m(l_j)}{M_W^2}\right) \times$$

$$\times \left(-\frac{1}{2} f_7(x_k) + \frac{k^2}{m^2(a_{(n)})} f_3(x_k) - \right.$$

$$-\frac{2m^2(l_i) + 2m^2(l_j) + 3m(l_i)m(l_j)}{3m^2(a_{(n)})} f_4(x_k) \Bigg\} \quad (10b)$$

$$F_W = -\frac{1}{2}\frac{i}{(4\pi)^2} eg_2^2 \frac{M_W^2}{M_{W(n)}^2} \frac{m^2(l_i) - m^2(l_j)}{m^2(a_{(n)})} U_{ik} U_{jk}^* \times$$

$$\times \Bigg\{ \frac{n}{RM_W} \frac{m(\nu_{k(n)})}{M_W} \frac{m(l_i) + m(l_j)}{m^2(a_{(n)})} f_1(x_k) +$$

$$+ \Bigg(1 + \frac{n^2}{R^2 M_W^2} \frac{m(l_i)m(l_j)}{M_W^2} \Bigg) \Bigg[\frac{1}{2} f_2(x_k) +$$

$$+ \frac{2(m^2(l_i) + m(l_i)m(l_j)) + m^2(l_j)}{m^2(a_{(n)})} f_3(x_k) + \frac{1}{3}\frac{k^2}{m^2(a_{(n)})} f_4(x_k) \Bigg] \Bigg\},$$

where

$$x_k = \frac{m^2(\nu_{k(n)})}{m^2(a_{(n)})} \qquad (11)$$

and summation over the tower indices n is assumed in Eqs.(10a-10c); the functions $f(x_n)$ are given in the Appendix. The axial form-factors are related to the corresponding vector ones by:

$$F_A(m(l_i), \quad m(l_j)) = F_V(m(l_i), \quad -m(l_j)). \qquad (12)$$

Eqs.(10a-10c) demonstrate explicitly the general relation between form factors:

$$(m(l_i) - m(l_j))F_V = -k^2 F_{\mathcal{V}} \qquad (13)$$

Using Eq.(7) we obtain for the decay width:

$$\Gamma(l_i \to l_j \gamma) = \frac{|F_{2V}|^2 + |F_{2A}|^2}{8\pi} \left(\frac{m^2(l_i) - m^2(l_j)}{m(l_i)} \right)^3 . \quad (14)$$

Let us note that the ratio $x_n = m^2(\nu_{k(n)})/m^2(a_{(n)})$ is close to unity for all n, namely $0.9 < x_k < 1$:

$$x_k = \frac{m^2(\nu_{k(n)})}{m^2(a_{(n)})} = \frac{m^2(\nu_k) + \frac{n^2}{R^2}}{M_W^2 + \frac{n^2}{R^2}} . \quad (15)$$

With the rough estimate for the compactification radius ($1/R > 250\text{GeV}$) we have already for the first KK-mode $x_k > 0.9$. Noting that the masses of the scalar and fermion towers are close to each other for the same n, we can simplify Eq.(10b):

$$F_{2V} = \frac{1}{2} \frac{i}{(4\pi)^2} e g_2^2 \frac{M_W^2}{M_{W'}^2} \frac{m(l_i)}{m(a_{(n)})} U_{ik} U_{jk}^* \times$$

$$\times \left\{ \frac{n}{RM_W} \frac{m(\nu_{k(n)})}{M_W} \left(-\frac{1}{4} + \frac{x_k}{12} \right) + \frac{x_k}{60} \right\}, \quad (16)$$

and thus

$$Br(l_i \to l_j \gamma) = \frac{6\alpha}{\pi} \frac{M_W^8}{M_{W'(n)}^8} \left(U_{ik} U_{jk}^* f(x_k) \right)^2, \quad (17)$$

In four-dimensional models with small Dirac neutrino masses the ratio of neutrino mass square differences to the W-boson square mass serves as a highly efficient *suppression factor* for $l_i \to l_j \gamma$. Eq. 16 exhibits an apparently *linear* dependence on the neutrino to W mass ratio for the exchange of KK towers in the loops. This might be due

at first as leading to a very considerable enhancement of the $l_i \to l_j \gamma$ amplitude. This conclusion, however, would be fallacious. For upon explicit substitution of Eq.9 for the KK masses into the form factor expression in Eq.16 the *quadratic* dependence re-emerges:

$$\frac{n}{RM_W} U_{ik} U_{jk}^\star \frac{m(v_{k(n)})}{M_W} =$$

$$= \frac{n}{RM_W} U_{ik} U_{jk}^\star \left(\frac{n}{R} + \frac{rm^2(v_k)}{2n} \right) \frac{1}{M_W} = U_{ik} U_{jk}^\star \frac{m^2(v_k)}{2M_W^2}. \quad (18)$$

The initial appearance of a merely linear suppression thus disappears due to the near-degeneracy of the masses for neutrino KK-towers from different generations. For example, we have for two neutrino generations:

$$m(v_{\mu(n)}) - m(v_{e(n)}) =$$

$$= (m(v_\mu) - m(v_e)) \frac{m(v_\mu) + m(v_e)}{2n/R} << m(v_\mu) - m(v_e) \quad (19)$$

In the end the following expression emerges for the branching ratio:

$$(l_i \to l_j \gamma) = \frac{3\alpha}{32\pi} \frac{M_W^4}{M_{K^*}^4} \left(U_{ik} U_{jk}^\star \frac{m^2(v_k)}{M_W^2} \right)^2, \quad (20)$$

This expression shows that it cannot enhance the SM result [7-12] significantly:

$$\mathrm{Br}(l_i \to l_j \gamma)_{CM} = \frac{3\alpha}{32\pi} \left(U_{ik} U_{jk}^\star \frac{m^2(v_k)}{M_W^2} \right)^2, \quad (21)$$

In the slightly extended SM with massive left-handed neutrinos lepton flavor violating processes like of $\mu \to e\gamma$ and $\tau \to \mu\gamma$ are extremely suppressed. For example, taking into consideration the data from modern neutrino experiments [13], the branching ratio for $\mu \to e\gamma$ is predicted to be as low as $7 \cdot 10^{-57}$ [7-12] in the SM.

A planned experiment is expected to lower the existing upper bound $Br(\mu \to e\gamma) < 1.2 \cdot 10^{-11}$ to the $10^{-13} - 10^{-14}$ levels [14].

4. $B_{S,D} \to \gamma\gamma$ DECAY IN MODELS WITH ONE UNIVERSAL EXTRA DIMENSION

Detailed studies of the decays of strange hadrons were instrumental in developing the Standard Model (SM). Recent findings on B decays – in particular the CP asymmetry observed in $B \to \psi K_S$ by the BABAR and BELLE collaborations at the B factories – represent a striking confirmation of the SM [38]. Yet they do not invalidate the various theoretical arguments pointing to its incompleteness, i.e. the existence of physics beyond the SM (BSMP). If anything they even strengthen the case for a new paradigm. History might well repeat itself in the sense that future detailed studies of the decays of beauty and charm hadrons and tau leptons will reveal the intervention of BSMP.

The BABAR and BELLE experiments running at the two B factories at SLAC in the USA and at KEK in Japan are producing the huge high-quality data sets required for such searches for BSMP. There is even a proposal in Japan for building a Super-B factory with much higher luminosity; similar plans are being pursued in Italy. Further information will be gained from the tau-charm factories at Cornell University in the US and at Beijing in China.

Some experimental evidence for an incompleteness of the CKM description has actually merged in the CP asymmetry in $B \to \phi K_S$ and similar channels. It also points towards radiative and related B decays as promising areas for search for BSMP.

Exploration of B-physics, including B-meson rare decays is one of the central issues of the physical programs at accelerator facilities

operating now or soon getting online. The process $B_{s,d} \to \gamma\gamma$, which is the subject of this section, has an unusual experimental signature that can be searched for at least at B factories. It should be noted that the two photon final states produced in this process can be CP even as well as CP odd. This feature might allow searches for nondiffractive sources of CP violation in B-physics. In general the process $B_{s,d} \to \gamma\gamma$ is sensitive to BSMP effects. The experimental feasibility has stimulated efforts of theoretical groups as well [15-32]. The decay rates have been calculated within the SM with and without QCD corrections, in multi-Higgs doublet as well as supersymmetric models.

In the SM $B_{s,d} \to \gamma\gamma$ first arise at the one loop level with the exchange in the loops by up-type quarks and W-bosons [15-19]. SM predictions for the branching ratios are of the order of 10^{-7} (10^{-9}).

It has been shown that in extended versions of the SM (multi-Higgs doublet and supersymmetric models) one could reach branching ratios as large as $Br(B_{s,d} \to \gamma\gamma) \sim 10^{-6}$ depending on the parameters of the models. This enhancement was achieved mainly due to exchange of charged scalar Higgs particles within the loop. There exists an analogous possibility in other exotic models as well for the scalar particle exchange inside the loop, which could enhance this process. For example, the Appelquist, Cheng and Dobrescu (ACD) model with only one universal extra dimension [3] presents us with such an opportunity. One should note that in this above approach towers of charged Higgs particles arise as real objects with definite masses, not as fictitious (ghost) fields.

In this Section we calculate the contributions from these real scalars to $B_{s,d} \to \gamma\gamma$. The Feynman graphs, describing the contributions of scalar physical states to process under consideration, are shown in Fig.2.

The amplitude for the decay $B_{s,d} \to \gamma\gamma$ has the form

$$T(B \to \gamma\gamma) = \varepsilon_1^\mu(k_1)\, \varepsilon_2^\nu(k_2)[A g_{\mu\nu} + iB\varepsilon_{\mu\nu\alpha\beta}k_1^\alpha k_2^\beta] \quad (22)$$

This equation holds after gauge fixing for the final photons which we have chosen as

$$\varepsilon_1 k_1 = \varepsilon_2 k_2 = \varepsilon_1 k_2 = \varepsilon_2 k_1 = 0 .$$

This is possible because in the CM frame both final photons are collinear, where ε_1 and ε_2 are photon polarization vectors, respectively.
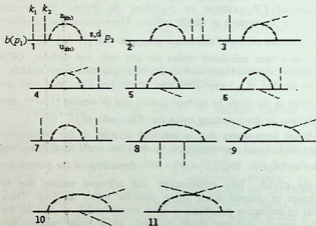

Fig.2. Double radiative B-meson decay $B_{s,d} \to \gamma\gamma$ in the theory with only one extra universal dimension (the dashed line in the loops correspond to the charged KK towers $a_{(n)}^{\pm}$), while the solid lines in the loops are for up-quark KK towers).

The gauge condition of Eq.(23) together with energy-momentum conservation leads to

$$\varepsilon_i P = \varepsilon_i p_1 = \varepsilon_i p_2 = 0 ,$$

(24)

where

$$P = k_1 + k_2 \quad \text{and} \quad p_1 = p_2 + k_1 + k_2. \tag{25}$$

Let us write down some useful kinematical relations resulting from Eqs.(23-25):

$$(k_1 k_2) = (Pk_1) = (Pk_2) = \frac{1}{2}M_B^2, \quad (p_1 p_2) = -m_b m_{s(d)}, \quad (Pp_1) = m_b M_B,$$

$$(p_1 k_1) = (p_1 k_2) = \frac{1}{2}m_b M_B, \quad (p_2 k_1) = (p_2 k_2) = -\frac{1}{2}m_{s(d)}M_B,$$

$$(Pp_2) = -m_{s(d)}M_B. \tag{26}$$

The total contributions into CP even (A) and CP odd (B) amplitudes from Eq.(22) are calculated as sums of the appropriate contributions of the diagrams in Fig.2 corresponding to a tower of scalar particle contributions in the ACD model with only one extra dimension. Let us note that we used the following formula for the hadronic matrix elements:

$$\left\langle 0\middle|\bar{s}\gamma_\mu\gamma_5 b\middle|B_s(P)\right\rangle = -if_B P_\mu. \tag{27}$$

Apart from one particle reducible (1PR) diagrams, one particle irreducible (1PI) ones contribute to the amplitudes, and hence, to their CP even (A) and CP odd (B) parts. We should note that each of the 1PI contributions is finite. Let us discuss these contributions in more details. In the SM only one 1PI diagram (the one with the W-boson exchange in the loop, when both photons are emitted by virtual up-type quarks) gives a contribution of order $\sim 1/M_W^2$. In Ref.[33] it was observed that diagrams with light quark exchanges contribute as $\sim 1/M_W^2$, while diagrams containing the heavy quarks are of order $\sim 1/M_W^4$. In the ACD model the contributions of such diagrams are also of order $\sim 1/M_W^4$ because the estimate for all KK-tower masses,

including the ones exchanged in the loops, is given in units of $1/R \sim 250\,GeV$ [34]. Similar considerations show that all the 1PI diagrams existing in the ACD model are of order $\sim 1/M_W^4$. Thus, the leading 1PI diagrams are negligible and we do not consider them.

The total contributions to the $B \rightarrow \gamma\gamma$ decay amplitudes are:

$$A = \frac{i}{(4\pi)^2} \frac{1}{4} e^2 g_2^2 f_B \frac{Q_d}{M_{W(n)}^2} \frac{1}{m^2(a_{(n)}^{\pm})} \frac{m_b^3}{m_{s(d)}} V_{is(d)}^* V_{ib} \times$$

$$\times \left\{ \frac{n}{RM_W} m_3^{(i)} m_{i(n)} c_{i(n)} f_8(x_i) + \right.$$

$$\left. + (m_3^{(i)})^2 - \frac{n^2}{R^2 M_W^2} m_b m_{s(d)} c_{i(n)}^2) \frac{1}{2} f_7(x_i) \right\}.$$

$$B = \frac{i}{(4\pi)^2} \frac{1}{2} e^2 g_2^2 f_B \frac{Q_d}{M_{W(n)}^2} \frac{1}{m^2(a_{(n)}^{\pm})} \frac{m_b}{m_{s(d)}} V_{is(d)}^* V_{ib} \times$$

$$\times \left\{ \frac{n}{RM_W} m_3^{(i)} m_{i(n)} c_{i(n)} f_8(x_i) + \right.$$

$$\left. + (m_3^{(i)})^2 + \frac{n^2}{R^2 M_W^2} m_b m_{s(d)} c_{i(n)}^2) \frac{1}{2} f_7(x_i) \right\}, \quad (28)$$

where

$$f_8(x) = \frac{-5x^2 + 8x - 3 + 2(3x - 2)\ln x}{6(1-x)^3},$$

$$f_7(x) = \frac{-2x^3 - 3x^2 + 6x - 1 + 6x^2 \ln x}{6(1-x)^4},$$

$$x_i = \frac{m^2(u_{i_{(n)}})}{m^2(a^z_{(o)})} \quad (29)$$

As is obvious from Fig.2, the correct calculation must include the crossed diagrams (not shown on Fig.2). In the kinematics we use, cf. Eqs.(23)-(26), this leads to a factor 2 for all amplitudes, except for the one given by diagram 11. However, diagram 11 belongs to the class of 1PI diagrams. As it was stated above, those contributions are order $\sim 1/M_W^4$ and thus negligible compared to those from the 1PR diagrams.

On the other hand, using the unitarity of the CKM matrix, the amplitude for double radiative B-meson decay can be rewritten as:

$$T = \sum_{i=u,c,t} \lambda_i T_i = \lambda_t \left[T_t - T_c + \frac{\lambda_u}{\lambda_t}(T_u - T_c) \right]. \quad (30)$$

Let us note that we restricted ourselves to calculating the leading order terms of $\sim 1/M_W^2$ from the up-quark KK-towers. In this approximation it turns out that the $u_{(n)}$ and the $c_{(n)}$ towers have equal contributions. Therefore, the expressions for the amplitudes have a simpler form than before:

$$A = \lambda_t (A_{t(n)} - A_{c(n)}), \qquad B = \lambda_t (B_{t(n)} - B_{c(n)}) \quad (31)$$

Furthermore, it is easy to obtain from Eq.(22) the expression for the $B \to \gamma\gamma$ decay partial width:

$$\Gamma(B \to \gamma\gamma) = \frac{1}{32\pi M_B} \left[4|A|^2 + \frac{1}{2} M_B^4 |B|^2 \right]. \quad (32)$$

Now we are in the position to compare the ACD contribution to the decay with that of the SM.

Namely, let us consider the ratio

$$\frac{\Gamma(B_{s(d)} \to \gamma\gamma)_{ACD}}{\Gamma(B_{s(d)} \to \gamma\gamma)_{CM}} = \frac{24}{Q_d^2} \frac{M_W^4}{M_{W'(n)}^4} \frac{M_W^2 n^2/R^2}{m^4(a_n^2)} \times$$

$$\times \left[\frac{\frac{m_l^{(\nu)} m_{l(n)}}{M_W^2} c_{l(n)} f_8(x_{l(n)}) + \frac{n}{RM_W} f_8(x_{c(n)})}{4 \left(C(x_t) + \frac{23}{3}\right)^2 + 2 \left(C(x_t) + \frac{23}{3} + 16 \frac{m_{s(d)}}{m_b}\right)^2} \right] \cdot \quad (33)$$

where

$$C(x) = \frac{22x^3 - 153x^2 + 159x - 46}{6(1-x)^3} + \frac{3(2-3x)}{(1-x)^4} \ln x,$$

$$x_t = \frac{m_t^2}{M_W^2}. \quad (34)$$

Rough numerical estimates show that the pure UED contributions to $B_s \to \gamma\gamma$ and $B_d \to \gamma\gamma$ enhance the SM estimate by about 3% and 6 %, respectively.

CONCLUSION

In this paper we have investigated lepton flavor violating radiative decays of charged leptons $l_i \to l_j\gamma$ within models with only one universal extra dimension and have estimated also their contributions to the highly suppressed SM rates for $B_{s,d} \to \gamma\gamma$.

Planned experiment are expected to lower the existing upper bound $Br(\mu \to e\gamma) < 1.2 \cdot 10^{-11}$ to the $10^{-13} - 10^{-14}$ levels [14]. There are bad news and good news from our analysis:

• The bad news are that UED models with only one additional spatial dimension cannot raise $Br(\mu \to e\gamma)$ into a range, where it could ever be observable.

74

- The good news are that if $\mu \to e\gamma$ is ever observed, it must have a completely different origin.

The pure UED contribution to the $B_s \to \gamma\gamma$ $[B_d \to \gamma\gamma]$ rate is 3% [6%] of the SM estimates of $Br(B_s \to \gamma\gamma) \sim 10^{-7}$ and $Br(B_d \to \gamma\gamma) \sim 10^{-9}$, i.e. rather small. It is quite possible that the as yet uncalculated radiative QCD corrections could enhance these rates further and that they become observable at a Super-B factory. Then they might be relevant for the central goal of B physics studies to not only discover New Physics, but also identify its salient features.

ACKNOWLEDGEMENTS

APPENDIX

The functions $f(x_i)$ appearing in Eqs.(10a-10c,16) are given by:

$$f_1(x) = \frac{1 - 9x - 9x^2 + 17x^3 - 6x^2(3+x)\ln x}{36(1-x)^5},$$

$$f_2(x) = \frac{2 - 9x + 18x^2 - 11x^3 + 6x^3 \ln x}{18(1-x)^4},$$

$$f_3(x) = \frac{1 - 8x + 36x^2 + 8x^3 - 37x^4 + 12x^3(4+x)\ln x}{144(1-x)^6},$$

$$f_4(x) = \frac{3 - 20x + 60x^2 - 120x^3 + 65x^4 + 12x^5 - 60x^4 \ln x}{240(1-x)^6},$$

$$f_5(x) = \frac{x^2 - 1 - 2x \ln x}{2(1-x)^3}, \quad f_6(x) = \frac{-1 - 9x + 9x^2 + x^3 - 6x(1+x)\ln x}{6(1-x)^5},$$

$$f_7(x) = \frac{-1 + 6x - 3x^2 - 2x^3 + 6x^2 \ln x}{6(1-x)^4},$$

$$f(x_k) = \frac{n}{RM_W} \frac{m(v_{k(n)})}{M_W} \left(-\frac{1}{4} + \frac{x_k}{12} \right) + \frac{x_k}{60}.$$

REFERENCES

1. N. Arkani-Hamed, S. Dimopoulos and G. Dvali, Phys. Lett. B **429**, 1998, 263; hep- ph/9803315; I. Antoniadis, N. Arkani-Hamed, S. Dimopoulos and G. Dvali, Phys. Lett. B **436**, 1998, 256; hep-ph/9804398.

2. L. Randall, R. Sundrum, Phys. Rev. Lett. **83**, 1999, 3370; hep-ph/9905221; L. Randall, R. Sundrum, Phys. Rev. Lett. 83, 1999, 4690; hep- ph/9906064.

3. T. Appelquist, H. C. Cheng and B. A. Dobrescu, Phys. Rev. D **64**, 2001, 035002; hep-ph/0012100.

4. I. Antoniadis, Phys. Lett. B **46**, 1990, 317.

5. A. J. Buras, M. Spranger and A. Weiler, Nucl. Phys. B 660, 2003, 225; hep-ph/0212143.

6. Bo He, T.P. Cheng and Ling-Fong Li, Phys. B **553**, 277, 2003.

7. S.T. Petcov Yad. Fiz. **25**, 641, 1977.

8. Marciano W. J., Sanda A. I., Phys. Lett. B **67**, 1977, 303.

9. Lee B.W., Shrock R., Phys. Rev. D **16**, 1977, 1445.

10. Cheng T.P., Li L.-F., Phys. Rev. D **16**, 1977, 1425.

11. S. M. Bilenky, S. T. Petcov and B. Pontecorvo, Phys. Lett. B 67, 1977, 309.

12. G.G. Volkov, A.G. Liparteliani, V.A. Monich, Yu.P. Nikitin Yad. Fiz. **27**, 1978, 1395

13. M. Maltoni, T. Schwetz, M. A. Tortola and J. W. F. Valle, New J. Phys. 6, 2004, 122 .

14. Brooks M.L. et al., (MEGA Collab.), Phys. Rev. Lett. **83**, 1999, 1521; Ritt S. et al., (MEGA Collab.), a research proposal PSI-R-9905 "Search for down to branching ratio", http://meg.web.psi.ch.

15. G.L. Lin, J. Liu and Y.P. Yao, Phys. Rev. D **42** , 1990, 2314.

16. H. Simma and D. Wyler, Nucl. Phys. B **344**, 1990, 283.

17. S. Herrlich and J. Kalinowski, Nucl. Phys. B **381**, 1992, 501.

18. G. G. Devidze, G. R. Dzhibuti and A.G. Liparteliani, Nucl. Phys. B 468, 1996, 241.

19. G. G. Devidze, G. R. Dzhibuti and A.G. Liparteliani, Phys. Atom. Nucl. **59**, 1996, 1948.

20. C.-H. V. Chang, G. L. Lin, and Y. P.Yao, Phys. Lett. B **415**, 1997, 395; hep-ph/9705345.

21. G. Hiller, E.O. Iltan, Phys. Lett. B **409**, 1997, 425; hep-ph/9705345.

22. T. M. Aliev, G. Hiller and E. O. Iltan, Nucl. Phys. B **515**, 1998, 321; hep-ph/9708382.

23. M. Boz, E. O. Iltan, Phys. Rev. D **62**, 2000, 054010; hep-ph/9012509.

24. T. M. Aliev and G. Turan, Phys. Rev. D **48**, 1993, 1176.

25. Y. Dincer and L. M. Sehgal, Phys. Lett. B **521**, 2001, 7; hep-ph/0108144.

26. J. O. Eeg, K. Kumericki and I. Picek, Fizika B**10**, 2001, 285; hep-ph/0203055.

27. J. Cao, Z. Xiao and G. Lu, Phys. Rev. D **64**, 2001, 014012; hep-ph/0103154.

28. L. Reina, G. Ricciardi and A. Soni, Phys. Rev. D **56**, 1997, 5805; hep-ph/9706253.

29. S. W. Bosch and G. Buchalla, JHEP 0208, 2002 054; hep-ph/0208202.

30. S. Bertolini and J. Matias, Phys. Rev. D **57**, 1998, 4197; hep-ph/9709330.

31. G. G. Devidze and G. R. Dzhibuti, Phys. Lett. B **429**, 1998, 48.

32. G. G. Devidze and G. R. Dzhibuti, Phys. Atom. Nucl. **63**, 2000, 310.

33. M. K. Gaillard and B. W. Lee, Phys. Rev. D **10**, 1974, 897.

34. A. J. Buras, A. Poschenrieder, M. Spranger, A. Weiler, Nucl. Phys. B **678**, 2004, 455; hep-ph/0306158

35. A. J. Buras, A. Poschenrieder, M. Spranger, A. Weiler, Published in eConf C030452: WG302, 2003; hep-ph/0307202.

36. T. Inami and C. S. Lim, Progr. Theor. Phys. **65**, 1981, 297.

37. Particle Data Group, http://pdg.lbl.gov

38. I.I. Bigi and A.I. Sanda, Nucl. Phys. B **193**, 1981, 85.

a) University of Notre Dame, Department of Physics

b) Institute of High Energy Physics and Informatization, Tbilisi State University

c) Institut fur Kernphysik (Theorie), Forschungszentrum Juelich

d) Universitat Bonn, Helmholtz-Institut fur Strahlen- und Kernphysik (Theorie)

ი. ბიგი, გ. ჭილაძე, გ. დევიძე, ქ. ჰანჰარტი, ულ-გ. მაისნერი, ა. ლიპარტელიანი

დამუხტული ლეპტონების რადიაციული და B-მეზონების ორმაგი რადიაციული დაშლები უნივერსალური დამატებითი განზომილებების მოდელში

დასავმა

წინამდებარე ნაშრომში შესწავლილია დამუხტული ლეპტონების რადიაციული და B-მეზონების ორმაგი რადიაციული დაშლები უნივერსალური დამატებითი განზომილებების მოდელში ერთი დამატებითი განზომი-

ბიით. პაულ შერერის ინსტიტუტში (შვეიცარია) დაგეგმი-
ლია ორნახანი რეგით გაიზარდოს $\mu \to e\gamma$ პროცესის ალ-
ბათობის ქვედა ზღვარის სიზუსტე. ამასთან დაკავშირებით
თეორეტიკოსთა გამოთვლითობა $\mu \to e\gamma$ პროცესის ალბათობის
უნივერსალური დამატებითი განშრიალებებს მოდელში.
ჩვენმა გამოთვლებმა აჩვენა, რომ პაულ შერერის
ინსტიტუტში დაგეგმილ ექსპერიმენტებში უახლოეს მო-
მავალში შეუძლებელია უნივერსალური დამატებითი გან-
შრიალების კვალის დანახვა. რაც შეეხება ნეირალური B-
მეზონების ორნახა რადიაციულ დაშლებში, აქ უფრო
ოპტიმისტური შეგიძლიათ განაცხადება სტანდარტული
მოდელიში მიღებული შედეგებიან შედარებით რამდენიმე (3-
6) პროცენტია, რაც მოსალოდნელია მნიშვნელოვანია გა-
ზარდოს კვანტური ქრომოდინამიკურ შესწორებების გათვა-
ლისწინებით. უკანასკნელ შემთხვევაში შორს ალარია ის
დრო, როცა ექსპერიმენტ შესაძლებელი იქნება იქნება
უნივერსალურ დამატებითი განშრიალების გამოვლენა B-
მეზონების ორნახა რადიაციულ დაშლებში. კერძოდ,
როგორც ხომ, შეცა (BABAR, BELLE) ასევა მომავლის დაგეგ-
მილ ექსპერიმენტებში (LHC-B, Super B).

79

NEW MODELS OF SEMICONDUCTOR MATERIALS AND HETEROSTRUCTURES FOR IR LASERS AND PHOTODETECTORS

O. Davarashvili, L. Akhvlediani, M. Enukashvili, N. Kekelidze

ABSTRACT. It was stated by us that in the connection with the diffusional mismatch in semiconductor heterostructures IV-VI the pressure exceeding the limit of elasticity can originate. For lasers it leads to the increase of threshold currents almost by a range and to the decrease of operating temperature. When the critical deformation resource is used up, the widening of elastic deformation diapason is used on account of elasticity modulus modification by doping with impurities, decreasing the crystal constant of solid solution. Accordingly it causes a significant weakening of mismatch effect.

Widening of elastic deformation diapason also allows to create the conditions in epitaxial layers for displacing impurity level into the depth of the forbidden gap. If at the same time the impurity is capable of stabilizing the Fermi level then for the given impurity and certain composition of solid solutions the transformation metal-dielectric is carried out.

The work presents formulation of conditions for creation the dielectric state in given IV-VI semiconductors, which are necessary for rising sensitivity of IR photodetectors.

Lately considerable breakthrough has been traced in working out IR tunable lasers and photodetectors on the basis of IV-VI semiconductors. This is connected firstly with creation of new heterostructures and homogenous heavily doping crystals.

If the width of forbidden gap and effective mass of current carriers in different semiconductors are basically determined through their chemical composition (chemical formula), then most characteristics: type of conductivity, mobility of carriers, lifetime, coefficients of absorption and heat conduction, etc., significantly depend on doping impurities. According to totality of these parameters for different tasks

the most effective materials are selected. Particularly, for semiconductor lasers and photodetectors optimization of their characteristics: threshold current (operating temperature), capacity of radiation, sensitivity, etc., are carried out in consideration with influence of doping on electrical, optical and thermal characteristics of materials. Although our latest research [1] showed that new important resource in perfecting their characteristics represented mechanical elastic properties (elasticity modulus, limit elastic deformation), modified at doping by certain impurities.

In the present statement we consider the situations, when at widening diapason of elastic deformation in semiconductor lasers threshold current decreases, and resistivity and consequently sensitivity rises in photodetectors.

It is well-known that due to decrease of active volume and limitation effects a considerable decrease of threshold current is achieved in lasers on the basis of heterostructures. In most cases for widening spectral diapason multicomponent solid solutions are used as active lasers. Due to experiments and calculations in the process of heterostructure creation an obvious interdiffusion of solid solution components takes place [1]. Consequently even in structures, assumed as isoperiodic, in emitters and active ranges of lasers a mismatched area forms. In most cases they are inevitable, even when changing the profile of composition in the heterostructure. The strain corresponding to mismatch exceeds limit of elasticity- their relaxation causes mismatch dislocation from the sticking centre [1,2]. Because of the increase of nonradiative recombination the threshold current rises considering:

$$I_{th} \sim \left(\frac{\tau_{\text{эф}}}{\tau} \right)^{-1} = \frac{d + 2S\tau}{d}, \tag{1}$$

where τ is the carrier's lifetime considering the centres of recombination under mismatch; τ is lifetime in active area; d is the thickness of active range; S is the velocity of surface recombination (in the given case distributed in certain thickness in the active range of lasers). In its turn:

$$S = \sigma \cdot \upsilon \cdot N,\qquad(2)$$

here $\sigma = a^2$ is the square of recombination; υ is thermal velocity of current carriers; a is a crystal parameter constant; N- density of centres of recombination, equaling to:

$$N = \frac{1}{a^2} \cdot \frac{\Delta a}{a}.\qquad(3)$$

Assuming that at weak mismatch $\frac{\Delta a}{a}$ equals to its maximum. Let consider as a sample heterostructures in IV-VI semiconductors PbSeTe-PbSnSeTe. The mismatch $\frac{\Delta a}{a}$ in the active range at epitaxial temperature corresponds to $(1 \div 3) \cdot 10^{-3}$. On the other hand out of measuring the lifetime in the active range of heterostructures and amplitudes of dependence of internal friction more than half of the whole amount of defects are revealed at deformation $(1 \div 2) \cdot 10^{-3}$. Therefore, considering $\upsilon = 3 \cdot 10^7$ cm/s, $\tau = 5 \cdot 10^{-9} \div 10^{-8}$ s, $d = 0.4$ μm because of diffusional mismatch the measured threshold current I_{th} increases by an order and more.

It is worth mentioning that the limit stress at research internal friction are determined by critical amplitudes of oscillation (when the derivative of the energy loss from the amplitude of oscillation considerably changes) with weak temperature dependence, i.e. with strong centers of sticking the dislocation. Although, for the initial crystals and layers with different density of dislocation plastic deformation generates in comparatively small or big amount of local volumes of different values. In epitaxial layers at large density of dislocation the limit of elasticity occurs at small mismatch. But even in this case the influence on this threshold current is significant. The calculations show that if mismatch represents the half of limit, then the threshold current increases $5 \div 6$ times.

When the resource for limit strain deformation in laser structures are excluded, then ultimate stress $\sigma_M = \dfrac{E}{1-\nu} \cdot \dfrac{\Delta a}{a}$ (where ν is

Pausson coefficient) can be increased on behalf of the rise of elasticity modulus E (for photodetectors also due to increase of critical elastic deformation ε_{Cr}). The research [3] shows that elasticity modulus in IV-VI semiconductors rises 2.5-3 times, and the critical elastic deformation 3.5-4 times at doping by Cr, Ca Mn impurities on the level ≤ 0.01. All these impurities reduce the crystal constant even in the condition of its pressing the barrier for generation and motion of dislocation. Though, the most neutral in relation to radiative transition in IV-VI semiconductors is impurity of Mn.

The doping effect, for example, with chromium impurity, can be expressed by letting the coefficient $\frac{r_{Cr}}{r_{Pb}} C_{Cr}$ (where $r_{Cr} = 1.1$ Å, $r_{Pb} = 1.5$ Å radii of Cr and Pb atoms in the lattice of solid solution PbSnTe, $C_{Cr} \leq 0.01$ – concentration of chromium impurity) in the expression of dislocation tightness (3). Clearly enough, this effective mismatch reduces by 2-3 orders and the threshold current will significantly be decreased, and the operating temperatures of lasers will rise.

The evaluations given above relate to double heterostructure lasers. In case when the width of mismatch area coincides with the thickness of active layer of the laser, then formide lead to displacement of the band edges. Considering isotopic and mobile deformational potentials displacement of the band edges at $\varepsilon \approx 2 \cdot 10^{-3}$ represents ≈ 40 meV. At the same time the degeneracy of four ellipsoids of band structure for their different orientation is relative to the direction of deformation that causes decrease of density of state, and consequently to the threshold current. In this way diffusional mismatch can be used as a positive factor in creation of strained layers in this case.

One of the abovementioned impurities – chromium, along with widening the diapason of elastic deformation, has the feature of stabilization of Ferm level. In the condition of stabilization of Fermi level at the rise of concentration of the given impurity or others the Fermi level does not change its position. When some impurity is high in concentration $(10^{19} \div 10^{20} \text{cm}^3)$ nonstoichiometric and other electrically active defects can take multivalentive states, including donor and acceptor, certain relation of occupied states among them

takes place and the state of Fermi level changes only in accordance with composition of solid solutions.

In solid solutions PbSnSe(Te) with the rising composition of tin the stabilized Fermi level displaces from the edge of the conductivity band to valence band, so that amount of vacancies rises in the sublattice of metal-equilibrium displaces on the side of acceptor states. Although the chromium level in PbTe is placed above the edge of conductivity band (~100 meV) the speed of its displacement with the composition (8 meV per 1%SnTe) exceeds almost two times the speed of reducing the width of the forbidden gap (4.8 meV per 1%SnTe) and therefore for some compositions of solid solutions it falls below the middle of the forbidden gap, transferring to acceptor states. If stabilized Fermi level of chromium for some compositions coincides with the middle and is remote from the edges of bands at considerable energy – $(7 \div 9)$ kT, then resistivity of the semiconductor significantly rises and it becomes possible to realize effective photodetector at maximum temperature.

Behaviour of the chromium level in PbSnTe is a matter of interest even at hydrostatic pressure the level is weakly displaced relatively in the middle of the forbidden gap. Obviously in some compositions of PbSnTe when the stabilized level of chromium lies in the forbidden gap, at pressing with negative coefficient of change of the forbidden gap with the transfer of dielectric-metal takes place with pressure. If in any way we achieve the stretching of semiconductor the reverse effect will be observed. According to the model of the dielectric state in the indicated semiconductor, using the mentioned methods at doping by impurities, the widening of the forbidden gap and penetrating in the depth of forbidden gap (or the cut) of donor or acceptor level can be assumed. The calculations show that for leaving of the forbidden gap edge with the energy $7 \div 9$ kT by the Fermi level, the widening of the bands in the indicated semiconductors should be ~ 100meV (for compositions corresponding to $\lambda \leq 8$ μm). In the range of elastic deformation $8 \cdot 10^{-3}$, achieved at doping by chromium, the difference among the electron potentials and the holes should be 10 eV. It occurred that abovementioned options should be realized at stretching the semiconductor through the growth of thin strained layer, for example, PbSnTe on the substrate BaSeTe with crystal constant. For the concrete composition PbSeTe:Cr with the content of SnTe = 0.3 and Cr = 0.5 % at increase on the substrate BaSeTe with content of

BaTe-0.15, the mismatch constitutes $5 \cdot 10^{-3}$ and the suitable pressure – 8 kbar. The width of the forbidden gap increases at 60 meV and reaches 140 meV ($\lambda = 9 \mu m$) at 100K, and the chromium level leaves the peak of the valence band at 60 meV. Relation of the specific resistance of semiconductor in strained and normal states according to calculation makes 4÷5 ranges. For covering the area of spectrum up to 20 µm by photodetectors the composition of solid impurities will be separately doped by gallium and vanadium.

Thus, the negative effect of diffusional mismatch in laser structures can be surrounded by doping with active impurity layers, decreasing the crystal lattice parameters. The creation of dielectric states in narrow-band IV-VI semiconductors seems possible only in case of fulfilment of these three options:

a. Formation of pressure for interchanging the level of impurity in the forbidden gap with leaving the edges of bands at energy 7-9 kT.

b. Fulfilment of appropriation of this pressure for the diapason of elastic deformation of the observed composition of solid solutions.

c. Selection of substrate with the same crystallographic structure and the composition for the necessary mismatch.

In conclusion, it is worth mentioning that simultaneous stabilization of Fermi level and widening the diapason of elastic deformation at doping the IV-VI semiconductors by certain impurities transform the initially defective, nonstoichiometric material into perfect, homogeneous with wide possibilities for managing energetic spectrum the current carriers. This condition can play a decisive role in the further usage of IV-VI semiconductors in IR optoelectronics.

REFERENCES

1. O. Davarashvili, M. Enukashvili, N. Kekelidze,
   M. Metskhvarishvili. Georgian Engineering News, 2, 2002, 7.

2. O. Davarashvili, G. Darsavelidze, M. Enukashvili,
   N. Kekelidze, T. Mamedov, N. Akhmedadze. Research of

Internal Friction in IV-VI Semiconductors, International
Conference Proceedings "Fizika-2005", Baku, 2005.
3. O. Davarashvili, M. Enukashvili, N. Kekelidze, R. Mamedov,
V. Zlomanov. Influence of Impurities on the Mechanical
Properties of IV-VI Semiconductors. Thesis of the XI
International Conference on Condensed Matter Physics.
Ankara, 2004, 19.

Tbilisi State University

ო. დავარაშვილი, ლ. ახელედიანი, მ. ენუქაშვილი,
ნ. კეკელიძე

ნახევარგამტარული მასალებისა და პეტეროსტრუქტურების
ახალი მოდელები ინფრაწითელი ლაზერების და
ფოტომიმღებებისათვის

დასკვნა

დადგინდა, რომ დიოდურიო შემოანხმობის გამო
ნახევარგამტარული IV-VI პეტეროსტრუქტურებში შეიძლება
აღიძრას დაძაბულობის, რომელთაც აქარხები დრეკადობის
ზღვარს. ლაზერებისათვის ეს გამოიწვევს ზღუბლოური
დენების გაზრდას თითქმის ერთი რიგით და სამუშაო
ტემპერატურების შემცირებას. წარმოდგენილ შრომაში
შემოთავაზებული იყოდგა დეფორმაციის დაპაპზრობის
მინიშუმების გაზრდა დრეკადობის მოდულის მოდიფი-
კაციის შესრებით, როცა ზღუბრული დეფორმაციის რე-
სურსები მთლიანად ამოისუბება. დრეკადობის მოდულის
მოდიფიკაცია ღა ხისხისრამის კრისტალური მესერის
პარა-მეტრის შემცირდიდობ მინარჯევების ღდეფირებით. შესაბა-
ნისად არსებითად სუსტდება დრეკადობის მოდული. შესაძ-
დრეკადი დეფირმაცია გაფართოება შესაძლებელ
ხდება, არერთის, გაპტეისტაცურ ფენებში მინარჯული
ღონეების გადანაცელებით არრალელურ ზონის სიღრმიში

ამავე დროს, თუ მინარევს ფერმის დონის სტაბილიზაციის უნარი აქვს, მაშინ მოცემული მინარევისათვის განსხვავებულდება შერეული-დიელექტრიკა გაადსლება განსხვავებული შემადგენლობისა მყარ ხსნარში.

შრომაში ფორმულირებულია პირობები ვიზრობსიიან IV-VI ნახევარგამტარში დიელექტრიკული მდგომარეობის შესაქმნელად, რომელიც აცივებებისას იწ ფოტომძგნებების მერხნებიარულში ასამღიღზდელდება.

SUPERCHARGE OPERATOR OF HIDDEN SYMMETRY IN THE DIRAC EQUATION

T. Khachidze, A. Khelashvili

ABSTRACT. As it is known, the so-called Dirac K-operator commutes with the Dirac Hamiltonian for arbitrary central potential $V(r)$. Therefore the spectrum is degenerate with respect to two signs of its eigenvalues. This degeneracy may be described by some operator, which anticommutes with K. If this operator commutes with the Dirac Hamiltonian at the same time, then it establishes new symmetry, which is Witten's supersymmetry. We construct the general anticommutator with K-operator, which under the requirement of this symmetry unambiguously select the Coulomb potential. In this particular case our operator coincides with that, introduced by Johnson and Lippmann many years ago.

Supersymmetry (SUSY) of the hydrogen atom is rather old and well-studied problem. We have in mind the usual cases: SUSY in non-relativistic quantum mechanics and inclusion of spin degrees of freedom by Pauli method as well. In the last case the projection of well-known Laplace-Runge-Lenz vector onto the electron spin direction plays the role of supercharge [1].

Relatively less is known about the Dirac electron, although the so-called radial SUSY was demonstrated a long-time ago [2]. As for 3-dimensional case, it was shown [3-6], that the supercharge operator is the one, introduced by Johnson and Lippmann in 1950 in the form of a brief abstract [7]. As regards to the more detailed derivation, to the best our knowledge, it is not published in scientific literature. Moreover as far as commutativity of the Johnson-Lippmann operator with the Dirac Hamiltonian is concerned, it is usually mentioned that it can be proved by "rather tedious calculations" [5].

The main aim of our paper is a derivation of the Johnson-Lippmann operator in a simple and transparent manner and simultaneous demonstration of its commutativity with the Dirac Hamiltonian.

Below we show that among all central potentials the Coulomb potential is a distinguished one. The additional symmetry takes place only for this potential. Then we show that the operator responsible for that symmetry reduces to the Johnson-Lippmann one in case of Coulomb potential.

So, let us consider the Dirac Hamiltonian for arbitrary central potential, $V(r)$:

$$H = \vec{\alpha} \cdot \vec{p} + \beta m + V(r). \qquad (1)$$

In this form $V(r)$ is a fourth component of a Lorentz 4-vector. We mention this fact here because the pure Lorentz-scalar potential is also often considered [8].

Let us introduce the so-called Dirac operator [9]

$$K = \beta \left(\vec{\Sigma} \cdot \vec{l} + 1 \right), \qquad (2)$$

where $\vec{l}$ is the angular momentum vector, $\vec{\alpha}$ and β are the usual Dirac matrices and $\vec{\Sigma}$ is the electron spin matrix

$$\vec{\Sigma} = \begin{pmatrix} \vec{\sigma} & 0 \\ 0 & \vec{\sigma} \end{pmatrix}. \qquad (3)$$

It is easy to show that

$$[K, H] = 0 \qquad (4)$$

for arbitrary central potential, $V(r)$.

Therefore the spectrum of Dirac equation is degenerate with respect to eigenvalues κ of the K-operator. As a rule, this is a degeneracy with regard to the signs of κ, $(\pm \kappa)$ [10].

We can find an operator A, which could connect these two signs. Naturally, such an operator should anticommute with K,

$$\{A, K\} = AK + KA = 0. \qquad (5)$$

89

If at the same time this operator commutes with Hamiltonian H, it will generate the symmetry of the Dirac equation.

Therefore, we are looking for an operator A with the following properties

$$[A,H]=0, \quad \{K,A\}=0. \qquad (6)$$

After that we will be able to construct supercharges as follows [3-6]

$$Q_1 = A, \qquad Q_2 = i\frac{AK}{|\kappa|}. \qquad (7)$$

Then it is obvious that

$$\{Q_1,Q_2\}=0 \qquad (8)$$

and we can construct Witten's superalgebra, where $Q_1^2 = Q_2^2 = h$ is a Witten's Hamiltonian.

Now our goal is a construction of the A operator. For this purpose at first we generalize one theorem [1,11], known from Pauli equation to the case of Dirac equation. For the Dirac case this theorem may be formulated as follows:

Theorem:

Suppose $\vec{V}$ be a vector with respect to the angular momentum $\vec{l}$, i.e.

$$[l_i, V_j] = i\varepsilon_{ijk}V_k$$

or, equivalently, in the vector product form one has

$$\vec{l} \times \vec{V} + \vec{V} \times \vec{l} = 2i\vec{V}.$$

Suppose also that this vector is perpendicular to $\vec{l}$

$$\left(\vec{l} \cdot \vec{V}\right) = \left(\vec{V} \cdot \vec{l}\right) = 0.$$

Then K anticommutes with operator $\left(\vec{\Sigma} \cdot \vec{V}\right)$, which is scalar with respect to the total $\vec{J}$ momentum, i.e. it commutes with $\vec{J} = \vec{l} + \frac{1}{2}\vec{\Sigma}$.

The proof of this theorem is almost trivial - it is sufficient to consider the product $\left(\vec{\Sigma} \cdot \vec{l}\right)\left(\vec{\Sigma} \cdot \vec{V}\right)$ in this and in reversed orders and make use of definition of K. Then it follows that

$$\left\{K, \vec{\Sigma} \cdot \vec{V}\right\} = K\left(\vec{\Sigma} \cdot \vec{V}\right) + \left(\vec{\Sigma} \cdot \vec{V}\right)K = 0. \qquad (9)$$

It is evident that the class of operators anticommuting with K (so-called, K-odd operators) is not restricted by these operators only. Any operator of the form $\hat{O}\left(\vec{\Sigma} \cdot \vec{V}\right)$, where $\hat{O}$ commutes with K, but otherwise arbitrary, also is a K-odd.

Let us remark for the further application, that the following useful relation holds in the framework of conditions of the above theorem.

$$K\left(\vec{\Sigma} \cdot \vec{V}\right) = -i\beta\left(\vec{\Sigma} \cdot \frac{1}{2}\left[\vec{V} \times \vec{l} - \vec{l} \times \vec{V}\right]\right). \qquad (10)$$

Now one can proceed to the second stage of our problem - we wish to construct the K-odd operator A, that commutes with H. It is clear that there remains large freedom according to the above mentioned remark about $\hat{O}$ -operator - one can take $\hat{O}$ into account or ignore it.

We have the following physically interesting vectors at hand which obey the requirements of our theorem. They are:

$\hat{r}$ - unit radius vector and $\vec{p}$ - linear momentum vector.

Both of them are perpendicular to $\vec{l}$. Constraints of this theorem are also satisfied by Laplace-Runge-Lenz vector $\vec{A} = \hat{P} - \frac{i}{2ma}$

$\times \left[\vec{p} \times \vec{l} - \vec{l} \times \vec{p} \right]$, but this vector is associated to the Coulomb potential. Hence, we abstain from its consideration for now. We can remark that $\vec{\Sigma} \cdot \vec{A}$ is not an independent structure. It is expressible by two other structures. e.g. $\vec{\Sigma} \cdot \vec{A} = \vec{\Sigma} \cdot \vec{r} + \dfrac{i}{ma} \beta K \left(\vec{\Sigma} \cdot \vec{p} \right)$. Therefore, we choose the following K -odd terms:

$$\vec{\Sigma} \cdot \vec{r} \qquad \text{and} \qquad K \left(\vec{\Sigma} \cdot \vec{p} \right). \qquad . \quad (11)$$

As it turns out inclusion of K into the second term in (11) is necessary for obtaining our final result.

Let us remark that both operators in (11) are diagonal matrices, while the Hamiltonian (1) is non-diagonal. Therefore, in commuting of (11) with H non-diagonal terms appear as well. For instance,

$$\left[\vec{\Sigma} \cdot \vec{r}, H \right] = \dfrac{2i}{r} \beta K \gamma^5. \qquad (12)$$

Therefore, we probe the following operator:

$$A = x_1 \left(\vec{\Sigma} \cdot \vec{r} \right) + i x_2 K \left(\vec{\Sigma} \cdot \vec{p} \right) + i x_3 K \gamma^5 f(r). \qquad (13)$$

Here the coefficients $x_i \, (i = 1,2,3)$ are chosen in such a way, that A is Hermitian operator for arbitrary real numbers x_i and $f(r)$ is an arbitrary scalar function to be determined later.

The commutator of A with H is calculated straightforwardly and the result is

$$[A,H] = x_1 \dfrac{i}{r} \beta K \gamma^5 + x_2 K \left(\vec{\Sigma} \cdot \vec{r} \right) V'(r) -$$
$$- x_3 K \left(\vec{\Sigma} \cdot \vec{p} \right) f'(r) - i x_3 2m \beta K \gamma^5 f(r).$$

Equating the above expression to zero, i.e. requiring commutativity of our operator with the Dirac Hamiltonian, we find

$$K\left(\vec{\Sigma}\cdot\vec{r}\right)\left[x_2 V'(r) - x_3 f'(r)\right] + 2i\beta K\gamma^5\left[\frac{x_1}{r} - mx_3 f(r)\right] = 0 . \quad (14)$$

Here terms are grouped in a way that we have a diagonal matrix in the first row, while the anti-diagonal matrix is in the second row. Therefore, the two equations follow:

$$x_2 V'(r) = x_3 f'(r), \quad (15)$$

$$x_3 m f(r) = \frac{x_1}{r} . \quad (16)$$

Integrating Eq.(15) with the requirement, that functions $f(r)$ and $V(r)$ tend to zero when $r \to \infty$, yields

$$x_3 V(r) = x_3 f(r), \quad (17)$$

while the equation (16) gives

$$f(r) = \frac{x_1}{x_2} \frac{1}{mr} . \quad (18)$$

Substituting Eq.(18) into Eq.(17) results in the following potential

$$V(r) = \frac{x_1}{x_2} \frac{1}{r} . \quad (19)$$

Hence, in the very general framework we have shown that the only central potential for which the Dirac Hamiltonian would have an additional symmetry (in the above mentioned sense) is a Coulomb potential.

Meanwhile, the relative signs of coefficients x_1 and x_2 may be arbitrary. Therefore we have a symmetry both for attraction and repulsion.

If we take the Coulomb potential in the usual form

$$V_c(r) = -\frac{a}{r},$$ (20)

where $a = Ze^2 = Z\alpha$, it follows

$$x_2 = -\frac{1}{ma} x_1.$$ (21)

In this case our symmetry operator (13) becomes

$$A = x_1 \left\{ \left(\vec{\Sigma} \cdot \hat{r} \right) - \frac{i}{ma} K \left(\vec{\Sigma} \cdot \vec{p} \right) + \frac{i}{mr} K \gamma^5 \right\}.$$ (22)

Number x_1, as an unessential common factor may be omitted. Moreover, if we make transition to the usual Dirac $\vec{\alpha}$ matrices according to the relation $\vec{\Sigma} = \gamma^5 \vec{\alpha}$, then operator A can be reduced to the form

$$A = \gamma^5 \left\{ \vec{\alpha} \cdot \hat{r} - \frac{i}{ma} K \gamma^5 (H - \beta m) \right\},$$ (23)

which coincides precisely with the Johnson-Lippmann operator [7].

We mention here that if the potential in the Dirac Hamiltonian was a Lorentz-scalar (which means the change $V \rightarrow \beta V$) then, while K still commutes with H, operator A does not commute anymore with K even for Coulomb potential.

Thus, we are convinced that in this problem of supersymmetry, the Coulomb potential (as a fourth component of 4-vector, i.e. minimal

gauge invariant switching) takes exceptional role - the supercharges and Witten algebra can be constructed *only* for this potential.

What real physical picture is standing behind this?

Remark that taking into account the Eq.(10) one can recast $\vec{V} = \vec{p}$, one can recast our operator for the Coulomb potential in the following form

$$A = \vec{\Sigma} \cdot \left(\vec{\hat{F}} - \frac{i}{2ma} \beta \left[\vec{p} \times \vec{l} - \vec{l} \times \vec{p} \right] \right) + \frac{i}{mr} K \gamma^5. \tag{24}$$

One can see that in the non-relativistic limit, i.e. $\beta \to 1$ and $\gamma^5 \to 0$, our operator reduces to

$$A_{NR} = \vec{\sigma} \cdot \left(\vec{\hat{F}} - \frac{i}{2ma} \left[\vec{p} \times \vec{l} - \vec{l} \times \vec{p} \right] \right). \tag{25}$$

Note the Laplace-Runge-Lenz vector in the parenthesis of Eq.(25). Therefore, relativistic supercharge reduces to the projection of the Laplace-Runge-Lenz vector on the electron spin direction. Precisely this operator, Eq.(25) was used in the case of Pauli electron [1].

Therefore, we see that there is a deep relation between supersymmetry of the Dirac Hamiltonian and the symmetry related to the Laplace-Runge-Lenz vector, which appeared already in classical mechanics and provides the closeness of celestial orbits.

We can conclude that the hidden symmetry associated to the Laplace-Runge-Lenz vector governs very wide range of physical phenomena from planetary motion to fine and hyperfine structure of atomic spectra. As for the Lamb shift, which is pure quantum field theory effect, its Hamiltonian, produced by radiative corrections of a photon propagator and photon-electron vertex function, does not commute with A operator and therefore spoils the above mentioned symmetry (supersymmetry). In other words, symmetry of the A operator controls the absence of the Lamb shift in the Dirac theory.

In conclusion, one must also remember that the form of obtained symmetry operator is not unique. One can always replace $A \to \hat{O}A$.

where $\left[\hat{O}, H\right] = 0$ and $\left[\hat{O}, K\right] = 0$. One can take, for example,

$\hat{O} = f(K)$ - arbitrary regular matrix function of K. Moreover, SUSY in specific and mostly exotic models of Dirac equation (such as $2 + 1$ dimensions [12], non-minimal or anomalous magnetic moment coupling [13], squared equation [14,15], etc.) are not excluded by our above consideration.

REFERENCES

1. R.G.Tangerman, J.A.Tjon. Phys. Rev. **A48**, 1998, 1089.
2. C.V.Sukumar. J.Phys.A:Math.Gen. 18, 1985, L697.
3. J.P.Dahl, T.Jorgensen. Int.J.Quantum Chemistry. **53**, 1995, 161.
4. A.A. Stahlhofen. Helv.Phys.Acta. **70**, 1997, 372.
5. H.Katsura, H.Aoki. ArXiv: **quant-ph**/0410174 (2004).
6. T.T.Khachidze, A.A.Khelashvili. Mod.Phys. Lett. **A20**, 2005, 2277.
7. M.H.Johnson, B.A.Lippmann. Phys.Rev. **78**, 1950, 329(A).
8. C.L.Critchfield. J. Math. Phys. **17**, 1976, 261.
9. P.A. Dirac. The Principles of Quantum Mechanics, 4th ed. Oxford Univ.Press, London, 1958. Chap.11.
10. J.J.Sakurai. Advanced Quantum Mechanics. Addison-Wesley, MA, 1967, Chap.3.
11. L.Biederharn, L.Louk, in Encyclopedia of Mathematics and Its Application. Addison-Wesley Reading, MA, 1981.
12. H.Ui. Progr.Theor.Phys. **72**, 1984, 192.
13. V.V.Semenov. J.Phys. A: Math. Gen. **23**, 1990, L721.
14. F.De Jonghe et al. Phys. Lett. **B359**, 1995, 114.
15. P.A.Horvathy et al. arXiv: hep-th/0006118 (2000).

თ. ხახიძე, ა. ხელაშვილი

სუპერსიმეტრიული ოპერატორ დირაკის განტოლების ფარული სიმეტრიისათვის

დასკვნა

ცნობილია, რომ ე.წ. დირაკის K ოპერატორი კომუტირებს დირაკის ჰამილტონიანთან ჩებისმიერი ცენტრალურად სიმეტრიული პოტენციალისათვის $U(r)$. ამიტომ სპექტრი გადაგვარებულია მისი საკუთარი მნიშვნელობების ორი ნიშნის მიმართ. ეს გადაგვარება შეიძლება აღიწეროს რიგი ოპერატორით, რომლებიც ანტიკომუტირებს K ოპერატორთან. თუკი ამ ოპერატორის ამავე დროს იკომუტირებს დირაკის ჰამილტონიანთან, მაშინ გვექნება სიმეტრია, რომელიც აღიწერება ე.წ. ცრუდის სუპერსელექტორით.

ჩვენ ავიღეთ უზოგადესი K-სთან ანტიკომუტატორის ოპერატორი, რომელმაც ზემოაღნიშნულ სიმეტრიის მოთხოვნით ცალსახად გამოიყო კულ. ლორენც პოტენციალი. მხოლოდ კულონური პოტენციალისათვის აქ დირაკის განტოლებას $N = 2$ სუპერსიმეტრია. ამ კერძო შემთხვევაში ჩვენ მიერ მიღებული სიმეტრიის ოპერატორ დასმისა სამიცნიერო ლიტერატურაში ცნობილ ოპერატორს, რომელიც შემოიყვანა ყად ლიაპისონს და ჯონსონის მიერ დიდი ხნის წინ მოკლე ანოტაციის სახით.

COMPARATIVE ANALYSIS OF THE AVERAGE MULTIPLICITIES OF CHARGED SECONDARY HADRONS, PRODUCED IN ELECTRON-POSITRON, PROTON-PROTON (ANTIPROTON) AND PROTON-NUCLEUS COLLISIONS

L. Akhobadze, V. Garsevanishvili, T. Jalagania, Yu. Tevzadze, G. Vanishvili

ABSTRACT. The $<n_{ch}(s)> \cong <n(s)>$ dependence on energy of the average multiplicity of charged secondary hadrons produced in electron-positron, proton-proton (antiproton) and proton-nucleus collisions is analysed on the basis of following models: Statistical model, Field-Feynman model, Cluster model and Lund model and parton-hadrons local duality model or Perturbative quantum chromodynamics.

I. INTRODUCTION

Characteristics of secondaries in hh-hadron-hadron, hA, -hadron-nucleus and e^+e^--electron-positron collisions are studied for many decades in cosmic rays and at the accelerators as well. For the analysis of experimental data up to 60-ies of the XX century (prequark epoch) different theoretical models have been developed (classical and quantum). These models described the main experimental regularities of soft processes – weak growth of the interaction cross section and multiplicity with increasing energy, restriction of the transverse momenta of secondaries, etc.

These models can be divided conventionally into two groups: statistical and multiperipheral. The first group starts from the notions of classical physics, taking into account some quantum effects – it is assumed initial hadrons form an exited, so called compound-system, which decays according to the laws of statistics [1,2].

The second group of models is based on quantum field theory. The production process is considered as a result of creation of many exited states (resonances, clusters). One of the representatives of this group

is a multiperipheral model, and its development is connected with the parton description of multiparticle processes. The existence of different approaches shows that at present we are far from the construction of the unique picture of soft processes. But the description of some significant regularities in terms of these models allows (in some sense) to construct fragments of this picture. The successes of these models should be taken into account in the development of the quark-parton interaction picture.

The experimental observation of quarks and gluons stimulated the creation of new model for hadronic interactions-quark model have been developed intensively, which have been applied for the explanation of some physical regularities [3,4,5]. In these studies two different areas of the application of quark-parton models are distinguished: a) the soft collision region-small momentum transfer (less than 1GeV/c, large distances, ~ 1F), in which the model is of the phenomenological nature, b) hard collisions region – large momentum transfer (>1GeV/c) and small distances (less than 0.1 F), where the perturbative QCD can be applied. QCD successfully describes the interaction of colored partons (quarks and gluons) at small distances due to the remarkable property of this theory (asymptotic freedom). At large distances for the description the hadronization of quarks phenomenological models are used. On the other hand, it is clear that physics of hard and soft processes is unique and it is necessary to consider them together for the construction of the strong interaction theory. It should be noted that in all quark parton models the main problem is the quark (parton, cluster) hadronization.

In the present paper the $<n_{ch}(s)>\equiv <n(s)>$ dependence on energy of the average multiplicity of charged secondary hadrons produced in electron-positron, proton-proton (antiproton) and proton-nucleus collisions is analysed on the basis of following models: SM(1) - Statistical model, FFM(2) - Field-Feynman model, CLM and LM(3) - Cluster model and Lund model and parton-hadrons local duality model or PQCD(4) - Perturbative quantum chromo dynamics (4) [1,2].

The above mentioned models give for the $<n_{ch}(s)>\equiv <n(s)>$ dependence following relations:

$$\langle n_{ch}(s)\rangle \geq \langle n(s)\rangle \longrightarrow \begin{cases} a\,s^{\beta} & SM, & (1) \\ a+b\ln s & FFM, & (2) \\ a+b\ln s+c(\ln^2 s) & CLM(LM), & (3) \\ a+b\exp(c_1\sqrt{\ln s}) & PQCD, & (4) \end{cases}$$

where s is the square of the total energy in the c. m. s., a, β, b, c are free parameters, which are extracted from the experiment; parameter c_i is calculated according to the formula [1;2]:

$$c_1 = \left(\frac{72}{33-2Nq}\right)^{1/2}, \qquad (5)$$

where N_q is the number of quark flavours, c_i can be considered as a free parameter as well.

The problem of quark (parton, cluster) hadronization is treated in different ways in different models. The model description of quarks is given either by PQCD or by the phenomenological approach.

In CLM(3) – cluster models hadronization is described without introduction of fragmentation function and restriction of parton transverse momenta. The first stage of the hard process-production of parton shower, is considered in the framework of the QCD. Due to the long distance colour forces the quarks and antiquarks form colorless clusters and after words hadronization of clusters is realized.

Hadronization of quarks in the FFM(2) in similar to the production of hadrons in the parton model. Hadrons are produced through the consequentive and independent decays:

$$q_a \to q_b + M, \qquad (6)$$

where initial quark (q_a) is fragmented into the meson M and the new quark (q_b), then q_b decays again according to the scheme (6). In the LM(3)-Lund model, the evolution of quark-antiquark systems is

considered taking into account the character of colour forces between quarks.

In the LM(3) it is possible to take into account the conservation of energy and quantum numbers. In this sense LM(3) is more adequate, than the FFM(2).

In the PQCD the parameter c_i is given by the relation (5) and takes the values:

$$c_i = \begin{cases} 1.63 & N_q = 3 \\ 1.70 & N_q = 4 \\ 1.77 & N_q = 5 \end{cases} \tag{7}$$

2. ANALYSIS OF EXPERIMENTAL DATA

The $<n(s)>$ dependence on energy of the average multiplicity of charged secondary hadrons in e^+e^-, pp^* and pA_t-collisions is analysed on the basis of above mentioned models (See equations (1), (2), (3), (4)).

pTa interaction is analysed to study the role of the heavy target nucleus. The results of the analysis are compared to each other in the same energy intervals, if possible. The experimental data are taken from the current literature [1-10].

The SM(1) describes rather well the data for e^+e^- collisions, especially for high energy intervals ((14-130), (14-91), (10-130), (10 - 200) GeV) (see Tables 1 and 7).

The value of the parameter β is located in the narrow interval $(0.20 \pm 0.01 \div 0.28 \pm 0.01)$. In high energy intervals the parameter β is slightly decreased to the value 0.20 ± 0.01. The inclusion of low energy data (low average multiplicities) causes the increase of the parameter β to the value 0.28 ± 0.01 (see Table 9). So the role of neutral particles in $<n(s)>$ is increased with increasing energy. (We will return to this point later).

---

* In the following we use the notation pp for both pp and proton-antiproton-collisions.

The description of $<n(s)>$ dependence by the SM(1) for pp collisions is worse, than in e^+e^- collisions. However the qualitative picture is the same. Namely, in low energy intervals $(2 \leq \sqrt{s} \leq 22)$ GeV the tendency of increasing of β $(0.32 \pm 0.01$, Table 9) is observed. The inclusion of high energy data causes the decreasing of β to the value 0.22 ± 0.01 (Table 1. $(10 \leq \sqrt{s} \leq 200)$ GeV).

The fact, that the multiplicity in e^+e^- interactions is always more than in pp-collisions (of course at fixed energy) can be explained by the baryon number conservation and by leading particles, which take the significant part of the initial energy.

Table 1.

The values of the parameters a, b, β, c and c_j in the approximation of the $<n(s)>$ dependence by the expressions (1),(2), (3), (4)

e^+e^--collisions $(1.5 \leq \sqrt{s} \leq 200)$ GeV

Formula	a	$b(\beta)$	c	χ^2/N
SM(1)	2.56±0.07	0.23±0.01		75/48
FFM(2)	-1.77±0.14	2.39±0.03		540/48
CLM(LM)(3)	2.81±0.25	-0.07±0.11	0.23±0.02	18/48
PQCD(4)	1.24±0.19	0.37±0.04	1.31±0.03	30/48

e^+e^--collisions $(10 \leq \sqrt{s} \leq 200)$ GeV

SM(1)	3.31±0.29	0.20±0.01		10/31
FFM(2)	-11.11±0.67	3.55±0.09		36/31
PQCD(4)	-0.21±0.95	0.65±0.14	1.15±0.06	8/31

SM(1)	2.06±0.11	0.22±0.01		28/11
FFM(2)	-5.17±0.42	2.17±0.07		36/11
PQCD(4)	-1.15±0.87	0.64±0.19	1.07±0.08	19/11

The experimental fact of the significant difference of average multiplicity in e^+e^- and pp-collisions is reflected in the inequality of parameters a: $a_{e^+e^-} = 3.31 \pm 0.29$; $a_{pp(p\bar{p})} = 2.06 \pm 0.11$ (Table 1). The cluster model and the Lund function - CLM(LM) describes well data for pp and especially for e^+e^--collisions. Simplest quark-parton models predict the logarithmic dependence of $<n(s)>$, i.e. $<n(s)> \sim \ln s$. However, the analysis of data shows, that $<n(s)>$ increases faster than $\ln s$ and the term $\ln^2 s$ is decisive. For instance, in e^+e^--collisions in the intervals including low energy data (Tables 2, 3, 4, 6) the value of coefficient c (before $\ln^2 s$) is equal to 0.23 ±0.01. High energy data give for c the value 0.34 ±0.02 (Table 7).

In pp-collisions the value of the coefficient c is always less than in e^+e^-- collisions and equals to 0.14 ±0.01. On the other hand, it is known, that the average multiplicity of hadrons in the jet increased as $\ln^2 s$.

On can conclude, that in e^+e^--collisions the jet structure is more pronounced, than in pp- and in pA_t- proton-nucleus collisions. This is confirmed also from different points of view and experiments [1].

It is interesting to note, that in e^+e^--collisions the coefficients b and c have different signs ($b < 0$), but in pp-collisions they have the same sign.

Table 2.

The values of parameters a, b, β, c, c_i in the approximation of the $<n(s)>$ dependence by formulae (1), (2), (3), (4)

$(3 \le \sqrt{s} \le 200)$ GeV , e^+e^-

Formula	a	$b(\beta)$	$c(c_i)$	χ^2/N
SM(1)	2.60±0.08	0.23±0.01		69/45
FFM(2)	-3.85±0.18	2.69±0.04		250/45
CLM(LM)(3)	2.72±0.49	-0.04±0.19	0.23±0.01	17/45
PQCD(4)	0.28±0.24	0.54±0.05	1.21±0.03	21/45

$(3 \le \sqrt{s} \le 200)$ GeV , pp

SM(1)	1.52±0.02	0.27±0.01		174/22
FFM(2)	-1.20±0.06	1.48±0.02		270/22
CLM(LM)(3)	1.17±0.15	0.28±0.07	0.14±0.01	30/22
PQCD(4)	0.024±0.087	0.41±0.02	1.20±0.02	30/22

$(3 \le \sqrt{3} \le 30)$ GeV, e^+e^-

SM(1)	2.06±0.31	0.27±0.01		13/17
FFM(2)	-1.12±0.30	1.93±0.08		32/17
CLM(LM)(3)	3.10±0.80	-0.24±0.46	0.25±0.02	10/17
PQCD(4)	1.50±0.35	0.24±0.08	1.48±0.09	12/17

$(3 \le \sqrt{s} \le 30)$ GeV, pp

SM(1)	1.38±0.02	0.29±0.01		50/16
FFM(2)	-0.99±0.07	1.42±0.02		146/16
CLM(LM)(3)	1.18±0.15	0.27±0.02	0.14±0.01	17/16
PQCD(4)	0.22±0.08	0.33±0.02	1.28±0.02	18/16

104

Table 3.

The values of parameters a, b, β, c, c_i in the approximation of the $<n(s)>$ dependence by formulae (1), (2), (3), (4)

$(3 \le \sqrt{s} \le 130)$ GeV, e^+e^--collisions

Formula	a	$b(\beta)$	$c(c_i)$	χ^2/N_p
SM(1)	2.32±0.09	0.25±0.01		28/30
FFM(2)	-2.75±0.20	2.41±0.03		110/30
CLM(LM)(3)	2.91±0.62	-0.13±0.27	0.23±0.02	14/30
PQCD(4)	0.88±0.47	0.39±0.10	1.31±0.08	15/30

$(3 \le \sqrt{s} \le 130)$ GeV, pp

Formula	a	$b(\beta)$	$c(c_i)$	χ^2/N_p
SM(1)	1.48±0.01	0.27±0.01		143/21
FFM(2)	-1.13±0.06	1.46±0.02		190/21
CLM(LM)(3)	1.02±0.17	0.36±0.08	0.13±0.01	24/21
PQCD(4)	-0.19±0.09	0.46±0.03	1.16±0.02	28/21

In e^+e^--collisions (in high energy intervals, Table 7) together with the growth of the influence of $\ln^2 s$- term, the role in the $\ln s$-term also increases. The parameter b reaches the value ~ 2 (with minus sign). Thus, in e^+e^--collisions the growth of the influence of the $\ln^2 s$-term causes the growth of the influence of the logarithmic term, as well.

In pp-collisions the situation is opposite: weak growth of the influence of the $\ln^2 s$-term (small growth of the parameter c) causes the significant decrease of the logarithmic term (significant decrease of the coefficient b) (Table 5). And vice versa: some decreases of the value parameter c, causes the significant growth of the parameter b (Tables 2, 3).

The PQCD describes well the $<n(s)>$ dependence for e^+e^- collisions and for pp-collisions as well. However, values of the parameter c_i extracted from the approximation do not correspond to values obtained from the formula (7), for instance the maximal value of the parameter $c_i = 1.54 \pm 0.07$ (Table 6, e^+e^-, $(1.5 \leq \sqrt{s} \leq 30)$ GeV).

If proceed from table values (7) and do not consider c_i as a free parameter, the good description is obtained only for e^+e^- collisions, when $c_i = 1.77$ ($N_q = 5$), $(14 \leq \sqrt{s} \leq 200)$ GeV. (Table 8)

We studied also the $<n(s)>$ - dependence for pTa-collisions and results were compared with the results for e^+e^- and pp-collisions in the interval $(2 \leq \sqrt{s} \leq 22)$ GeV, (Table 9).

In e^+e^- and pp-collisions $<n(s)>$ dependence (according to SM (1)) increased equally fast ($\beta \approx 0.30$).

In pTa-collisions more rapid growth is observed ($\beta \approx 0.45$). In the beginning (up to $\sqrt{s} \leq 5$ GeV) a most rapid growth is observed and further the growth is significantly slower, β is approximately the same as in e^+e^- and pp - collisions (Fig.1).

Table 4.

Values of parameters a, b, β, c, c_i in the approximation of the $<n(s)>$ dependence by formulae (1), (2), (3), (4)

$(1.5 \leq \sqrt{s} \leq 91)$ GeV, e^+e^- -collisions

Formula	a	$b(\beta)$	$c(c_i)$	χ^2/N_p
SM(1)	2.28 ± 0.08	0.25 ± 0.01		$25/31$
FFM(2)	-0.73 ± 0.15	2.05 ± 0.03		$240/31$
CLM(LM)(3)	2.83 ± 0.28	-0.09 ± 0.14	0.23 ± 0.01	$13/31$
PQCD(4)	1.72 ± 0.22	0.25 ± 0.04	1.45 ± 0.05	$19/31$
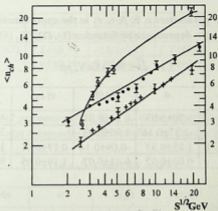
Fig.1. $< n(s) >$ dependence for $pp(+)$, e^+e^- (•) and pTa(○)-
collisions. Solid line – approximation by CLM(LM)
(formula (3))

$(1.5 \leq \sqrt{s} \leq 130)$ GeV, e^+e^-

SM(1)	2.31±0.07	0.25±0.01		28/33
FFM(2)	-0.70±0.15	2603±0.30		250/33
CLM(LM)(3)	2.89±0.27	-0.08±0.14	0.22±0.01	14/33
PQCD(4)	1.65±0.21	0.26±0.04	1.43±0.05	15/33

Table 5.

Values of parameters a, b, β, c, c_l in the approximation of the $<n(s)>$ dependence by formulae (1), (2), (3), (4)

$(3 \le \sqrt{s} \le 900)$ GeV, pp

Formula	a	$b(\beta)$	$c(c_l)$	χ^2/N_p
SM(1)	1.70±0.03	0.24±0.01		437/23
FFM(2)	-2.57±0.16	1.96±0.03		227/23
CLM(LM)(3)	1.85±0.33	-0.09±0.14	0.17±0.01	10/23
PQCD(4)	0.06±0.32	0.41±0.07	1.19±0.05	9/23

Table 6.

Values of parameters a, b, β, c, c_l in the approximation of the $<n(s)>$ dependence by formulae (1), (2), (3), (4)

$(3 \le \sqrt{s} \le 60)$ GeV, e^+e^-

Formula	a	$b(\beta)$	$c(c_l)$	χ^2/N
SM(1)	2.21±0.09	0.26±0.01		17/25
FFM(2)	-2.32±0.22	2.29±0.05		71/25
CLM(LM)(3)	2.91±0.64	-0.13±0.25	0.24±0.02	12/25
PQCD(4)	1.16±0.26	0.32±0.05	1.37±0.05	14/25

$(3 \le \sqrt{s} \le 60)$ GeV, pp

SM(1)	1.44±0.02	0.27±0.01		93/20
FFM(2)	1.09±0.06	1.45±0.02		141/20
CLM(LM)(3)	1.07±0.17	0.33±0.08	0.13±0.01	23/20
PQCD(4)	0.018±0.085	0.41±0.02	1.20±0.02	25/20

$$(1.5 \leq \sqrt{s} \leq 30)^* \text{ GeV, } e^+e^-$$

SM(1)	2.21±0.08	0.26±0.01		17/23
FFM(2)	-0.09±0.16	1.81±0.04		149/23
CLM(LM)(3)	2.84±0.30	-0.09±0.17	0.23±0.02	12/23
PQCD(4)	1.93±0.28	0.20±0.04	1.54±0.06	16/23

Table 7.

Values of parameters *a, b, β, c, c_I* in the approximation of the
< n(s) > dependence by formulae (1), (2), (3), (4)

$$(14 \leq \sqrt{s} \leq 91) \text{ GeV, } e^+e^-$$

Formula	*a*	*b(β)*	*c(c_I)*	χ^2/N
SM(1)	2.94±0.44	0.22±0.02		3/14
FFM(2)	-7.28±1.06	3.01±0.14		9/14
CLM(LM)(3)	7.92±1.15	-1.40±0.28	0.31±0.02	2/14
PQCG(4)	1.00±0.91	0.45±0.11	1.26±0.07	3/14

$$(14 \leq \sqrt{s} \leq 130) \text{ GeV, } e^+e^-$$

SM(1)	2.94±0.43	0.22±0.02		3/16
FFM(2)	-8.33±0.97	3.16±0.13		16/16
CLM(LM)(3)	9.46±1.12	-1.86±0.28	0.34±0.02	3/16
PQCD(4)	2.01±0.90	0.30±0.15	1.38±0.16	3/16

---

* In the interval $(3 \leq \sqrt{s} \leq 50)$ GeV the same results are obtained as in the interval $(3 \div 60)$ GeV.

109

$(10 \leq \sqrt{s} \leq 130)$ GeV, e^+e^-

SM(1)	2.97±0.45	0.22±0.02		3/18
FFM(2)	-6.38±0.72	2.91±0.07		26/18
CLM(LM)(3)	9.20±0.99	-1.80±0.28	0.34±0.02	3/18
PQCD(4)	2.95±0.61	0.21±0.04	1.47±0.06	3/18

The reason of the rapid growth of the multiplicity in the beginning (up to $\sqrt{s} \approx 5$ GeV) seems to be in the significant absorption of slow secondaries in the heavy target nucleus Ta [5]. In higher interval the intranuclear scattering (cascading) is more significant, than absorption.

Table 8.

Values of parameters a and b in the approximation of the $< n(s) >$ dependence by formula (4) (PQCD) for e^+e^--collisions (fixed values of c_i (formula (5))

a	b	c_i fix	Energy range $(\sqrt{s})$GeV	χ^2/N
2.73±0.11	0.132±0.001	1.63±(N_q=3)	1.5÷200	85/48
3.28±0.14	0.102±0.001	1.70(N_q=4)	4÷200	93/43
5.89±0.24	0.070±0.001	1.77(N_q=5)	14÷200	16/31

At more higher energies (>10 GeV) the role of neutral particles in the total multiplicity increases and one observes a less rapid growth of the multiplicity of charged secondaries (confirmed by experimental data) [11].

It is interesting to be mentioned, that in contrast to pp and especially to e^+e^--collision, in the analysis of $< n(s) >$ dependence in pTa-collisions in the framework of CLM (LM) (3) the logarithmic term dominates and the parameter c is practically equal to zero. The reason seems to be following: in this energy range in pTa-collision

the jet structure is less pronounced, than in e^+e^- and pp-collisions. (Table 9, Fig. 1).

Table 9.

Values of coefficients in the approximation of the $<n(s)>$ dependence by formula SM(1), CLM, LM(3). e^+e^- and pTa-collisions. Energy range $(2 \leq \sqrt{s} \leq 22)$ GeV

e^+e^- -collisions

Formula	a	$b(\beta)$	c	χ^2/N
SM(1)	1.97±0.12	0.28±0.01		10/16
CLM(LM)(3)	3.33±0.55	-0.45±0.08	0.29±0.02	9/16

pp-collisions

SM(1)	1.21±0.07	0.32±0.01		3/14
CLM(LM)(3)	1.06±0.06	0.33±0.02	0.13±0.03	8/14

pTa – collisions

SM(1)	1.65±0.08	0.45±0.02		43/6
CLM(LM)(3)	-4.78±1.13	4.07±0.60	0.062±0.0124	3/6

CONCLUSIONS

1. The $<n(s)>$ dependence on energy of the average multiplicity of charged secondary hadrons in e^+e^-- collisions is in principal well described by the statistical model SM(1). The best description is obtained for high energy intervals ((10-200), (14-130), (10-130), (14-91)) GeV, when in each event more than six particles are produced (multiparticle

events). The description of the $<n(s)>$ dependence in the framework of the same model of pp-collisions is significantly worse. It is seen most well if the results in the same energy intervals are compared.

2. The Cluster (Lund) model and PQCD(4) describe date rather well but Cluster (Lund) model is more preferable.

3. In the description of pp- collisions by formula (3) (CLM(LM)) as a rule the logarithmic term is more preferable, than in e^+e^--collisions (in the same energy intervals) (Tables 2, 3, 6). This may be the reflection of the fact, that in pp-collisions the most part of secondaries is produced outside of jets.

4. In e^+e^-- collisions the influence of the $\ln^2 s$ term (coefficient c) is more pronounced, than in pp and pTa – collisions. This may be the reflection of the fact, that the jet structure in e^+e^--collisions is more pronounced, than in pp- and pTa-collisions. The fast growth of the average multiplicity in pTa-collisions is caused by the absorption of slow secondaries. Slower growth of the multiplicity above 10 GeV seems to be caused by the growth of the role of neutral particles in the total multiplicity.

6. The Field-Feynman model describes well the data for e^+e^--collisions only in high energy intervals.

REFERENCES

1. V.G. Grishin. Sov. J.Nucl. Phys. 1983, **38**, 967.
   V.G. Grishin. Kvarki i adroni vo vzaimodeistviakh chastits vysokikh energii. M., 1988 (Russian).
   R. D. Field, S. Wolfram. Nucl. Phys. B. 1983, **213**, 65.
2. V. S. Murzin and L. T. Saricheva. Vzaimodeistvia adronov visokikh energii. M., 1983 (Russian).
   R. D. Field, R. P. Feynman. Nucl. Phys. B. 1980, **136**, 1.
3. Fujivara et al. Nucl. Phys. 1983, **A40,** 509.
4. P. Albrew et al. CERN-EP/2000-023, 7/2, 2000.

Charged and identified particles in the hadronic decay. . . from (130-200) GeV (DELPHI Collaboration).

5. P. Albrew et al. CERN-PPE/96-05, 22/1, 1996.

   Charged particles multiplicity in e^+e^--interactions at $\sqrt{s} = 130$ GeV (DELPHI Collaboration).

6. P. Albrew et al. Z. Phys. C. (Particles and Fields) 1991, **50**, 185.

7. P. Albrew et al. Scaling violation in multiplicity distributions at 200 and 900 GeV; CERN-EP/85-197. 2/12, 1985.

8. D. Brick et al. Phys. Rev. D. 1989, 39, 2484.

9. M. A. Dasaeva et al. Sov. J. Nucl. Phys. 1984, **39**, 846.

10. N. S. Grigalashvili et al. Sov. J. Nucl. Phys., 1988, **48**, 476.

11. E. N. Kladnitskaya. Fizika elementarnikh chastits i atomnogo iadra. 1982, **13**, 669.

Tbilisi State University

ლ. ახობაძე, ვ. გარსევანიშვილი, ი. თეჟბაძე,
თ. ჯალაღანია, გ. ვანიშვილი

e^+e^-, pp- და pA-პროცესებში დაყხებებში დაბადებული მეორადი დამუხტული ადრონების საშუალო მრავლობითობის ენერგიისაგან დამოკიდებულების შედარებითი ანალიზი

დასკვნა

e^+e^--ელექტრონ-პროტონის, pp-პროტონ-პროტონის (ანტი-
პროტონის), pA-პროტონ-ბირთვის დაყხებებში დაბადებუ-
ლი მეორადი დამუხტული ადრონების $\langle n(s) \rangle$-საშუალო
მრავლობითობის ენერგიისაგან დამოკიდებულების შედა-
რებითი ანალიზია, ჩატარებულია რიგორცა კლასიკური,
ასევე კვარქ-პარტონული მოდელების საფუძველზე.

ნახვენებია, რომ ექსპერიმენტს ყველაზე კარგად აღ-
წერს კლასიკური (ლუნდ) მოდელები. მაღალენერგეტი-
კულ არეში e⁺e⁻-დაჯახებებისათვის კარგად მუშაობს
სტატისტიკური მოდელი.

INFLUENCE OF REVERSIBLE RELAXATION ON SINGLE-PULSE ECHO DECAY IN MAGNETS

A.Akhkalkatsi, T.Gegechkori*, G.Katalandze, G.Mamniashvili*, Z.Shermadini

ABSTRACT. In the present work it was studied the single-pulse echo properties in the multipulse excitation mode in a number of magnets. It was discussed the role of different SPE formation mechanisms in connection with the interpretation of the obtained experimental results. It was studied the decays of single-pulse and two-pulse echoes intensities on the duration of radiofrequency pulses and the time-interval between them correspondingly.

It was discussed the role of reversal transverse relaxation processes for the interpretation of unusually short single-pulse echo transverse relaxation times observed in lithium ferrite.

The single-pulse echo (SPE) is a resonance response of spin-system on the application of solitary exciting radiofrequency (RF) pulse arising at a time approximately equal to the pulse duration after its termination. Though SPE was discovered by Bloom yet in 1955 soon after Hahn's discovery of the famous two-pulse echo (TPE) phenomena, the mechanism of its formation appeared to be far more complicated, as compared with the TPE one, and continues to attract the attention of researchers [1].

SPE formation mechanisms could be conditionally classified on so-called edge-type ones when RF pulse edges act like two RF pulses in the Hahn method – such as the nonresonant mechanism [2] and the distortion mechanism [3], and also internal mechanisms due to the presence in the spin-system dynamics particular nonlinearities, as example, connected with a strong dynamic frequency shift of the NMR frequency or with a nonlinear dynamics of nuclear spins due to the simultaneous presence of large Larmor and Rabi inhomogeneous broadenings of the NMR line [1].

In this work we consider in more details the so-called multipulse mechanism of SPE formation, presented in work [1], for systems with both types of frequency inhomogeneities of NMR lines. An important example of such system is multidomain magnets, for example, lithium ferrite. Earlier in work [4] it was investigated by us the peculiarities of SPE formation in this magnets. It was established that its properties sharply differ from SPE properties in cobalt where it was formed by the distortion mechanism. Therefore, the conclusion was made on the possible effectiveness of new internal mechanism of the SPE formation in lithium ferrite. But in work [4] the SPE formation mechanism in lithium ferrite was not finally established what was made in works [5,6] where it was shown that SPE and its secondary signals properties in lithium ferrite were well described by the multipulse mechanism of formation [1].

Shakhmuratova et al. [1] used the formalism of statistical tensors to perform a theoretical investigation of the formation of SPE and its secondary signals in the presence of large Larmor and Rabi inhomogeneous broadenings of the NMR line, which, e.g. takes place in multidomain ferromagnets, when the repetition period of RF pulse T satisfies the following inequality for the characteristic relaxation parameters:

$$T_3 << T_2 < T < T_1, \tag{1}$$

where T_1 is the spin-lattice relaxation time, T_2 is the transverse irreversible relaxation time, T_3 characterizes the transverse reversible relaxation time ($T_3 \sim 1/\sigma$, where σ is the halfwidth at halfmaximum of the inhomogeneously broadened line).

Under these conditions, the RF cycles are applied to a nonequilibrium spin system, and in the end of each period T we should take into account only the longitudinal component of the nuclear magnetization as the initial condition for the consideration of the dynamics of the spin system.

It was shown that the dephasing of the spin system, which is accumulated in the course of n-fold repetition of the pulsed excitation, is recovered during a time interval following the (n+1)th "read-out" pulse in the multipulse sequence, which leads to the formation of an

116

SPE and its secondary signals at time moments multiple of the duration of the RF pulse τ after the termination of the "read-out" pulse.

In work [6] it was shown that obtained in [1] by the statistical tensors method expression for the transverse components of nuclear magnetizations could be obtained in the framework of the usual classical-approach by solving the system of Bloch equations from [2], where it was allowed for both types of inhomogeneous broadenings of NMR lines and condition (1). But the approach of work [7] using the Mims transformation matrix method [8], appeared to be more visual.

Let us consider the case when a local static magnetic field H_n is directed along Z axis and RF field is along X axis of the rotating coordinate system (RCS) when an effective magnetic field modulus in RCS is given by the expression:

$$H_{eff} = \frac{1}{\gamma_n}\sqrt{\Delta\omega_j^2 + \omega_1^2} \, ,$$

where angle ψ_j between

$$\mathbf{H}_{effj} = \frac{1}{\gamma_n}(\Delta\ \omega_j\hat{\mathbf{z}} + \omega_1\hat{\mathbf{y}}) \tag{2}$$

(where the $\hat{\mathbf{z}}$ and $\hat{\mathbf{y}}$ are unit vectors in RCS) and Z axis is defined by the relation:

$$\sin\psi_j = \omega_1/\Delta\omega_j' \ ; \quad \cos\psi_j = \Delta\omega_j/\Delta\omega_j' \, , \text{ and } \Delta\omega_j' = \sqrt{\Delta\omega_j^2 + \omega_1^2}$$

is the angular velocity of the precession of the j-th isochromate around $\mathbf{H}_{effj}$, $\Delta\omega_j = \omega_{NMR} - \omega_{RF}$ is the detuning for the j-th isochromate, $\omega_1 = \gamma_n\eta H_1$ is the pulse amplitude in frequency units, η is the gain of the RF field, γ_n is the nuclear gyromagnetic ratio.

Time t characterizes time interval after a pulse termination and is counted from the back front of RF pulse.

The transformation matrix (R) describing the rotation of the magnetization vector $\mathbf{m} = (m_x; m_y; m_z)$ around $\mathbf{H}_{eff}$ is [8]:

$$(R) = \begin{pmatrix} S_\psi^{\,2} + C_\psi^{\,2}C_\theta & -C_\psi S_\theta & S_\psi C_\psi(1-C_\theta) \\ C_\psi S_\theta & C_\theta & -S_\psi S_\theta \\ S_\psi C_\psi(1-C_\theta) & S_\psi S_\theta & C_\psi^{\,2}+S_\psi^{\,2}C_\theta \end{pmatrix},$$

where C_ψ, S_ψ, C_θ and S_θ stand for $\cos\psi$, $\sin\psi$, $\cos\theta$ and

$\Psi = tg^{-1}\left(\dfrac{\omega_1}{\Delta\omega_j}\right)$ is an angle between the effective field $\mathbf{H}_{eff}$ and $\mathbf{Z}$

axis. θ is the angle by which the magnetization turns about $\mathbf{H}_{eff}$ during the pulse time τ : $\theta = \gamma H_{eff}\tau$, where H_{eff} is given by (2).

Let us consider firstly the case of single-pulse excitation. Let

$$X_j = m_{xj}/m\,;\, Y_j = m_{yj}/m\,;\, Z_j = m_{zj}/m \quad \text{and} \quad \mu = (X_j; Y_j; Z_j),$$

where m is the magnetization modulus. If before the excitation by a RF pulse the nuclear spin system was at the equilibrium conditions $\mu_{eq} = (0;0;1)$, then the result of RF pulse action is presented by $\mu = (R) \cdot \mu_{eq}$.

After the termination of RF pulse isochromates precess freely around the $\mathbf{Z}$ axis that is described by the matrix:

$$(R_\varphi) = \begin{pmatrix} C_\varphi & -S_\varphi & 0 \\ S_\varphi & C_\varphi & 0 \\ 0 & 0 & 1 \end{pmatrix},$$

where $\varphi = \Delta\omega_j t$ is the angle of rotation of an isochromate around the $\mathbf{Z}$ axis, and t is the time elapsing from the trailing edge of pulse.

Therefore, we have finally:

$$\boldsymbol{\mu}_1 = \left(R_\varphi\right)(R)\boldsymbol{\mu}_{eq} = \begin{pmatrix} C_\varphi S_\psi C_\psi (1-C_\theta) + S_\varphi S_\psi S_\theta \\ S_\varphi S_\psi C_\psi (1-C_\theta) - C_\varphi S_\psi S_\theta \\ C_\psi^2 + S_\psi^2 C_\theta \end{pmatrix}.$$

Expressions for the magnetization components in $\boldsymbol{\mu}_1$ coincide with ones obtained in [1] and [2] for the case of single-pulse excitation.

Let us find now the effect of n-fold repetition of the pulsed excitation in the frameworks of model [1] when before the next RF pulse of a train only the longitudinal component of nuclear magnetization remains. It is not difficult to prove by successive matrix multiplication that the expression for equilibrium nuclear magnetization $\boldsymbol{\mu}_n$ before the final "read-out" $n+1$ th pulse is:

$$\boldsymbol{\mu}_n = \left(C_\psi^2 + S_\psi^2 C_\theta\right)^n \boldsymbol{\mu}_{eq}.$$

Then the result of excitation by the "read-out" pulse and following free precession of magnetization is described directly for the new initial conditions:

$$\boldsymbol{\mu}_{n+1} = \left(R_\varphi\right)(R)\boldsymbol{\mu}_n = \left(C_\psi^2 + S_\psi^2 C_\theta\right)^n \begin{pmatrix} C_\varphi S_\psi C_\psi (1-C_\theta) + S_\varphi S_\psi S_\theta \\ S_\varphi S_\psi C_\psi (1-C_\theta) - C_\varphi S_\psi S_\theta \\ C_\psi^2 + S_\psi^2 C_\theta \end{pmatrix}.$$

These expressions coincide with the ones obtained in [1] using the formalism of statistical tensors. The n-th degree multiple has a simple physical meaning of a longitudinal nuclear magnetization created by the n elementary pulses of a multipulse train reflecting the spin system memory to the excitation. The expressions for the SPE and its secondary echo signals using similar expressions for nuclear magnetization components were obtained in [1].

It is easy to carry out this approach also for the case of periodic two-pulse excitation which is of interest for describing the secondary echo signals of two-pulse echo (TPE) in the investigated systems.

One could see that the expression for $\boldsymbol{\mu}_{n+1}$ in the case of single-pulse periodic excitation could be presented as:

$$\mu_{n+1} = Z^n \begin{pmatrix} C_\varphi X - S_\varphi Y \\ S_\varphi X + C_\varphi Y \\ Z \end{pmatrix} \quad (3)$$

Where X, Y, Z are the components of nuclear magnetization immediately after the single-pulse excitation. Similarly to this for the periodic two-pulse train allowing for condition (1) one could easily obtain components of nuclear magnetizations after (n+1)th "read-out" pair of RF pulses in the form of (3) where this time X,Y,Z are components of nuclear magnetization immediately after the solitary two-pulse excitation which could be readily obtained from relation:
$\mu_1 = RR_\varphi R\mu_{eq}$ and

$$X = (S_\psi^2 + C_\psi^2 S_\theta) \cdot [C_\varphi S_\psi C_\psi (1-C_\theta) + S_\varphi S_\psi S_\theta] -$$
$$- C_\varphi S_\theta \cdot (S_\varphi S_\psi C_\psi (1-C_\theta) - C_\varphi S_\psi S_\theta) + S_\psi C_\psi (1-C_\theta) \cdot (C_\psi^2 + S_\psi^2 C_\theta)$$
$$Y = C_\psi S_\theta \cdot [C_\varphi S_\psi C_\psi (1-C_\theta) + S_\varphi S_\psi S_\theta] +$$
$$+ C_\theta \cdot [S_\varphi S_\psi C_\psi (1-C_\theta) - C_\varphi S_\psi S_\theta] \cdot S_\psi S_\theta \cdot (C_\psi^2 + S_\psi^2 C_\theta)$$
$$Z = S_\psi C_\psi (1-C_\theta) \cdot [C_\varphi S_\psi C_\psi (1-C_\theta) + S_\varphi S_\psi S_\theta] +$$
$$+ S_\psi S_\theta \cdot [S_\varphi \cdot S_\psi C_\psi (1-C_\theta) - C_\varphi S_\psi S_\theta] + [C_\psi^2 + S_\psi^2 C_\theta]^2.$$

Here, as in the case of single-pulse excitation, the presence of a n-th degree multiplier reflects the memory of spin system on its excitation by the train of double RF pulses that results similarly to [1] in the formation of TPE secondary signals.

Let us present the main experimental results obtained in this work. Measurements were carried out by the NMR spectrometer using diamagnetically diluted lithium ferrite $Li_{0.5}Fe_{2.35}Zn_{0.15}O_4$, Co and Co_2MnSi samples described in work [3,5].

Let us firstly present the results of comparative analysis of SPE and TPE amplitudes and their secondary signals in the function of repetition period T of exciting RF pulses.

In Fig.1 is presented the oscillograms of SPE and its secondary signals at the optimal value of repetition period T of RF pulses, and

Fig.2 indicate the oscillograms of TPE and its secondary signals at the optimal value of repetition period T of RF pulses and Fig.3 and 4 show dependences of their intensities on T in lithium ferrite.

The particular attention was paid to the investigations of SPE at large T when the condition of single-pulse excitation $T >> T_1$ obeyed what was made using storage oscilloscopes.

Oscillograms in Fig.5 show the process of complete disappearance of SPE signal in lithium ferrite in the limit of single-pulse excitation (Osc.3 in Fig.5) and the absence of any contribution in the SPE intensity due to the distortion mechanism. From all magnets studied by us only in lithium ferrite it was not found such contribution. As it is known [3], the intensive SPE signals at single-pulse excitation were observed in ferromatellic hexagonal cobalt and in intermetallic Co_2MnSb. A similar sufficiently intensive SPE signal was observed in halfmetallic NiMnSb and a weaker signal was found in such "bad" metal as manganite. For example, let us present the SPE and TPE dependences for Co and Co_2MnSi on T in Fig.6 and 7, correspondingly. In these materials the main formation SPE mechanism is the distortion mechanism [3]. The effectivity of this mechanism in these materials was confirmed by us by the effect of SPE enhancement at pulsed frequency distortion of the exciting RF pulse trailing edge introduced similarly to work [10]. Similar excitation in the case of lithium ferrite resulted only in the suppression of SPE signal in this material.

From the obtained results it could be noted the correlation of the physical properties of studied by us magnets with intensities of observed SPE signals in them, formed by the distortion mechanism. Beginning from the most intensive signal in ferromatal Co down to weak one in "bad" ferrometal manganite and its full disappearance in magnetic dielectric lithium ferrite. This problem could present some interest from the point of view of the practical applications of SPE for the aims of magnetic materials science.

The other interesting problem is the investigation of influence of reversible and irreversible transverse relaxations on the SPE amplitude.

In work [2] it was shown that with a help of SPE signal one could define the transverse relaxation time T_2 in magnets of $MnFe_2O_4$ type. The transverse relaxation time T_2 measured by this method does not coincide with the value measured by the TPE method [2]. As it was

turned out the SPE signal dependence on the duration τ of the exciting RF pulse is defined not only by the irreversible relaxation but also by other mechanisms related with the SPE formation, for instance, by the inhomogeneous broadening of the NMR line [10].

Lithium ferrite is the interesting object to study the relaxation processes at the SPE formation because of the absence of the contribution of distortion mechanism in it, and the SPE formation process is only described by the multipulse mechanism the physical nature of which was above discussed.

In Fig.8 it is presented the experimental dependences of SPE main and secondary signals intensities (I_1^s, I_2^s) and in Fig.9 the corresponding dependences for TPE main and secondary signals in lithium ferrite. As it is known, in the case of the effectivity of the distortion mechanism the SPE and TPE signals are change similarly at the variation of their excitation conditions [3] and in this case usually holds the following relation between transverse relaxation times of TPE (T_2) and SPE ($^sT_2$):

$$^sT_2 = (0.5 - 0.8)\, T_2,$$

what is not the case for lithium ferrite where $^sT_2$ is about 30 times shorter as compared with T_2, as example, a $f_{NMR} = 73.4$ MHz, $T_2 = 1200$ μs and $^sT_2 = 40$ μs .

So, the results of experimental investigations of SPE transverse relaxation time in lithium ferrite speak in the favor of the essential influence of reversible transverse relaxation transverse on the SPE relaxation time in lithium ferrite in correspondence with works [2,10].

In conclusion, let us note that in the present work it was studied the SPE properties in the multipulse excitation mode in a number of magnets. It was discussed the role of different SPE formation mechanisms in connection with the interpretation of the obtained experimental results. It was discussed the decay of SPE and TPE intensities on the duration of RF pulses and the time interval between them, correspondingly. It was discussed the role of reversal transverse relaxation for the interpretation of the observed unusually short transverse relaxation times of the SPE signals in lithium ferrite.
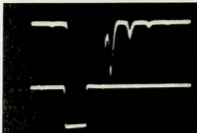
Fig.1. Oscillograms of the SPE and its secondary signals from ^{57}Fe nuclei in lithium ferrite. The lower beam indicates the position and duration of the RF pulses ($T = 77$ K, $f_{NMR} = 71, 6$ MHz, $\tau = 10\,\mu s$, $T = 300\,\mu s$).
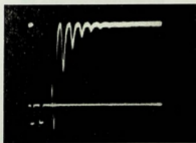
Fig.2. Oscillograms of the TPE and its secondary signals in lithium ferrite. The lower beam shows the position and duration of the RF pulses ($T = 77$ K, $f_{NMR} = 71.6$ MHz, $\tau_1 = 1.8\,\mu s$, $\tau_2 = 2.2\,\mu s$, $\tau_{12} = 5\,\mu s$, $T = 300\,\mu s$).
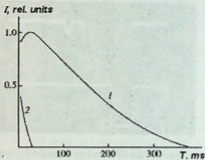
Fig.3. The intensity of the SPE signal (1) and its secondary signal (2) as functions of the repetition period of RF pulses T in lithium ferrite.
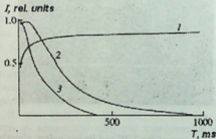
Fig.4. The intensity of TPE (1) and its secondary signals (2), (3) as functions of the period of repetition of the RF pulses T in lithium ferrite.
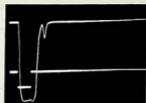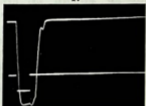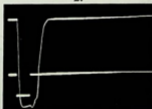
Fig.5. SPE signal (1-3) in lithium ferrite at the influence of RF pulse repetition period T showing the process of complete disappearance of the SPE signal when T becomes more than ~ 1 sec (3).
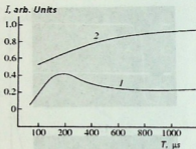
Fig. 6. The intensity of SPE (1) and TPE (2) as functions of the period of repetition of the RF pulses T in the intermetallic compound Co$_2$MnSi. (T = 77 K, f$_{NMR}$ = 71.6 MHz, τ = 10 μs, T = 300 μs).

Fig. 7. The intensity of SPE (1) and TPE (2) as functions of the period of repetition of the RF pulses T in hexagonal cobalt.
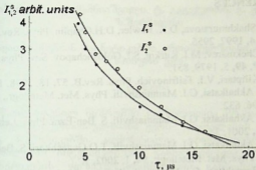
Fig.8. Intensities of SPE main and secondary signals as functions of the duration of RF pulse τ in lithium ferrite at $f_{NMR} = 74 MHz$.
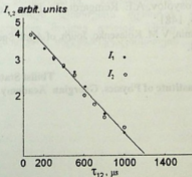
Fig.9. Intensities of TPE main and secondary signals as functions of the interval between RF pulses τ_{12} in lithium ferrite at $f_{NMR} = 74$ MHz.

REFERENCES

1. L.N. Shakhmuratova, D.K. Fowler, D.H.Chaplin. Phys. Rev., **A55**, 4, 1997, 2955.

2. V.P.Chekmarev, M.I. Kurkin, S.I. Goloshchapov. Sov. Phys. JETP, **49**, 5, 1979, 851.

3. I.G. Kiliptari, V.I. Tsifrinovich. Phys. Rev.B. **57**, 18, 1998, 1554

4. A.M. Akhalkatsi, G.I. Mamniashvili. Phys. Met. Metallogr., **81**, 6, 1996, 632.

5. A.M. Akhalkatsi, G.I. Mamniashvili. S. Ben-Ezra. Phys. Lett. **A291**, 2001, 34.

6. A.M. Akhalkatsi, G.I. Mamniashvili. T.O.Gegechkori, S. Ben-Ezra. Phys. Met. Metallogr., **94**, 1, 2002, 1.

7. T.O.Gegechkori, G.I. Mamniashvili. Proc.of I. Javakhishvili Tbilisi State University, Physics, **36**, 2001, 12.

8. W.B. Mims, K. Nassau, J.D. McGee. Phys. Rev. **123**, 6, 1961, 2059.

9. V.I. Tsifrinovich, E.S. Mushailov, N.V. Maltsev, A.M. Bessmertny, E.A. Glozman, V.K. Maltsev, O.V. Novosyolov, A.E. Reingardt. Zh. Eksp. Teor. Fiz., **985**, 88, 4, 1481.

10. V.S. Kuzmin, V.M. Kolesenko. Journ. of Appl. Spectr., **70**, 5, 2003, 694.

Tbilisi State University
*Institute of Physics, Georgian Academy of Sciences

ა. ახალკაცი, გ. მამნიაშვილი, რ. გეგეჭკორი, გ. ქათალბაძე, ზ.შერმადინი

მრავალდომენიან მაგნეტიკებში ერთიმპულსიანი ბირთვული სპინური ექო

დასკენა

წარმოდგენილი ნაშრომში განხილულია მრავალიმპულსი-
ან რეჟიმში ერთიმპულსიანი ექოს სიგნალების თვისებები-
რიგ მაგნეტიკებში. აღნიშნული ერთიმპულსიანი ექოს
სიგნალების ინტენსივობის განსხვავებული კორელაცია
მაგნეტიკების ფიზიკურ თვისებებთან. განხილული ერთი-
იმპულსიანი ექოს ფორმირების სხვადასხვა მოდელებით
როდ მიღებული ექსპერიმენტული მონაცემების ინტერ-
პრეტაციისათვის. შესწავლილია ერთიმპულსიანი და ორ-
იმპულსიანი ექოს ინტენსივობის დამოკიდებულება რადიო-
სიხშირული იმპულსების ხანგრძლივობაზე და შესაბამისად
მათ შორის დაშორებაზე. განხილული შემუშავებ რე-
ლაქსაციის როლო ლითოდოლოგიის ფერხული ერთიმპულსიან
ექოში უჩვეულოდ მოკელე დროით მქონე განიხა რელაქ-
საციის სიგნალების ინტერპრეტაციისათვის

ZERO-POINT VIBRATION ENERGY WITHIN QUASI-CLASSICAL APPROXIMATION: BORON NITRIDES

L. Chkhartishvili

ABSTRACT. The method of calculation of the substance constituent atoms zero-point vibration energy within the initial quasiclassical approximation is elaborated. By this way the ground state vibration energy values for boron nitride molecule, isolated sheet, hexagonal, cubic and wurtzite-like crystals are found as 0.178, 0.242, 0.266, 0.330 and 0.323 eV/mole, respectively.

1. INTRODUCTION

Boron nitride phases form the class of materials of special scientific and technological interest for their superior bonding, electronic and optical properties. Boron nitride with the general chemical formula BN can exist as one- (diatomic molecule), two- (tubular and fullerene-like surfaces) and three-dimensional (layered hexagonal $h-BN$ and rhombohedral $r-BN$, relatively dense cubic $c-BN$ and wurtzite-like $w-BN$ crystals, turbostratic and amorphous films) structures. The development of theoretical approaches that do not require considerable computational effort but provide a reasonable accuracy in the prediction of main physical characteristics is particularly important for the study of such kind of substance with wide variation of the structure types. A number of structural and electron energy spectrum parameters of boron nitrides were obtained [1-9] by the new effective computing method based on the quasiclassical approximation (summarization of the physical theory is given in [10], the key mathematical aspects see in [11-12]). In the present work the same approach is applied to estimate the energies of zero-point vibrations in boron nitride modifications. In next section we justify method for this task. Then results of calculations are given in comparison with available data.

2. STANCE OF ZERO-POINT VIBRATION ENERGY WITHIN THE INITIAL QUASICLASSICAL APPROXIMATION

Under the term of 'substance' is implied atoms and polyatomic structures at the ground state, i.e. molecules and crystals, which can be considered as-an interacting electron system affected by the stationary external electrical field of nuclei fixed at the sites in given structure. And so, its physical properties are mainly determined by the electron energy spectrum. The quasi-classical expression for bounded state energies obtained by Maslov [13] yields [14] that for substance inner (self-consistent field) potential the precise and quasiclassical electronic spectra are close to one another. On this basis the scheme of quasi-classical representation of charge density and potential distributions in substance has been elaborated [10] which is useful to estimate energy of atoms vibrating near the equilibrium sites in structure.

The quasi-classical limit means the truncation of electron states wave functions exponentially decaying tails in the classically forbidden regions. In such approximation partial charge densities of the space-averaged atomic orbitals equal zero outside the classical turning points and a nonzero constants within the range between them. Consequently, full charge densities in consistent system are expressed by the step-like partial functions. Using the Poisson equation the radial dependencies of the atomic potentials also can be represented as step-like functions if substituted by the space-averaged values inside each of the uniform charge density regions.

Let us assume that $\vec{d}_{(i)}$ are the basis vectors of the unit cell of a crystal with N atoms, $(i) = 1, ..., N$. In this case, the point $\vec{d}_{(i)} + \vec{t}$ corresponds to the equilibrium position of the center of (i)-type atom belonging to the unit cell with translational vector $\vec{t}$. Therefore, the total density of the nuclear and electronic charges in the atom and the potential of the field induced by these charges at the point $\vec{r}$ can be represented by the functions $\rho_{(i)}(\vec{r} - \vec{d}_{(i)} - \vec{t})$ and $\varphi_{(i)}(\vec{r} - \vec{d}_{(i)} - \vec{t})$. If the affecting atoms are fixed at their sites (this is equivalent to the time averaging of their vibrations), the potential energy of the (i)th atom of the central unit cell (i.e. with $\vec{t} = 0$) displaced by the vector

131

$\vec{r}$ from the equilibrium position is defined as

$$U_{(i)}(\vec{r}) = \sum_{l}' \sum_{(k)=1}^{(k)=N} \int d\vec{r}'(\rho_{(i)}(\vec{r}' - \vec{d}_{(k)l} - \vec{r})\varphi_{(k)}(\vec{r}' - \vec{d}_{(k)l} - \vec{t}) +$$

$$+ \rho_{(k)}(\vec{r}' - \vec{d}_{(k)l} - \vec{t})\varphi_{(i)}(\vec{r}' - \vec{d}_{(i)l} - \vec{r}))/2 .$$

The prime on the summation sign indicates that the term with $\vec{t} = 0$ and $(k) = (i)$ corresponding to the self-action is omitted (besides, the formula is symmetrized with respect to the contributions of interacting charges, because these approximations not related by the Poisson equation were used upon quasi-classical parameterization of the charge density and potential).

The central-field approximation for the constituent atoms permits us to represent this potential energy as the sum of the contributions that depend only on the squares of the distances from the point $\vec{r} + \vec{d}_{(i)}$ to the point $\vec{d}_{(k)} + \vec{t}$:

$$U_{(i)}(\vec{r}) = \sum_{l}' \sum_{(k)=1}^{(k)=N} U_{(ik)l}(r_{(ik)l}^2 - 2(\vec{r}_{(ik)l}\vec{r}) + r^2) ,$$

where $\vec{r}_{(ik)l} = \vec{d}_{(k)l} + \vec{t} - \vec{d}_{(i)}$ denotes the radius vector of the (k)th atom with respect to the (i)th atom. In order to estimate the energy of small-amplitude lattice vibrations, we expand each contribution into a power series of the variable parts of the arguments and retain only constant and linear terms. The terms responsible for the vibrations are as follows:

$$U_{(i)vibration}(r) = \sum_{l}' \sum_{(k)=1}^{k=N} r^2 \, dU_{(ik)l}(r_{(ik)l})/2dr_{(ik)l} .$$

In quasi-classical scheme, the pair potential energies $U_{(ik)l}(r_{(ik)l})$ are linear combinations of the functions $V(r_{(ij)l}, r_{(ik)l}, r_{(ik)l})$, which determine the volumes of the intersection of the layers with uniform charge density and potential in the interacting atoms:

132

$$V_{(ik)jl}(r_{(ik)\overline{z}}) = V(r_{(i)j}, r_{(k)l}) + V(r_{(i)j-1}, r_{(k)l-1}) - $$
$$-V(r_{(i)j}, r_{(k)l-1}, r_{(k)\overline{z}}) - V(r_{(i)j-1}, r_{(k)l}, r_{(ik)\overline{z}}).$$

Here $r_{(i)j}$ are the outer radii of the atomic layers, $j = 1, \ldots, q_{(i)}$ ($q_{(i)}$ is the total number of uniform layers in (i) atom), and $V(R_1, R_2, D_{12})$ is the continuously differentiable piecewise analytical algebraic function determining the volume of the intersection of two spheres with radii R_1 and R_2 whose centers are spaced at D_{12} (this universal geometrical function was derived in an explicit form in [15] when formulating the problem regarding the quasi-classical calculation of the band structure of a crystal). Consequently, by introducing the charge density $\rho_{(i)j}$ and the potential $\varphi_{(i)j}$ values in the atomic layers the molar energy of zero-point vibrations in the crystal can be written in the form

$$E_{Vibration} = $$
$$= \sum_{(i)=1}^{(i)=N} \frac{3}{2} \sqrt{\sum_{\overline{i}}^{\overline{i}} \sum_{(k)=1}^{(k)=N} \sum_{j=1}^{j=q_{(i)}} \sum_{l=1}^{l=q_{(k)}} \frac{\rho_{(i)j}\varphi_{(k)l} + \rho_{(k)l}\varphi_{(i)j}}{2M_{(i)}r_{(ik)\overline{z}}} \frac{\partial V_{(ik)jl}(\overline{r}_{(ik)\overline{z}})}{\partial r_{(ik)\overline{z}}}},$$

$$\partial V_{(ik)jl}(r_{(ik)\overline{z}}) / \partial \overline{r}_{(ik)\overline{z}} = $$
$$= \partial V(r_{(i)j}, r_{(k)l}, r_{(ik)\overline{z}}) / \partial r_{(ik)\overline{z}} + \partial V(r_{(i)j-1}, r_{(k)l-1}, r_{(ik)\overline{z}}) / \partial r_{(ik)\overline{z}} - $$
$$-\partial V(r_{(i)j}, r_{(k)l-1}, r_{(ik)\overline{z}}) / \partial r_{(ik)\overline{z}} - \partial V(r_{(i)j-1}, r_{(k)l}, r_{(ik)\overline{z}}) / \partial r_{(ik)\overline{z}}.$$

$M_{(i)}$ denotes the mass of the (i)th atom, and the frequencies of lattice vibrations are expressed through the partial derivative $\partial V(R_1, R_2, D_{12}) / \partial D_{12}$ which is the continuous piecewise analytical algebraic function:

$$\partial V(R_1, R_2, D_{12}) / \partial D_{12} = 0 \qquad D_{12} \leq R_2 - R_1$$

$$= 0 \qquad D_{12} \leq R_1 - R_2$$

$$= -\pi((R_1 + R_2)^2 - D_{12}^2)(D_{12}^2 - (R_1 - R_2)^2) / 4D_{12}$$

$$|R_1 - R_2| \leq D_{12} \leq R_1 + R_2$$

$$= 0 \qquad R_1 + R_2 \leq D_{12}.$$

These relations obtained for infinite crystalline structure can be reduced for case of molecule fixing translational vector at $\vec{t} = 0$.

3. QUASI-CLASSICAL ZERO-POINT VIBRATION ENERGIES IN BORON NITRIDES

The quasi-classical parameters of charge density and potential distributions in constituent atoms B and N (necessary for calculations) were determined within the scheme of Coulomb-like potentials by fitting quasi-classical electron energy levels to the ab initio, namely, Hartree–Fock [16]) ones for isolated atoms (as it is known, need for the large programming resources makes such kind of calculations unrealizable in case of crystals). The obtained values are listed in Table 1. Then using these parameters the molar ground state vibration energies have been calculated for following boron nitride structures (see Table 2):

– diatomic molecule, i.e. isolated B–N bond, what is important object being the building 'block' for any boron nitride solid phase;

– hypothetic two-dimensional hexagonal crystal which also is of special interest because the three-dimensional layered modifications are formed by similar boron nitride sheets and, moreover, fullerene and nano-tube aggregates are bounded by flat or curved fragments of such a sheet;

– hexagonal crystal with two-layer stacking sequence (value found for rhombohedral one with three-layer stacking sequence is almost the same due to substantially weakness of the inter-layer bonding in comparison with intra-layer interactions);

134

Table 1. Quasi-classical parameters of the charge density and potential distributions in B and N atoms (in *atomic units*)

$\varphi_{(B)j}$	$\rho_{(B)j}$	$r_{(B)j}$	j	$r_{(N)j}$	$\rho_{(N)j}$	$\varphi_{(N)j}$
210.5468	56865.14	0.027585	1	0.009446	1982589	878.4581
8.882329	−3.61095	0.509802	2	0.357724	−	20.22523
3.652920	−0.00734	0.744122	3	0.549803	10.4497	8.464698
0.206072	−0.01028	4.021346	4	2.909074	−	0.509668
0.000614	−0.00294	4.337060	5	3.204489	0.01939	0.003993
					0.04127	
					0.02188	

Table 2. Quasi-classically calculated zero-point vibration energies of boron nitride structural modifications (in eV/mole)

Modification	$E_{vibration}$
molecule BN	0.178
sheet BN	0.242
h-BN	0.266
c-BN	0.330
w-BN	0.323

− cubic crystal;

− wurtzite-like crystal for which the ratio of lattice constants a and c and internal parameter u were fixed at the 'ideal' values: $(a/c)^2 = u = 3/8$.

The quasi-classically calculated B–N inter-atomic vibration energy, 0.178 eV/mole, is in good agreement (with a deviations ~5%) with the values experimentally found for neutral BN molecule 0.187 eV/mole [17] and 0.188 eV/mole [18]. According to the original (self-consistent-field-type) theoretical method of [19] ground state vibration energy in molecular boron nitride estimated as ≈0.179 eV/mole is almost our quasi-classical result. In [20] it was suggested higher

theoretical value 0.217 eV/mole what is close with 0.216 eV/mole measured in ionized molecule BN^+ [21].

The present calculations of vibration energy are the first for boron nitride crystalline modifications. Earlier these values were only estimated according to the semi-empirical models and/or theoretical phonon spectra.

It is natural that the molar vibration energies quasi-classically found for sheet and hexagonal boron nitrides, 0.242 eV/mole and 0.266 eV/mole, are close one to another. When comparing these energies, it should be taken into account that inter-layer bonds in layered boron nitride structure are substantially weaker than intra-layer bonds and, consequently, inter-layer interaction may be ignored. On the other hand, the atoms of the isolated layer which is a two-dimensional system, nevertheless, can execute vibrations in three independent directions in the physical space. Thus, it is expedient to analyze these predictions jointly (especially because there is no experimental studies for boron nitride sheet being the hypothetic structure). Both of them agree well with semi-empirical value of 0.225 eV/mole for the energy of zero-point vibrations in real h-BN crystal found within the model of a classical force field potential [22] and coincide in order of magnitude with the estimate 0.350 eV/mole made from the theoretical phonon spectrum [23].

It is also natural that determined vibration energies of c-BN and w-BN crystals, 0.330 eV/mole and 0.323 eV/mole, are almost the same. Boron and nitrogen atoms are tetrahedrally surrounded in both of densely packed forms of boron nitride and in considered 'ideal' case, that mimics the real stable wurtzite-like lattices, the w-BN structure differs from the c-BN structure only in the stacking sequence of the B and N atoms. Correspondingly, the nearest-neighbor atomic environments and bonding types in both crystals are sufficiently close and it may be taken for guarantee that their ground state parameters are also similar (the lower symmetry and small deviations of bond lengths in the w-BN structure can result only in some unique features of its properties). It urges on analysis of c-BN and w-BN vibration energies together (especially as w-BN bonding parameters have not been measured). Aforementioned quasi-classical values coincide only in order of magnitude with the semi-empirical estimates based on the model of a classical force field potential: 0.130 eV/mole and

0.210 eV/mole, respectively [22]. However, there is excellent agreement with equal values of 0.320 eV/mole found from the theoretical phonon spectrum [23] and early semi-empirical Debye model [24] for c-BN.

Summarizing the obtained results we can conclude that quasi-classical calculation would be useful for determination of lattice zero-point vibration energy which is important ground state parameter hardly lended itself to measurement in crystals.

REFERENCES

1. L. Chkhartishvili, D. Lezhava, O. Tsagareishvili, D. Gulua. Trudy AMVDG, **1**, 1999, 295 (Russian).

2. L. Chkhartishvili, D. Lezhava, O. Tsagareishvili. J.Solid State Chemistry, **154**, 1, 2000, 148.

3. L. Chkhartishvili, D. Lezhava. Trudy GTU, **6 (439)**, 2001, 87 (Russian).

4. L. Chkhartishvili. Proceedings of the 1st International Boron Symposium. Kütahya: Dumlupinar University Press, 2002, 139.

5. L. Chkhartishvili. J.Solid State Chemistry, **177**, 2, 2004, 395.

6. L. Chkhartishvili. Physics of the Solid State, **46**, 11, 2004, 2126.

7. L. Chkhartishvili. Proceedings of the 2nd International Boron Symposium. Eskişehir: Osmangazi University Press, 2004, 253.

8. L. Chkhartishvili. Transactions of the ICTU, **1**, 2005, 296.

9. L. Chkhartishvili. Physics of the Solid State, **48**, 5, 2006, 606.

10. L. Chkhartishvili. Kvaziklassicheskaya teoriya osnovnogo sostoyaniya veshchestva. Tbilisi: Technical University Press, 2004 (Russian).

11. L. Chkhartishvili. Mathematical Notes, **69**, 3, 2001, 421.

12. L. Chkhartishvili. Mathematical Notes, **77**, 1, 2005, 273.

13. V. P. Maslov. Teoriya vosmushchenij i asimptoticheskie metody. Moscow, 1965 (Russian).

14. P. V. Elyutin, V. D. Krivchenkov. Kvantovaya mekhanika s zadachami. Moscow. 1976 (Russian).

15. L. Chkhartishvili. Trudy GTU, **3**, 411, 1996, 45 (Russian).

16. Ch. Froese-Fischer. The Hartree-Fock Method for Atoms. A Numerical Approach. New York, 1977.

17. K. P. Huber, G. Herzberg. Molecular Spectra and Molecular

Structure. IV. Constants of Diatomic Molecules. New York, van Nostrand Reinhold Co, 1979.

18. M. Lorenz, J. Agreiter, A. M. Smith, V. E. Bondybey. J. Chemical Physics, **104**, 8, 1996, 3143.

19. Yu. G. Khajt, V. I. Baranovskij. Zhurnal strukturnoj khimii, **21**, 1, 1980, 153 (Russian).

20. H. Bredohl, I. Dubois, Y. Houbrechts, P. Nzohabonayo. J.Physics, **B17**, 1, 1984, 95.

21. V.I. Vedeneev, L.V. Gurvich, V.N. Kondrat'ev, V.A.Medvedev, E.L. Frankevich. Energiya razryva khimicheskikh svyazej. Potentsialy ionizatsii i srodstvo k elektronu (Spravochnik). Moscow. 1962 (Russian).

22. Ch. M. Marian, M. Gastreich, J. D. Gale. Phys. Rev., **B62–I**, 5, 2000, 3117.

23. K. Albe. Phys. Rev., **B55–II**, 10, 1997, 6203.

24. P. J. Gielisse, S. S. Mitra, J. N. Plendl, R. D. Griffis, L. Mansur, R. Marshall, E. A. Pascoe. Phys. Rev., **155**, 4, 1967, 1039.

Georgian Technical University

ლ. ხახუტაშვილი

ნუკლეონ რხევების ენერგია კვაზიკლასიკურ
მიახლოებაში: ბორის ნიტრიდები

დასკვნა

დამუშავებულია საწყისი კვაზიკლასიკურ მიახლოებაში
ნივთიერების შემადგენელი ატომების ნუკლეონ რხევების
ენერგიის გამოთვლის მეთოდი. ამ გზით ბორის ნიტრიდის
დიატომური მოდელებელის, განბმოლებული ფენის, ჰექსა-
გონალური, კუბური და ვურტციტისბერი კრისტალელბის
რხევათ ენერგიების ძირითად მდგომარეობაში შეუსუბი-
ლია, როგორცა 0.178, 0.242, 0.266, 0.330 და 0.323 eV/mole,
შესაბამისად.

THE GREENHOUSE EFFECT, CLIMATIC CHANGE AND LONG-TERM TRENDS IN THE IONOSPHERE

K. Tukhashvili, V. Kakulia, V. Kandashvili, K. Otarashvili

ABSTRACT. The new method to study long-term trends in the ionosphere is worked out. Existing absolute and relative methods do not describe real aspect of trends. Data of Moscow, Tbilisi and Vanimo are used to analyze revealing long-term trends by our method, but this is not observed in these data. It is shown that Solar activity in the ionosphere increases with decrease of the Sun's zenith angle and reaches its maximum at noon. The analysis of data on the radio wave absorption in the D region, f_oE and f_oF2 indicate that the role of solar activity decreases with decreasing altitude from the F-region down to D-region, that agrees with opinion of several investigators. In addition the role of solar activity at constant zenith angle ($\cos \chi = 0.2$) increases with decreasing latitude. It is necessary to analysis data of another latitude and longitude to reveal long term trend (if it exists), which is not caused by solar activity.

1. INTRODUCTION

Man's expanding activities reached the level at which their effect is global in nature. The natural systems, i.e. the atmosphere, land and sea as well as life on this planet, are being disturbed. It is well-known that some natural trace gases in the atmosphere, such as carbon dioxide (CO_2), nitrous oxide (N_2O), methane (CH_4) and tropospheric ozone (O_3), have been increasing during the last century. In addition, other gases are being emitted that are not naturally part of the global ecosystem, notably chlorofluoro-carbons. These trace gases absorb and emit radiation and are thus able to influence the Earth's climate. They will be referred to as greenhouse gases.

The reason for concern about climatic effects is the so-called "greenhouse effect" of CO_2.

While CO_2 is transparent to incoming short wave radiation from the Sun, it absorbs outgoing long wave radiation and re-emits this energy in all directions. Therefore, an increase of the atmospheric CO_2 concentration leads to a warming of the Earth's surface and lower atmosphere. In addition, it is becoming increasingly clear that a number of other greenhouse gases in the atmosphere similarly affect the radiation budget. Their concentrations are also changing as a result of natural and human causes. Since increased concentrations of CO_2, as well as of those other greenhouse gases, all lead to a warming of the Earth's surface and lower atmosphere, the estimated climatic effects and further impacts (e.g. on sea level and agriculture) must be considered as a result of combined effects of these potential origins of the warming [1].

The long-term continuous increase of greenhouse gas concentration in the atmosphere and other anthropogenic influences represent serious threat for human civilization. Therefore, it is necessary to determine the long-term trends and changes in the atmosphere–ionosphere system. The observed long-term trends in the 20th century might be, however, influenced by contribution of the Sun's origin, and the process of determination of anthropogenic trends from observational data may be "spoilt" by the 11-year solar cycle. As for the possible solar and geomagnetic activity responsible for part of the observed long-term trends, the two main conclusions are as follows: 1. The role of solar and geomagnetic activity in the observed long-term trends decreases with decreasing altitude from the F-region ionosphere down to the troposphere; 2. In the 20th century the role of solar and geomagnetic activity in the observed long-term trends/changes was decreasing from its beginning towards its end [2].

More pronounced trends have been observed in the middle and upper atmosphere and ionosphere. There is a tendency to attribute these trends solely to the increasing concentration of greenhouse gases in the atmosphere. However, the observed long-term trends in the ionosphere and atmosphere cannot be explained solely by the greenhouse effect. The considerable increase of geomagnetic activity in the 20th century and the increase of solar activity in its first half contribute to trends observed in the 20th century. The existence of the strong 11-year solar cycle can result in the incorrect determination of trends from shorter data series.

The calculation of trends and estimates of long-term changes of anthropogenic origin may be affected by solar and geomagnetic activity basically in two ways: 1. Inappropriate selection of data and/or missing measures to correct for medium-term solar/geomagnetic activity variations, which makes the calculation of trends vulnerable to a substantial effect of the 11-year solar cycle. 2. Long-term changes of solar and geomagnetic activity, which contribute to long-term trends.

Long-term changes of solar activity and/or geomagnetic activity may play an important role in the observed long-term trends, particularly in the ionized component of the atmosphere, in the ionosphere [2].

The data on the radio wave absorption in the D region indicate to some systematic trends which may be considered as a manifestation of a temperature decrease around the mesopause. Analysis of rocket measurements of the electron concentration in the D region reveals strong enough positive trend in the upper D region. Several groups claimed positive trends of the E-layer critical frequency, f_oE. Also negative trends of the ratio of two principal ions in the E region ([NO^+]/[O_2^+]) were found. These trends of three independently registered parameters may be interpreted as an indication to the existence of pronounced trends of dynamical processes at altitudes of the D and E regions. In many publications trends of the F2-layer parameters have been considered. Trends in both, the critical frequency f_oF2 and maximum height $hmF2$, were found. It was also found that the f_oF2 trends depend strongly on geomagnetic latitude and geomagnetic activity. This fact makes it possible to assume that the trends are not a consequence of the «greenhouse» cooling of the upper atmosphere (as has been numerously suggested) but manifest secular changes of geomagnetic activity, which influences F2-layer parameters though ionospheric storms. Trends in ionospheric storm number and intensity have also been claimed. However, even if trends of a geomagnetic origin input considerably into the observed long-term changes of f_oF2 and $hmF2$, there still may be a «geomagnetic» component in these changes manifesting «greenhouse» (or other anthropogenic) trends. The question is still open [3].

As follows from review, it is necessary to exclusion the influence of solar and geomagnetic activity from experimental data for find out of long-term trends, it is necessary to consideration long-term changes of parameter at constant activity.

Studies of the long-term changes (trends) in the parameters of the upper atmosphere and ionosphere became very popular during the recent years [2,4].

There are two different approaches (absolute and relative) to the search of long-term trends. It must be said, that neither absolute nor relative can give real nature of trends. For example, if Bremer [5] had used the formula $\Delta X = X_{th} - X_{exp}$ in place of $\Delta X = X_{exp} - X_{th}$, he would have obtained opposite nature: in place of positive trend he would have received negative one and vice versa. Furthermore there takes place a big error when average X obtains yearly value; therefore it is necessary to point out a root-mean-square-error (σ) at figure. Probably, long-term changes get within error; therefore there is no point in spicing about trends. Some advantages of this method were noted by Danilov [4]. In the same place must be noted that Ruiping Ma [6] does not select the best method for revealing semiannual variations, when averages f_oF2 during 8^h-19^h LT period. For this period average $\cos \chi$ changes very considerably within a seasons (for Chung-Li average $\cos \chi$ is twice more in summer than in winter). It will be better, if Ruiping Ma take out $f_oF2(\cos \chi = \text{const})$.

Critical frequency of layers E and F2 depends on the sun's zenith angle and activity, and so it is necessary to calculate the parameter at constant zenith angle (for example $\cos \chi = 0.2$) and the same activity.

The calculation f_oE at constant zenith angle is possible by well-known formula $f_oE = (f_oE)_o \cos^n \chi$. It is necessary to point out, that as the Earth is spherical $\cos \chi$ will be changed by Chapman's function at sunrise and sunset ($\chi > 75^\circ$). The experiment shows that diurnal variation of f_oE will be better described by second degree polynomial $f_oE = k + bt + at^2$ ($t = LT$), from which it is easy to calculate $f_oE(\cos \chi = \text{const})$ (if we have better calculated t ($\cos \chi = \text{const}$) and time of relaxation — shift of noon maximum of f_oE to evening hours [7]. The $f_oE(\cos \chi = \text{const})$ has seasonal variations of so-called

winter anomaly [8], therefore it is necessary to compute σ when calculating average yearly value.

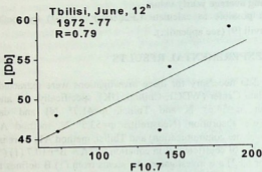It is possible to calculate $f_oF2(\cos \chi = const)$ by method of Tukhashvili [9] (see appendix).

2. EXPERIMENTAL RESULTS

The data necessary for these investigations were extracted from World Data Center (WDC1, Chilton, UK), specifically, f_oE and f_oF2 (Juliusruh, $\varphi=54.6°$ N and Tbilisi, $\varphi=41.7°$ N) and data of radiowave's absorption (Neustrelitz, $\varphi=53.5°$ N, method A3 (G. Entzian, private communication) and Tbilisi, method A1) were used.

Behavior of coefficient B in equation $y = A + B*F10.7$ (1) (where $y = f_oE$ or f_oF2) are investigated. As seems from (1) B defines rate of critical frequency/electron concentration change with increasing of sun's activity. It is found that B increases with decrease of the sun's zenith angle and reaches its peak in the noon.

Fig.1 shows that the role of solar activity decreases with decreasing altitude from the F-region down to the D-region: B decreases from F-region to the E region from 0.034 to 0.006 (Tbilisi) and from 0.018 to 0.0065 (Juliusruh). Correlation coefficient R between line and experimental points decreases from 0.96 (F region) to 0.79 (D region) by data of Tbilisi and 0.92 (F region) to 0.39 (D region) by data Juliusruh and Neustrelitz.

Tbilisi, June, 12^h
1964 - 86
R=0.96

foF2
foF2=3.7+0.034F10.7

foE
foE=2.9+0.006F10.7

143

Tbilisi, June, 12^h
1972 - 77
R=0.79

Juliusruh, June, 12^h
1958 - 90
R=0.92

foF2

foF2=4.08+0.018F10.7

foE

foE=2.6+0.0065F10.7
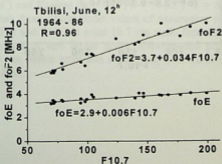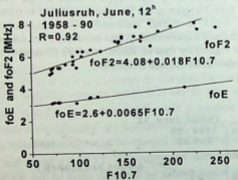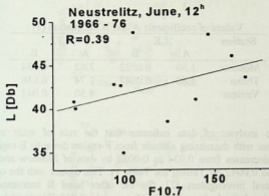
Fig.1 Dependence noon values of critical frequencies of E and F2 layers and radio wave absorption (L) at activity of the Sun by data of Tbilisi and Juliusruh for June

Parameters of ionosphere depend on the sun's zenith angle as well as on the activity, therefore it is necessary make use of parameters at constant zenith angle and activity for calculation of trends.

Fig.2 shows the results obtained by analysis of data of the following points: Moscow ($\varphi = 55.5^0$ $\lambda=37.30^0$), Tbilisi ($\varphi = 42.5^0$; $\lambda = 44.8^0$) and Vanimo ($\varphi = -2.7^0$; $\lambda = 141.3^0$). $Y = A + B*F10.7$ (1) is equation, from which model values of parameters were obtained; $Y = f_0E(f_0F2)$ and F10.7 is solar 10.7 cm radio flux. In Table 1 values of coefficients A and B are given. Experimental points coincide with model one within error and so the long-term trend is not observed by those data.

Table1

Values of coefficients A and B in equation (1)

Station	f_0E		f_0F2	
	A	B	A	B
Moscow	1.96	0.0032	2.62	0.034
Tbilisi	1.88	0.0042	2.74	0.036
Vanimo			4.50	0.041

The analysis of data indicates that the role of solar activity decreases with decreasing altitude from F-region down to E-region (B in (1) decreases from 0.034 to 0.0032 by data of Moscow and from 0.036 to 0.0042 by Tbilisi; see Table 1). This agrees with the opinion of several investigators [2]. On the other hand B increases with decreasing latitude from 0.034 (Moscow) to 0.041 (Vanimo) by f_0F2 and from 0.0032 (Moscow) to 0.0042 (Tbilisi) by f_0E (f_0E data of Vanimo was not enough).

It is possible to reveal f_0E and f_0F2 long-term trends, which are not caused by solar activity (if it exists) by analyzing data for another latitude and longitude.

146
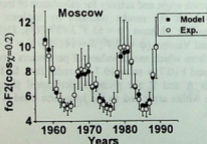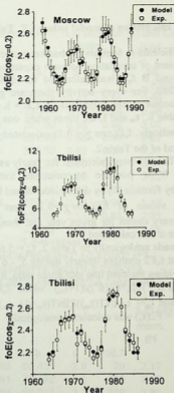
Fig.2. Long-term changes of model values (black points) and experimental ones (white area of circle) of f_0E and f_0F2 at $\cos \chi = 0.2$. Long-term trends are not observed these data – experimental points coincide with model ones within error.

About calculation of model value: f_mE, Table 2.

A and **B** coefficients in formula (1) had been calculated for every hour. R – coefficient of correlation between experimental points and line (1). By **A** and **B** f_mE was calculated for different activities: F10.7=70; 150; 250. For every activity there are given equations, obtained by the second degree polynomial fit $f_mE = k + bt + at^2$ (2) (t = LT), with suitable R. t_m and t_e are times when $\cos \chi$ =0.2 morning and evening respectively. $f_mE(\cos \chi = 0.2)$ calculated by equation (2) are given in the end of the Table 2.

A and **B** coefficients were calculated for yearly average values of $f_mE(\cos \chi = 0.2)$. It is possible to calculate model values of $f_mE(\cos \chi = 0.2)$ by formula (1) by determined **A** and **B**.

Experimental values of $f_mE(\cos \chi = 0.2)$ were calculated by formula (2) for every month for given year and then yearly average value with suitable σ was calculated.

Table 3 was made analogically to Table 2. $t_m = 5.67$ i.e. $5^h < t_m < 6^h$. Let us assume that f_mF2 changes linearly during $5^h - 6^h$ interval. Using the formula of dividing segment line into given ratio, it follows: $f_mF2(t_m)=F1(t_m)=(F1(5^h)+I_m*F1(6^h))/(1+I_m)$ when $f_mF2(\cos \chi = 0.2)= f_mF2(t_m)= F1(t_m)$ and $I_m=(t_m - INT(t_m))/(INT(t_m+1)- t_m)$. Evening value $f_mF2(\cos \chi = 0.2) = F2(t_e)$ was calculated analogically.

Table 2. Values of A, B, R in equation (2) and $f_oE(LT; F10.7)$

Tbilisi, June

tm	te	LT	A	B	R	70	150	250
						F10.7		
						$f_oE(LT; F10.7)$		
5.7	18	7	226.74	0.47	0.91	2.60	2.98	3.45
		8	250.11	0.52	0.94	2.86	3.28	3.79
		9	267.80	0.56	0.92	3.07	3.51	4.07
		10	281.23	0.58	0.88	3.22	3.68	4.26
		11	289.53	0.59	0.86	3.31	3.78	4.38
		12	292.29	0.60	0.85	3.34	3.82	4.43
		13	290.23	0.60	0.85	3.32	3.80	4.40
		14	282.86	0.59	0.87	3.24	3.71	4.30
		15	270.13	0.57	0.90	3.10	3.55	4.12
		16	253.02	0.54	0.93	2.91	3.33	3.87
		17	230.43	0.50	0.94	2.65	3.05	3.55

$$f_oE = k + bt + at^2$$

		R
$f_oE(70) = -85.46434 + 69.43147 \cdot t - 2.87063 \cdot t^2$		0.9999
$f_oE(150) = -91.03963 + 78.19231 \cdot t - 3.3296 \cdot t^2$		0.9999
$f_oE(250) = -104.39767 + 90.23147 \cdot t - 3.71911 \cdot t^2$		0.9999

$f_oE(\cos \chi = 0.2)$

				morn. E1	average (E1+E2)/2
k	b	a	F10.7		
-85	69.431	-2.9	70	2.17	2.20
-91	78.192	-3.2	150	2.50	2.54
-104	90.231	-3.7	250	2.89	2.95
				even. E2	
-85	69.431	-2.9	70	2.24	
-91	78.192	-3.2	150	2.58	
-104	90.231	-3.7	250	3.01	

Table 3. Values of A, B, R in equation (2) and f/f² (LT; F10,7)   Tbilisi   June

	LT	A	B	R	\(f(F10,7; F10,7)\)											
					70	100	130	160	210	260	70	100	130	160	210	260
Im= 5,67	0	27	0,27	0,94												
Im= 18,33	1	25	0,24	0,93	54	63	68	76	85	86						
Im= 2,00	2	0	0,3	0,96	41	50	56	67	75	83	85					
Im= 0,50	3	16	0,31	0,95	34	50	54	63	71	77			F1			
	4	14	0,31	0,97	30	41	54	63	71	82		45	54	63	73	81
	5	20	0,28	0,46	34	53	60	71	82	85						
	6	28	0,28	0,94	40	55	63	72	84	85						
	7	32	0,29	0,94	47	60	70	78	88	91						
	8	34	0,29	0,95	51	65	72	82	92	102	118					
	9	32	0,33	0,95	52	60	73	82	90	98	102		(F1+F2)/2			
	10	36	0,32	0,94	53	60	70	80	86	96	106	119	66	74	84	93	81	89	90
	11	36	0,33	0,94	52	60	70	80	86	97	107	121					
	12	36	0,34	0,96	54	60	69	78	86	95	105						
	13	33	0,36	0,96	54	60	69	77	88	98						
	14	33	0,36	0,98	50	58	66	74	84	95						
	15	31	0,36	0,95	46	53	63	72	80	88	102					
	16	31	0,34	0,97	42	52	61	70	78	88	100		F2			
	17	29	0,33	0,92	37	46	57	66	78	88						
	18	23	0,33	0,92	32	42	52	63	71	79		55	64	66	74	80
	19	21	0,3	0,96	31	39	50	63	72	80						
	20	23	0,28	0,92	33	45	51	62	69	78						
	21	26	0,28	0,93	34	50	58	65	74	81						
	22	24	0,22	0,91	44	53	60	69	77	84						
	23	20	0,25	0,9	48	58	64	74	85	87						
	24	23	0,27	0,9	52	60	66	75	85	86						

REFERENCES

1. B. Bolin, J Jager and B.R. Doos, The greenhouse effect, climatic change, and ecosystems. SCOPE-29- The Greenhouse effect, Climatic change, and Ecosystems.By the UNEP/WMO/ICSU Conference on the assessment of the role of carbon dioxide and of other greenhouse gases in climate variations and associated impacts (Villach, Austria, October 1985).

2. J. Lastovicka. Journal of Atmospheric and Solar-Terrestrial Physics **67**, 2005, 83.

3. A.D. Danilov. Advances in Space Research. **28**, 2001, 987.

4. A.D. Danilov. Physics and Chemistry of the Earth. **27**, 2002, 579.

5. J. Bremer. Annales Geophysicae. **16**, 1998, 986.

6. Ruiping Ma, Jiyao Xu and Huaizhe Liao. Journal of Atmospheric and Solar-Terrestrial Physics **65**, 2003, 47.

7. E. V. Appleton. J. Atm. Terr. Phys. **3**, 1953, 282.

8. B. B. Kandashvili, M. I. Tevdorashvili, K. I. Tukhashvili, Geomagnetism I Aeronomia. **3**, 1985, 499 (Russian).

9. K. Tukhashvili. Journal of the Georgian Physical society **3**, 1996, 74.

Tbilisi State University

ქ. ტუხაშვილი, ვ. კაკულია, ვ. ყანდაშვილი,
ა. ოთარაშვილი

სათბურის ეფექტი, კლიმატის ცვლილება და
გრძელვადიანი ტენდენციები იონოსფეროში

დასკვნა

შემუშავებულია იონოსფერში გრძელვადიანი ტენდენცი-
ციის შესწავლის ახალი მეთოდი. არსებული აპსოლუტური
და ფარდობითი მეთოდები ვერ ასახავენ რეალურ სურათს.

ჩვენ მეორიდან ანალიზისათვის გამოვყენებულია მოს‑
ვის, თბილისისა და ქოშის მონაცემები. ამ შემთხვევაში
გრძელდებიდან ტენდენცია არ დაიკვირვება. ნაჩვენებია,
რომ მზის აქტივობის ცუველურია იზრდება ზენიტური
კუთხის შემცირებასთან ერთად, აღწევს რა მაქსიმუმს
შუადღესთან. D არეში რადიოტალღების შთანთქმის, f_E და
f_sF2 მონაცემების ანალიზით ნაჩვენებია, რომ მზის
აქტივობის როლი მცირდება სიმაღლის შემცირებასთან
ერთად F არედან D არემდე, რაც თანხმდება ხხა ჭცელე‑
ვარია ახრს. ნაჩვენებია, აგრეთვე, რომ მზის აქტივობის
როლი მუდმივ ზენიტურ კუთხეზე (cos χ = 0.2) იზრდება ზა‑
ნრალთ შემცირებასთან ერთად. საჭირო სხვადასხვა ვა‑
ნრალის და გრძელის მონაცემთან ანალიზი, რათა გამა‑
მცნელდეს გრძელდებიდან ტენდენცია, რომდელიც არ არის
გამოწვეული მზის აქტივობით (თუ იგი არსებობს).

OSCILLATION SHAPE OF THE HOPPING DOMAIN CURRENT DEPENDING ON THE BIAS VOLTAGE

D. Aladashvili, Z. Adamia, A. Adamia

ABSTRACT. The dependence of the shape of current oscillations observed in the hopping conductivity region in a weakly compensated p-Si on the supply voltage applied to the sample is established. With increasing bias voltage the current pulse shape to form a hopping domain changes significantly. The change in the shape is ascribed to voltage redistribution in corresponding regions in the bulk of the crystal.

In [1] the observation of a new type of current instability in the hopping conductivity region was reported. The phenomenon manifested itself in a periodic current increase and decrease observed in the external electric circuit. The current oscillations were observed in samples with a sublinear current-voltage characteristic in the portion with a negative differential resistance. A slight decrease in the conductivity with increasing field was obtained experimentally in p-Ge [2]. Earlier in [3] a possibility of exponential decrease in the hopping conductivity with increasing field had been predicted. In the work a formation of dead ends in the infinite cluster (IC) of acceptors responsible both for electron trapping in high electric fields and for hopping transport was considered. The length of these ends-traps was equal to that of the characteristic grid period. A statistical current-voltage characteristic with decreasing current was computer-modeled [4] in assumption of an ideally homogeneous sample. In this case typical traps captured electrons in any part of the sample with equal probability. And the real sample always has an inhomogeneity of one kind or another. Further experimental investigations showed that current oscillations observed in the semiconductor were due to formation and motion of a hopping domain in the bulk of the sample [5]. A crystal "predisposed" to negative differential resistance passes into this state in the portion where its resistance is somewhat higher.

Precisely from this portion (cathode) the formation and motion of a volume charge similar to Gunn diode takes place [6].

Let us consider the obtained experimental data. Current oscillations were observed in p-Si samples with the intrinsic impurity concentration of $(5-7.5) \cdot 10^{16}$ cm^{-3} and compensation degree of $(5 \cdot 10^{-3}$-$4 \cdot 10^{-5})$. The generation took place at a certain critical bias voltage U_r. A voltage generator was switched to the sample in the pulse mode, which is necessary for synchronization of the oscillograph's work. The voltage pulse width could be controlled in the broad range. The current meter was a specially designed differential amplifier. Part of the signal was applied to the protective screen of triaxial cable from the amplifier output due to the feedback. Here capacitance leakages were neutralized thus increasing the frequency properties of the current meter. The form of the varying current signal was observed on the oscillograph and recorded on the photographic film. The process of domain formation depends on many conditions. In particular, on the type of contacts and on the conditions imposed by the external circuit.

1(a)   1(b)

154
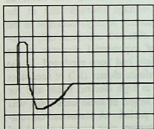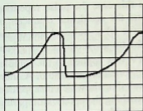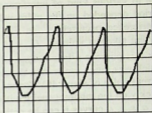
Fig.1. Current pulse shape versus bias voltage U_s near the
threshold voltage U_t of hopping domain formation.

(a) - Trigger mode, (b) - U_s =31.1V, (b) - U_s =38.4V,
(c) - U_s =39V, (d) - U_s =40V. Scanning time t (horizontal
scale) for (a,b,c) - t = 50 ms/part, for (d) - t = 100 ms/part.
Current I (vertical scale) for (a) -1 nA, for (b,c,d) - 0.5 nA

Let us consider the change in the current pulse shape in the sample
with $N_a = 7.3 \cdot 10^{16}$ cm^{-3} and $K \approx 2 \cdot 10^{-4}$ at the bias voltage U_s close
to the threshold of high field region formation. In this case the pulse
width was 3-4 of the transit time T. The investigations were carried
out at temperature 10K. In Fig.1, b, c, d a time dependence of the
current shape is given for three fixed bias voltages within 38.4-41V. In
this region the time-averaged current increases with increasing
voltage. Here on the cathode there occurs a triangle-shaped domain
moving towards the anode [7]. The formation of the next domain is
preceded by a certain expectation time decreasing with the bias
increase. At the bias voltage equal to the domain formation threshold
the differential mobility μ_d = dv/dE = 0 (here v is the carrier drift
velocity). In our case the Kroemer criterion is fulfilled [8]. Therefore
when the bias field even slightly exceeds the threshold one, i.e. at a
low $|\mu_d|$ the domain can be formed. And the higher is $|\mu_d|$, the
quicker it is formed. At weak circuit screening the domain was formed

due to various kind of interference; in this case the pulse repetition period depended on the pulse value and the accidental character of interference occurrence. In Fig.1 (curve a) a pulse shape of the current taken at voltages $U_{ts} < U_t$ in the trigger mode is also given. For this purpose a bias voltage of 31.1V was applied to the sample, which was much lower than the domain formation threshold. A short current pulse of about 40V formed a weak domain which disappeared quickly on the inhomogeneity without reaching the anode. Comparing the a, s, c, d curves it can be noticed that with an increase in bias the domain transit time rises from 150 ms (for a trigger mode) to 320 ms. It can be explained as follows.

(a)

(b)

(c)

(d)
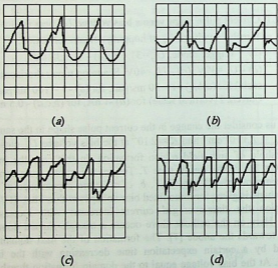
Fig.2. Current pulse curve at high bias voltages. (a) - $U_s = 45V$, (b) - $U_s = 47V$, (c) - $U_s = 49V$, (d) - $U_s = 50V$. The scanning time (horizontal scale) - 100 ms/part. Current I (vertical scale) - 0.5 nA.

It is clear from Fig.1 that the time dependence of the current reproduces the conductivity profile in a certain scale in the region of inhomogeneities. With increasing bias the domain velocity does not change significantly. One should also take into account that the observed inhomogeneity (the relief of the lower part of the current pulse) in the sample is due to a monotonous rise in the conductivity in the portion of approaching the anode. Therefore with increasing bias a stronger domain passes a longer distance to the anode. The best-developed is the domain shown in Fig.1 (d). Knowing its velocity $V_c \approx 0.25$ cm^{-3} and the size $d \approx 150$ µm, a characteristic time of its travel to the anode can be estimated $\tau_a \approx 60$ ms. It should be mentioned that this process is actually much more complex. For example, the action of the Poole-Frenkel hopping effect accompanying the domain motion should probably be taken into account [9].

With a further increase in the bias voltage in the sample a new domain may appear on the cathode simultaneously with the motion of the domain to the anode. Here the constant voltage applied to the sample is redistributed between the domain moving towards the anode and the domains being formed. At the same time the maximum value of the generating current remains unchanged. During the motion of the high field region towards the anode the voltage excess on the cathode increases for the time longer than that of a space charge formation. Therefore this voltage will form one domain in the sample. Here, taking into consideration the tendency in development of the current pulse shape, one can assume that at a high bias voltage the domain becomes wider and takes a trapezoidal shape. In our case the complex relief of the current pulse can be explained by inhomogeneities in the short path of the domain as well as by the mutual effect of the domain moving to the anode and those being formed.

Voltage pulses with the width equal to the domain transit time were also applied to the sample. The front pulse rise of the bias voltage took place for the time much shorter than the Maxwell time $\tau_{md} = \varepsilon / 4\pi q \mu_d n_0$ of formation of a volume charge (where ε is the substance permittivity, q is the charge, μ_d is the differential mobility, n_0 is the current concentration). In this case the current pulse shape

157

observed was different from that of current oscillations taken at a constant voltage, source.

In conclusion the following can be said: At the sample voltage close to the threshold of formation of current oscillations there occurs a situation when the first domain is formed. In this case conditions are created for main diode transit regimes – the quenching regime and the lagging regime similar to the transit regime of a Gunn diode. With sufficiently high bias voltage the conditions of voltage redistribution between the domain moving towards the anode and the next domain being formed on the cathode are realized. The formation of adjustable inhomogeneities in the sample makes it possible to control the current with time, which presents a practical interest in terms of creation of analogous devices working at low temperatures.

REFERENCES

1. D.I.Aladashvili, Z.A.Adamia, K.G.Lavdovskii, E.I.Levin, and B.I.Shklovskii, JETP Lett. **47**, 1988, 390.
2. A.G. Zabrodskii, I.S. Shlimak, Soviet Phys. Semicond. **11**, 1977, 736.
3. V.I.Nguyen, B.I.Shklovskii, Solid State Commun. **38**, 1981, 99.
4. E.I.Levin, V.I.Nguyen, B.I.Shklovskii, Sov. Phys. Semicond. **16**, 1982, 815.
5. D.I.Aladashvili, Z.A.Adamia, and E.L.Tzakadze, Solid State Commun. **101**, 1997, 183.
6. J. B. Gunn, IBM JI Res. Dev., **8**, 1964, 4.
7. D.I.Aladashvili, Z.A.Adamia, Philos. Mag. **B 81**, 2001, 1031.
8. H.Kroemer, Proc. IEEE, **52 (12)**, 1964, 1736 .
9. D.I. Aladashvili, Z.A. Adamia, K.G. Lavdovskii, E.I. Levin, and B.I. Shklovskii. Fizika Tekhn Poluprovodn. **23**, 1989, 2, (Russian).

Tbilisi State University

დ. ალადაშვილი, ზ. ადამია, ა. ადამია

ნახტომისებური დონეების დენის რხევების ფორმის დამოკიდებულება წანაცვლების ძაბვის სიდიდეზე

დასკვნა

დადგენილია დენის რხევების ფორმის დამოკიდებულება ნიმუშზე მოდებულ ძაბვაზე სუსტად კომპენსირებულ p-Si-ის ნახტომისებური გამტარობის არეში. წანაცვლების ძაბვის გაზრდით ნახტომისებური დონეების დენის რხევების ფორმა საგრძნობლად იცვლება, რაც აიხსნება ძაბვის გადანაწილებით კრისტალის მოცულობის შესაბამის არეებში.

LONG-TERM TRENDS IN THE IONOSPHERE (METHOD AND SOME RESULTS)

K. Tukhashvili, V. Kandashvili, J. Mdinaradze, K. Otarashvili, M. Miminoshvili

ABSTRACT. A new method of investigation of long-term trends in the ionosphere is introduced. Using of ionosphere parameters at constant zenith angle and same activity makes the long-term trends independent of the solar activity and zenith angle. This method opposes a statement about long-term trends of f_oE and f_oF2-parameters observed by data of Moscow and Tbilisi. The analysis of data by this method for several latitudes and longitudes asserts or disclaims (that is more probable) existence of the long-term trends not caused by the solar activity in the ionosphere.

1. INTRODUCTION

Studies of long-term trends of the parameters of upper atmosphere and ionosphere became very popular during recent years [1,2]. There are two different approaches (absolute and relative) to investigation of long-term trends. Absolute values of f_oF2 and $hmF2$ trends are looked for in the absolute method. The principal formulae are given in [3]. The theoretical (model) value of the parameter X (it may be f_oF2, $hmF2$, f_oF1 etc.) is obtained as a result of the data regression in terms of a solar activity index [3]:

$$X(th) = A + B R$$

or

$$X(th) = A + B R + C R^2.$$

The author tried also to include into the regression the magnetic activity index

$$X(th) = A + BR + C Ap$$

but found no significant effect in the trends.

Then the difference between the observed $X(\exp)$ and modeled $X(\text{th})$ values is found:

$$\Delta X = X(\exp) - X(\text{th})$$

The ΔX values were then presented versus the years considered:

$$\Delta X = a + bY,$$

where Y is a year, and the slope b was taken as an absolute trend (in MHz per year for f_oF2 and in km per year for $hmF2$).

Having analyzed the data of 31 ionospheric stations in the European region, there were obtained f_oF2 trends of various signs and values [4]. It was detected no dependence of the trends on latitude, but some longitudinal effect, the trends to the west from $\lambda = 30$ E being mostly negative and the trends to the west from $\lambda = 30$ E being mostly positive.

Unfortunately, the absolute method of trend determination applied by [4] has some disadvantages which may cause negative results on the f_oF2 and $hmF2$ trends finally obtained [1]

[5,6] proposed a method of long-term trend determination different from that used by other authors.

The principal formula is:

$$\delta X = [X(\text{obs}) - X(\text{mod})]/X(\text{mod}),$$

where X stands for f_oF2 or $hmF2$ and the third-degree polynomial in terms of the sunspot number R is used as a model.

It must be mentioned that neither of them allow finding the real character of trends. Furthermore, error of estimation of yearly average of X is rather considerable. Therefore, it is necessary to display every point of the plot with its root-mean-square-error (σ). If long-term changes of the parameters fall within the error limits, revealing of trends is not possible. It should be also pointed out that selection of the method in work [7] in order to reveal semiannual variations of average of f_oF2 within 08:00-19:00 LT was not quite accurate.

Average of $\cos \chi$ for this period of day changes very considerably by seasons (within those hours average of $\cos \chi$ is twice as much during summer than in winter time in Chung-Li). It would be better, if Ruiping Ma used $F2(\cos \chi = \text{const})$.

2. EXPERIMENTAL RESULTS

The data necessary for these investigations were extracted from World Data Center WDC1, Chilton, UK. Data of different latitudes are used.

Critical frequencies of E and $F2$ (f_oE and f_oF2) layers depend on the zenith angle and activity of the sun. So, it is necessary to calculate the parameters at constant zenith angle (for example $\cos \chi = 0.2$) and for the same activity.

The calculation of f_oE at constant zenith angle is possible by means of a well-known formula

$$f_oE = (f_oE)_o \cos^n \chi \qquad (1)$$

It is necessary to point out that as the Earth is spherical, $\cos \chi$ must be replaced by Chapman's function at sunrise and sunset ($\chi \leq 75^0$). Experiments show that second degree polynomial

$$f_oE = k + bt + at^2 \qquad (2)$$

($t = \text{LT}$) describes diurnal variation of f_oE better than (1). It is easy to calculate $f_oE(\cos \chi = \text{const})$ (if we have calculated t ($\cos \chi = \text{const}$) in advance) and relaxation time – shift of noon maximum of f_oE towards evening hours [8]. The $f_oE(\cos \chi = \text{const})$ is characterized by seasonal variations – so-called winter anomaly [9,10]. Therefore, it is necessary to compute σ when calculating average yearly value of X. In Table 1, t_m and t_e are points, when $\cos \chi = 0.2$ in the morning and in

Table 1.

Values of A, B, R in equation (2) and f_eE(LT; F10.7)

t_m	t_e	LT	Tbilisi			June F10.7		
			A	B	R	70	150	250
						f_eE(LT; F10.7)		
5.7	18	7	226.74	0.47	0.91	2.60	2.98	3.45
		8	250.11	0.52	0.94	2.86	3.28	3.79
		9	267.80	0.56	0.92	3.07	3.51	4.07
		10	281.23	0.58	0.88	3.22	3.68	4.26
		11	289.53	0.59	0.86	3.31	3.78	4.38
		12	292.29	0.60	0.85	3.34	3.82	4.43
		13	290.23	0.60	0.85	3.32	3.80	4.40
		14	282.86	0.59	0.87	3.24	3.71	4.30
		15	270.13	0.57	0.90	3.10	3.55	4.12
		16	253.02	0.54	0.93	2.91	3.33	3.87
		17	230.43	0.50	0.94	2.65	3.05	3.55

$f_eE = k + bt + at^2$

		R
$f_eE(70) = -85.46434 + 69.43147 \cdot t - 2.87063 \cdot t^2$	0.9999	
$f_eE(150) = -91.03963 + 78.19231 \cdot t - 3.2296 \cdot t^2$	0.9999	
$f_eE(250) = -104.39767 + 90.23147 \cdot t - 3.71911 \cdot t^2$	0.9999	

$f_eE(\cos \chi = 0.2)$

				morning	average
k	b	a	F10.7	E1	(E1+E2)/2
-85	69.431	-2.9	70	2.17	2.20
-91	78.192	-3.2	150	2.50	2.54
-104	90.231	-3.7	250	2.89	2.95
				evening	
				E2	
-85	69.431	-2.9	70	2.24	
-91	78.192	-3.2	150	2.58	
-104	90.231	-3.7	250	3.01	

the evening correspondingly. Data of Tbilisi (June 1964-86) are used. Hourly data from 7^h till 17^h were interpreted by formula

$$y = A + B \cdot F10.7 \qquad (3)$$

($y = f_oE$, F10.7 is the solar radio flux at 10.7 cm in units 10^{-22} W·m^{-2}) and A and B were calculated. There are given correlation coefficient R between line (3) and experimental points in the Table. $f_oE(LT)$ calculated by coefficients A and B for several F10.7 (F10.7 =70; 150 and 250) are given in the last three columns. Diurnal variations of f_oE are described by second-degree polynomial (2) and corresponding equation with correlation coefficient R between curve (2) and experimental points are also given in Table. Substitution of t_m and t_e for t gives afternoon values (E1) and forenoon values (E2) of $f_oE(\cos\chi = 0.2)$ correspondingly. There are given the values of $f_oE(\cos\chi = 0.2) = (E1 + E2)/2$ for June at each activity in the Table. It will be calculated for the rest of the months analogically. After that, early mean value of $f_oE(\cos\chi = 0.2)$ for several activities will be calculated and the line $f_oE(\cos\chi = 0.2) = A_{jh} + B_{jh} \cdot F10.7$ will be drawn through the points corresponding the calculated early mean values of $f_oE(\cos\chi = 0.2)$. Definite A_{jh} and B_{jh} enable to calculate model values of $f_oE(\cos\chi = 0.2)$ for any activity.

Experimental values of $f_oE(\cos\chi = 0.2)$ of every month for given year were calculated by formula (2) and then its yearly average with corresponding σ was evaluated.

Calculation of $f_oF2(\cos\chi = \text{const})$ is possible by method of [11] (see Table 2). As in the previous case, Tbilisi data of June 1964-86 are used here. It is drawn a line according (3) through the points that correspond to hourly data of June for every year and calculated A and B coefficients with correlation coefficients R given in the Table 3. Values of $f_oF2(LT)$ calculated by formula (3) for several F10.7 are given in Ttoo. t_m and t_e are points, when $\cos\chi = 0.2$ in the morning and in the evening correspondingly. $t_m = 5.67$ follows $5^h < t_m < 6^h$; Assumption, that f_oF2 changes linearly within $5^h - 6^h$

Table 2.
Values of A, B, R in equation (2) and $f_v/2$(LT; F10.7)

					Tbilisi						June							
					F(10.7)							F(10.7)						
					70	100	130	150	180	210	250	70	100	130	150	180	210	250
	LT	A	B	R	(F2)(LT; F10.7)							(F2)(LT; F10.7)						
tm= 5.67	0	27	0.27	0.94			66	63	76	85	96							
te= 18.33	1	25	0.28	0.94		53	61	67	75	83	95							
tm= 2.00	2		03	0.96	41	50	59	64	74	85	93							
te= 0.50	3	16	0.35	0.98	38	47	56	63	72	81	93					F1		
	4	14	0.31	0.97	35	44	54	60	69	78	90							
	5	20	0.28	0.95	40	49	57	62	71	79	89	45	64	62	68	76	85	96
	6	28	0.28	0.94	48	56	65	71	79	88	99							
	7	32	0.29	0.94		52	62	75	82	93	105							
	8	29	0.29	0.95	54	63	74	78	87	96	108							
	9	32	0.33	0.96		58	65	82	92	102	115							

165

Table 2 (To be cont.)

Values of A, B, R in equation (2) and ζF2(LT; F10.7)

					Tbilisi	June											
							F(10.7)						F(10.7)				
LT	A	B	R	ζF2(LT; F10.7)	70	100	130	170	210	250		70	100	130	150	210	250
10	36	0.32	0.94	59	68	78	84	93	103	115	(F1+F2)/2 119	52	60	68	73	81	89 / 99
11	36	0.33	0.94	60	70	80	86	96	106	119							
12	36	0.34	0.96	60	70	80	87	98	109	123							
13	33	0.36	0.96	58	69	80	87	98	109	123							
14	31	0.36	0.95	56	68	78	85	96	76	81	115						
15	31	0.34	0.97	56	66	75	81	91	101	115							
16	29	0.33	0.97	52	62	72	78	88	98	111							
17	31	0.3	0.96	52	61	70	76	83	94	106							
18	34	0.28	0.95	54	62	70	76	83		104	F2						
19	42	0.25	0.9	55	57	65	73	79	86	94	106	72	78	86	93	102	
20	49	0.19	0.87	63	68	74	78	88	93								
21	44	0.22	0.91	59	66	73	77	84	90	99							
22	43	0.2	0.91	57	63	69	74	80	86	94							
23	35	0.23	0.92	52	59	68	75	77	84	93							

interval gives negligible error. Using the formula of dividing segment line into given ratio, gives:

$$f_oF2(t_m) = F1 = (F1(5^h) + I_m \cdot F1(6^h))/(1 + I_m),$$

where $I_m = (t_m - \text{INT}(t_m))/(\text{INT}(t_m+1) - t_m)$. Evening value $f_oF2(\cos\chi = 0.2) = F2$ was calculated analogically.

Values of $f_oF2(\cos\chi = 0.2) = (F1 + F2)/2$ will be defined for every month and then yearly average values for several activities will be calculated. It is possible to describe this data by line $f_oF2(\cos\chi = 0.2) = A_{th} + B_{th}$. F10.7 and calculate A_{th} and B_{th}, that enables to calculate model values of $f_oF2(\cos\chi = 0.2)$ for any activity.

Experimental values of $f_oF2(\cos\chi = 0.2)$ will be found for each month every year by using t_m and t_e as it was described above. Then yearly average value will be evaluated with corresponding σ.

Fig.1 shows the dependences by analysis of the following data: Moscow ($\varphi = 55.5^0$; $\lambda = 37.30^0$ 1958-1990), Tbilisi ($\varphi = 42.5^0$; $\lambda = 44.8^0$, 1964-1986) and Vanimo ($\varphi = -2.7^0$; $\lambda = 141.3^0$ 1967-1990).
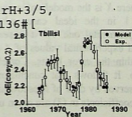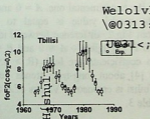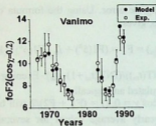
Fig.1. Long-term changes of model values (black circles) and experimental ones (white circles) of f_oE and f_oF2 at $\cos \chi = 0.2$. Long-term trends are not revealed by this data – estimation errors of the experimental points cover the model ones

Model values of both $f_oF2(\cos \chi = 0.2)$ and $f_oE(\cos \chi = 0.2)$ are calculated for the activity, which corresponds to their experimental values. Fig.1 shows, that the parameters depend on the sun's activity – they reach their maximum in the period of an active sun and the minimum – in the period of a quiet sun. Experimental values are given with corresponding σ. As it is obvious from Fig.1, experimental values fall within the error limits of the model points and so the long-term trends were not observed by these data. Fig.2 shows more clearly that the long-term trends are not observed by these data. Dependence between theoretical (model) and experimental values of parameters (f_oE or f_oF2 at $\cos \chi = 0.2$) are described by equation: $Y = A + B X$ where X is the model value and Y – the experimental one. $A = 0$ and $B = 1$ in the ideal case, when the model value is equal to the experimental one. As it is seen from Fig.2, difference between ideal and experimental values of A and B is negligible – $A \approx 0$ and $B \approx 1$ within the error limits. Correlation coefficients are high ($R > 0.97$) too. It follows that conclusion to [4] about long-term trends being observed by data of Moscow and Tbilisi is erroneous. Values of A and B coefficients in (3) are given in Table 3.
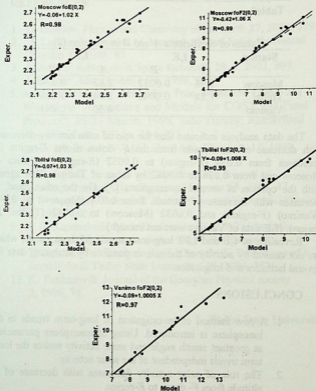
Fig.2. Dependence between theoretical(model) and experimental values of f$_z$E and f$_z$F2 at $\cos \chi = 0.2$. R is correlation coefficient between $Y = A + BX$ line and experimental points.

Table 3.

Station	f_oE		f_oF2	
	A	B	A	B
Moscow	1.96	0.0032	2.62	0.034
Tbilisi	1.88	0.0042	2.74	0.036
Vanimo			4.50	0.041

The data analysis indicates that the role of solar activity decreases with decrease of an altitude from the $F-$ down to the $E-$region (B decreases from 0.034 (F-region) to 0.0032 (E-region) by data of Moscow and from 0.036 to 0.0042 by those of Tbilisi). This agrees with the opinion of several investigators [2]. On the other hand, B increases with decrease of latitude from 0.034 (Moscow) to 0.041 (Vanimo) (F-region) and 0.0032 (Moscow) to 0.0042 (Tbilisi, $E-$region). (f_oE data of Vanimo were not enough).

Revealing of f_oE and f_oF2 long-term trends (if those exist), which are not caused by activity of the sun, is possible by analyzing data for several latitudes and longitudes.

CONCLUSIONS

1. A new method of investigation of long-term trends in the ionosphere is introduced. Using of ionosphere parameters at constant zenith angle and same activity makes the long-term trends independent of the solar activity.

2. The role of solar activity decreases with decrease of an altitude from $F-$ down to $E-$region

3. The role of solar activity at constant zenith angle ($\cos \chi = 0.2$) increases with decrease of latitude.

4. Result, obtained by this method, opposes a statement about the long-term trends of f_oE and f_oF2 parameters being observed by data of Moscow and Tbilisi [4]. The analysis of data by this method for several latitudes and longitudes asserts or disclaims (that is more probable) existence of the long-term trends in the ionosphere.

REFERENCES

1. D. Danilov. Physics and Chemistry of the Earth 27, 2002, 579.
2. J. Lastovicka. Journal of Atmospheric and Solar-Terrestrial Physics 67, 2005, 83.
3. J. Bremer. Advances in Space Research, 28, 7, 2001, 997.
4. J. Bremer. Ann. Geophys. 16, 1998, 986.
5. A. D. Danilov, A. V. Mikhailov. Proc. of the 2nd COST 251 Workshop "Algorithms and Models for COST 251 Final Product", 30-31 March, 1998, Side Turkey, Rutherford Appleton Lab., UK, p. 114-121.
6. A. D. Danilov, A. V. Mikhailov. Ann. Geophys. 17, 1999, 1239.
7. Ruiping Ma, Jiyao Xu and Huaizhe Liao. Journal of Atmospheric and Solar-Terrestrial Physics 65, 2003, 47.
8. E. V. Appleton. Journal of Atmospheric and Terrestrial Physics 3, 1953, 282.
9. B. B. Kandashvili, M. I. Tevdorashvili, K. I. Tukhashvili. Geomagnetism I Aeronomia 3, 1985, 499, (Russian).
10. Tukhashvili, V. Kandashvili, K. Otarashvili. Procedings of I. Javakhishvili Tbilisi State University, 39, 2004, 182.
11. K. Tukhashvili. Journal of the Georgian Physical society 3, 1996, 74.

Tbilisi State University

171

ქ. ტუხაშვილი, ვ. ყანდაშვილი, ჯ. მგებრაძე,
კ. ოთარაშვილი, მ. მიმინოშვილი

გრძელვადიანი ტენდენციები იონოსფეროში
(მეთოდი და ზოგიერთი შედეგი)

დასკვნა

შემუშავებულია იონოსფეროში გრძელვადიანი ტენდენ-
ციების კვლევის ახალი მეთოდი. მუდმივი ზენიტური კუ-
თხის და აქტიობის შესაბამისი პარამეტრების გამოყენება
გრძელვადიან ტენდენციის ამოასუფულებს მზის აქტიო-
ბის და ზენიტური კუთხის ცვლილების გავლენისაგან. ამ
მეთოდით მიღებული შედეგი ეწინააღმდეგება იმ შეხედუ-
ლებას, თითქოს მოსკოვის და თბილისის მონაცემებით დად-
გკურდება f_0E და f_0F2 პარამეტრების გრძელვადიანი ტენდენ-
ცია. სხვადასხვა განცდების და გრძელვადიანი მონაცემების
ანალიზმა დაამასტურებინ ან ურაყოფს (რაც უფრო მოსა-
ლოდნელია) იმ გრძელვადიანი ტენდენციის არსებობას,
რომელიც არ არის გამოწვეული მზის აქტიობით.

POSITRON ANNIHILATION ENERGY AND LIFETIME SPECTROSCOPY STUDIES ON STAINLESS STEEL 316L AND STEEL 9CR1MO

L.Chelidze[*], D.P. Wells[**]

ABSTRACT. Studies of Positron Annihilation Energy and Lifetime Spectroscopies (PAES and PALS, respectively) on radiation-damaged specimens of stainless steel 316L and steel 9Cr1Mo have been performed. Results for S, W, and T parameters of the Doppler broadened 511keV annihilation line as well as the positron lifetime and trapping intensities have been obtained. Dependence of the characteristic T parameter, positron lifetime and trapping intensity on the dose delivered to specimens was in agreement with what was expected.

INTRODUCTION

The interaction of positrons with matter is widely used to study material properties. It was developed in the early 50s and has matured quickly since then [1]. The reason is that positrons can provide exclusive information about the configuration and properties of materials at the atomic level.

The properties of inhomogeneities (or defects) within material are different from that in the rest of material. Defects are central to any consideration of material characteristics. They determine various material properties. PAES and PALS, which are non-destructive material testing techniques, can be used to verify both the density and size of defects in the material. Therefore these techniques can be used for obtaining essential information about the materials of industrial interest and not only about them [2].

Conservative methods exploit different types of positron sources such as ^{22}Na, or positrons from pair-production. External positron sources are used when studying thin specimens, however, pair-production is the only way to study thick samples [3,4]. Another method is to create a positron source within the material of interest via

nuclear reactions. This was the case in our experiments. The specimens of investigation all contained ^{22}Na positron source via the nuclear separation reaction during the irradiation.

METHODS

The specimens of investigation were irradiated at Los Alamos National Laboratory with 700MeV protons. Doses delivered to them were from 1.02dpa to 10.3dpa. Here dpa stands for displacements per atom and indicates how many times in average has an individual atom displaced from its original position.

The samples of interest were stainless steel 316L and steel 9Cr1Mo. Table 1 shows the chemical composition of the steels mentioned.

Table 1. Chemical composition of stainless steel 316L and steel 9Cr1Mo

Stainless Steel 316L		Steel 9Cr1Mo	
Chemical Element	% comp.	Chemical Element	% comp.
Iron (Fe)	Balance	Iron (Fe)	Balance
Chromium (Cr)	16 – 18	Chromium (Cr)	9
Nickel (Ni)	12 – 14	Molybdenum (Mo)	1
Molybdenum (Mo)	≤ 2.5	Manganese (Mn)	≤ 0.5
Manganese (Mn)	≤ 1.5	Carbon (C)	≤ 0.12
Carbon (C)	≤ 0.02		

We exploited a typical PAES and PALS experimental setups in the research conducted using high energy resolution germanium detector in the energy spectroscopy and fast scintillator detectors in the lifetime spectroscopy.

Figure 1 represents a simplified scheme of the experimental setup used in PAES. The term *source-sample* indicates that the sample of interest had a positron source in it. The source-sample was set in front of the *High Purity Germanium Detector*, which has an excellent energy resolution. The detector measured the energy of the gammas emitted by the source. The signal from the detector was amplified using the *Preamplifier* and *Spectroscopy Amplifier*. Then it was sent

to an *Analog to Digital Converter* (ADC). We took two signals, unipolar and bipolar from the spectroscopy amplifier, since one of
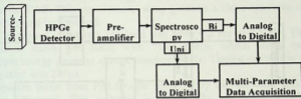
Fig.1. Experimental Setup for PAES

them gives better resolution. When analysing data, we used spectra from the bipolar signal, since it had slightly better resolution compared to the other one. The final spectra were taken and partially analyzed by the *Multi-Parameter Data Acquisition System*. The 511 keV line seen in spectra was the line of interest for us. Not surprisingly it was always wider than the resolution of the detector.

The typical resolution obtained in all PAES experiments was 1.1-1.2keV at 356keV. The full width at half max of the 511 keV lines in the samples analyzed varied from 2.8 keV to 3.4 keV. The background to signal ratio in these experiments was ~1.5%. Typical counting rates were ≈ 2 kHz.

Final analysis of data was performed using the program *STW_PPandACT 2005*, which gives the values of S, W and T parameters of the Doppler broadened 511keV annihilation lines.

Figure 2 shows an experimental setup we used for PALS. We had two BaF_2 detectors coupled with *photomultiplier tubes*. The signals from PMT-s were sent to *Constant Fraction Discriminators* (CFD). Then, one of the signals was delayed, using the *Delay* electronic module. Then they entered in the *Time to Analog Converter* (TAC). TAC starts operation when it gets signal and stops when it gets the second signal. An output signal from TAC is proportional to operation time. In our experiments we have manually gated the *Analog to Digital Converter* (ADC) that receives the TAC signal using the *Timing Single Channel Analyzers, Delay Amplifiers, Gate and Delay*
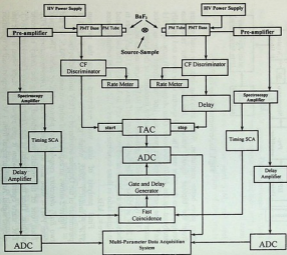
Fig.2 Experimental Setup for PALS

The diagram shows the experimental setup with the following labeled components:

- HV Power Supply (left and right)
- BaF$_2$
- PMT Tube, PMT Bias (left and right)
- Source-Sample
- Pre-amplifier (left and right)
- CF Discriminator (left and right)
- Rate Meter (left and right)
- Delay
- Spectroscopy Amplifier (left and right)
- Timing SCA (left and right)
- TAC (start / stop)
- ADC
- Delay Amplifier (left and right)
- Gate and Delay Generator
- Fast Coincidence
- ADC (left and right)
- Multi-Parameter Data Acquisition System

Generators and Fast Coincidence Module. We have gated the ADC in such a way that it counted mostly signals of interest. That means that we have been using an energy window around 1274 keV as a start signal for the TAC and an energy window around 511 keV as a stop signal for TAC. This experimental setup gives us a clean spectrum on top of a small background.

The typical count rate obtained was from 0.2 Hz to 0.5 Hz. The resolution curve was taken with ^{60}Co source, which emits two different energy gammas almost simultaneously. Timing resolution of the system was 280ps.

Spectra taken from PALS were analyzed by the software called Kansy *Lifetime9*. This software is specifically written for PALS analysis and is accepted internationally. The program looks at the central part of the lifetime spectrum and fits it with the Gaussian function. Therefore it estimates the FWHM of the central part of the peak, which is the timing resolution of the experimental setup used. Then it fits the tail of the spectrum with the convoluted spectrum of Gaussian and one or several exponential decays with different lifetimes. The software finds the best combination of parameters that suit the spectrum and gives the results for the lifetimes of the decay lines. The program also estimates the background to signal ratio in the spectrum [5].

RESULTS

PEAS and PALS on radiation-damaged specimens of stainless steel 316L and steel 9Cr1Mo showed the following results.

In our energy spectroscopy measurements, we measured T = W/S, where W is the sum of counts in the "tails" and "wings" of the 511keV peak, and S is the sum of counts in the center of the same peak. T-parameter should decline as defects are introduced into a specimen. As experiments showed the T parameter decreased with dose in case of stainless steel 316L. At the same time the trapping intensity of positrons in defects generated increased. This means that when increasing dose, we generate more and bigger defects in the material as expected.

However, in case of steel 9Cr1Mo positron trapping intensities increased, thus more defects were generated, but the T parameter

177

showed incensement. The dependence of the T parameter on dose is shown in Figure 3. Such a behaviour of the T parameter means that the molybdenum decoration of defects is observed [6]. Steel 9Cr1Mo contains 1% Molybdenum which is high Z (Z=42) material positron annihilations with its valence electrons is the reason of the growth of T with dose.
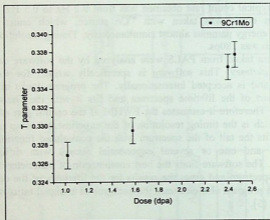
Fig.3. The dependence of the T parameter of the annihilation 511 keV line on dose

Positron lifetimes in stainless steel 316L didn't change in the doses delivered, while in steel 9Cr1Mo the positron lifetime in defects decreased with dose from 1.02 dpa to 2.46 dpa. This implies that the electron density at the annihilation sites, defects in this case, increased. This is due to the helium or other gases inside the defects, the concentration of which increased when applying more dose [7,8].

CONCLUSIONS

Radiation-damaged specimens of stainless steel 316L and steel 9Cr1Mo have been investigated in this research using the PAES and PALS. All specimens of interest contained several radioactive sources, which were introduced in them during irradiation. One of such sources was radioactive ^{22}Na positron source which we used during PAES and PALS experiments. Doses delivered to samples of interest during the activation were from 1.02dpa to 10.3dpa.

As the results show investigation of lower dose samples over a range of doses with PAES and PALS techniques would be significant. A detailed study of specimens of interest at lower doses would enable one to uncover the relationship between radiation damage and PAES/PALS signals.

ACKNOWLEDGMENTS

REFERENCES

1. P. Hautojarvi et al. Positrons in Solids, Springer, 1979.
2. M. Charlton et al., Positron Physics, Cambridge, 2001.
3. F.A. Selim, D.P. Wells, et al., Nuclear Instruments and Methods in Physics Research B, **192**, 2002, 197.
4. F.A. Selim, D.P. Wells, et al. Radiation Physics and Chemistry. **68**, 2003, 427.
5. J. Kansy, Nuclear Instruments and Methods in Physics Research A, **374**, 1996, 235.
6. P. Asoka-Kumar et al., UCRL-JC-142592
7. K.O. Jensen, Defects and Diffusion Forum, **57-58**, 1988, 207.
8. K.O. Jensen et al., J. Physics. F: Met. Phys. **18**, 1998, 1069.

* Tbilisi State University
** Department of Physics and Idaho Accelerator Center, Idaho State University, Pocatello, Idaho, USA

ლ. ჯელაძე, დ.პ. ველსი

**პოზიტრონის ანასილაციის სიცოცხლის ხანგრძლივობისა
და ანასოირებული გამა ნაწილაკების ენერგიის
შესწავლა უჟანგ ფოლად 316L და ფოლად 9Cr1Mo-ის
მაგალითზე**

დასკვნა

ნაშრომში შესწავლილია რადიაციულად დასხივებული
უჟანგ ფოლად 316L და ფოლად 9Cr1Mo-ის თვისებებში პო-
ზიტრონების ანასილაციის სიცოცხლის ხანგრძლივობასა
და ანასოირებული გამა ნაწილაკების ენერგიის და-
კვირვებას. მიღებულია შედეგები ანასილაციის 511 keV
სპექტროსკოპიური ხაზის მახასიათებელი S, W და T პარა-
მეტრებისათვის, ასევე პოზიტრონების ანასილაციის ინტე-
სიურობისა და სიცოცხლის ხანგრძლივობის ძირითადი მახა-
სიათებელი T პარამეტრი, პოზიტრონების ანასილაციის
ინტენსიურობისა და სიცოცხლის ხანგრძლივობის დასხი-
ვების დოზაზე დამოკიდებულება აღწერილია ისეთი ფორ-
მით, როგორიც მოსალოდნელი იყო.

USE OF LASER RAMAN SPECTROSCOPY FOR STUDY OF SURFACE PROPERTIES OF SOME SEMICONDUCTORS OF A³B⁵ TYPE

S. Gotoshia[*], L. Gotoshia[**]

ABSTRACT. Laser Raman spectroscopy is used to study optical properties of surface thin layers of semiconductors. Use of various wavelengths of exciting laser enabled us to alter at request the skin values of penetration of laser radiation in films under observation. Through proper selection of film thicknesses, absorption coefficients and skin-values, we achieved absolute exclusion of interfering LO and TO phonons of substrate from Raman spectra of various films of $Ga_xAl_{1-x}P$ under observation.

That enabled us to fix LO_1, LO_2, TO_2 vibrations of optical phonon branches for GaP- and AlP-like sublattices to a high accuracy and plot more accurate graphs characterizing two-mode crystal. On the basis of this technique we were able to estimate thicknesses of films and the first to study resonance Raman scattering in system $Ga_xAl_{1-x}P$. With the aid of laser Raman spectroscopy surface thin layers modified by P and Al ion implantation of substrates of GaAs and GaP, respectively, has been studied. Varying technological conditions of ion implantation we obtained amorphous ternary thin films α-GaAsP, α-GaAlP of substrate.

Their identification for various depths has been done with laser Raman spectroscopy.

As is well known, the main tendency of modern semiconductor microelectronic instrument-making industry is miniaturization of devices. This, on its part, is based on use of semiconductor material's surfaces rather than bulk crystals. An obvious example of this is epitaxial films' use for that purpose. These films may be received both by usual chemical (liquid-phase, molecular, organo-metallic epitaxy and their different modifications) methods, and various physical

181

extremal methods (ion implantation, radiation-laser, electron beam and etc.). Utilization of those methods implies both this surfaces' reception and preliminary modification of existing substrates' properties for goal achievement. Dimension of such layers may be changed from nanosizes to microsizes. Naturally, the problem of testing such thin layers and objects of small sizes arises. Most likely, there are mainly two problems to be taken into consideration. The first one, physical, consists in the following: in a perfect three-dimensional crystal the region over which the spatial correlation function of the phonon extends is infinite. This leads to the fact that phonons' propagation is expressed by plane waves and in the first order Raman scattering the q = 0 selection rule is observed. In direct space the phonons of microcrystalline materials are confined within spheres with diameter L. Description of such phonons is carried out in reciprocal space with wave packet with wave vector k in interval $\Delta k \approx L^{-1}$. Just when studying a microcrystalline semiconductor Si, Richter introduced the so-called "phonon confinement" conception, according to which shift of phonons' frequencies and asymmetric broadening of halfwidths take place in microcrystalline materials.

Here a concrete example is given for Raman scattering on phonons, but the fact that almost all properties of spatial crystal differ from physico-chemical properties of nanomaterials and thin layers, is already admitted generally. This first basic physical difference gives rise to the second, "geometrical" problem, as we call it - testing methods for small dimension materials are to be selected in such a way that they correspond to experimental fixing of their different properties and manifestation of peculiarities. For example, by usual spectroscopic methods it is difficult or impossible to carry out univocal measurements from thin films, micro or nano materials, and out-of-the-way places. There is no theoretical possibility of this sometimes, because it is impossible for incoherent and great classical radiation source emission to be focused on micro or less sizes, and it is almost impossible to direct this radiation concentrically. Multicolored directions of laser spectroscopy based on various physical principles are irreplaceable for this objective. In the present article the possibilities of only one of the basic directions of laser spectroscopy-laser Raman spectroscopy will be discussed. Naturally, the universally

recognized physical methods, as various analytical methods based on ion, X-Ray and electronic beam sondes will not be touched.

In 1976 first in Georgia we constructed several laser Raman spectrometers of various types, carried out investigations in different directions, and thus most likely grounded development of laser Raman spectroscopy direction in Georgia. The analogues of the laser Raman systems we have constructed are very expensive at international markets. Perhaps, that is why this very important scientific direction has not found corresponding propagation in Georgia as yet. It is a pity, because this direction's potential is very high and practical almost in all spheres of science from fundamental as well as applied, analytical, industrial points of view.

One of the aims of the work presented here is just the popularization of the mentioned direction among scientists from the point of its wide utilization. We shall try to realize this purpose on the basis of the experiments we have made. This time, all these experiments show monitoring of semiconductor surfaces by laser Raman spectroscopy.

When studying surfaces by laser methods, peculiarity and advantage in comparison with classic, ordinary optic spectroscopy mainly consists in use laser as a radiation source. Laser's advantage is expressed with its radiation coherence, radiation unidirectionality, narrowness of its radiation spectral band; it has property of summing its radiation with the aid of lenses in focal point of very small size (of nano dimensions). A lot of types of lasers of the day enable to change discreetly their radiation from ultraviolet of optical spectrum to near infrared area; according to spectral task, if necessary, this area may be overlapped continuously (with the aid of dye lasers, semiconductor heterolasers, nonlinear laser optics and other lather techniques). Geometric mobility of laser beam is of great importance, also - it may penetrate out of the way places and analyze and interact with matter even from the aggressive medium (from separating surface of heterosurfaces, the phase buried in crystal matrix, various inclusions in minerals, active zone of reactor, high temperature and acid volumes and many others).

We are presenting our experimental material and discussing two different themes concerning semiconductor surfaces we have studied by laser Raman spectroscopy.

1. RESONANCE RAMAN-SPECTROSCOPY OF MIXED SEMICONDUCTORS $Ga_xAl_{1-x}P$ AND ESTIMATION OF FILMS' THICKNESS

The mixed $Ga_xAl_{1-x}P$ crystal is an interesting material though less studied for semiconductor electronics. Particular interest in this material is caused by the fact that because of its wide band-gap it could be used for making light-emitting devices in visible region of spectrum. For example, semiconductor heterostructural Raman-lasers were made on its ground [1]. Optical properties of this compound have been less studied while Crystal lattice vibrational dynamics is discussed in works [2-5].

With Raman-spectroscopy we routinely study semiconductors modified by ion implantation, especially complex semiconductors synthesized by ion implantation. Simultaneously, we elaborate standards for qualitative identification of ion synthesized films and their quantitative estimation as the result of Raman scattering studies of the same semiconductors synthesized by ordinary chemical methods, for example, by liquid phase epitaxy.

The above-mentioned work serves just the purpose. On the other hand, identification of phonons in $Ga_xAl_{1-x}P$ and studies of mode structure of this compound is needed for interpretation of Raman-spectra of quaternary $(Al_yGa_{1-y})_{0.5}In_{0.5}P$, a necessary semiconductor at present. This is connected to the fact that this compound consists of components $Ga_xAl_{1-x}P$ and $Ga_xIn_{1-x}P$. The above mentioned quaternary semiconductor grown epitaxially on GaAs substrate is widely used nowadays in the visible region of spectrum for producing light-emitting microelectronic devices, as it has wide forbidden zone.

In the present work Raman scattering has been studied in a lot of n- and p-type $Ga_xAl_{1-x}P$ epitaxial films. We studied undoped films as well. The mentioned films were grown by liquid-phase epitaxy on GaP substrates with (001) orientation. Film thickness was in the range of 5-18 mmk.

The Raman-spectra were recorded on the home-made laser Raman-spectrometer constructed on the base of double monochromator DFC-24. Argon laser emission of 514.5, 488.0, 457.9 nm and excitation source helium-cadmium laser emission of 441.6 nm

wavelengths respectively served as excitation source. The Raman system experimental equipment is described in details in [6].

Fig.1 shows Raman-spectra for $Ga_{0.3}Al_{0.7}P$ composition when exciting by various wavelengths of laser. It is clear from the picture that when we use short waves to get spectrum, the intensity of LO phonon of GaP substrate at 402 cm^{-1} diminishes gradually and when carrying out excitation with helium-cadmium laser radiation with 441.6 nm wavelength, the peak characterizing LO phonon vanishes at all. Simultaneously increases the intensity of LO phonon at 487 cm^{-1}, which characterizes vibration of a sublattice similar to AlP in $Ga_{0.3}Al_{0.7}P$ system. Thus, with shortening the exciting laser's wavelength, manifestation of interfering spectrum of substrate gradually decreases, and in boundary conditions we are absolutely free from it.
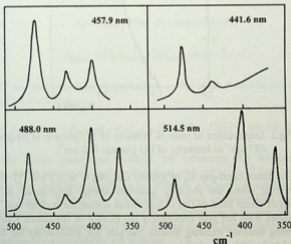
Fig.1. Raman spectra for $Ga_{0.3}Al_{0.7}P$ excited with various wavelengths of the laser.

Fig.2 shows the dependence of ratio of LO phonons intensities at 487 cm^{-1} and 402 cm^{-1} frequencies respectively upon energy of exciting photons.
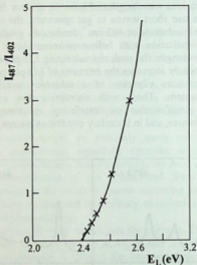
Fig.2. Dependence of ratio of intensity of LO phonon at frequency 487 cm^{-1} to intensity of LO phonon 402 cm^{-1}.

The direct band-gap E_6 of system $Ga_{0.3}Al_{0.7}P$ is 3.5 eV [7]. Fig.2 shows that when the exciting quantum energy approaches to the amount of direct band of $Ga_{0.3}Al_{0.7}P$, weak resonance is observed. The mentioned does not give completely the picture of resonance Raman-scattering because exciting quanta energies are sufficiently far from direct band width. We shall have the complete picture if we are able to use laser shorter wavelengths for excitation. Besides it will be more correct if we take the ratio of LO_{487} to phonon vibration intensity of standard crystal CaF_2.

The fact that we study the system-GaP substrate with $Ga_xAl_{1-x}P$ film-by various wavelength of laser emission, gives us the possibility to estimate epitaxial layers' rough thickness by Raman-spectroscopy.

According to [8] Raman-scattering intensity

$$I = (I_0 R / 2\alpha)(1 - \exp 2\alpha d), \quad (1)$$

where I_0 is intensity of impinged radiation, R_0 - scattering cross-section, α - absorption coefficient, d - film thickness.

If we assume that the film $Ga_xAl_{1-x}P$ is grown on GaP substrate with steep front, then it is possible to assume, that the scattering intensity equals to substrate and film Raman scattering intensities sum.

$$I_{Total} = I_f + I_{subst} \exp(-2\alpha_f d) \quad (2)$$

$$I_f = (I_0 R_f / 2\alpha_f)[1 - \exp(-2\alpha_f d)] \quad (3)$$

$$I_{subst} = (I_0 R_{subst} / 2\alpha_{subst}) \exp(-2\alpha_f d) \quad (4)$$

If we take the ratio of intensities, it would be possible to calculate the film thickness.

$$I_{subst} / I_f = (R_{subst} \alpha_f / R_f \alpha_{subst})[\exp(-2\alpha_f d)] / [1 - \exp(-2\alpha_f d)] \quad (5)$$

By above mentioned method we estimated the thickness of $Ga_{0.3}Al_{0.7}P$ composition film thickness and got $d = 12.5$ micm. The same film thickness measured by ordinary microscopic method gives $d = 12$ micm. In this case comparatively thick epitaxial film has been estimated. In a same manner may be estimated much thinner films, for instance, nano dimensional films formed by ion implantation, only if corresponding conditions are selected.

Scanning of focal point on the surface of the film under investigation was carried out after sharp focusing of laser beam. Raman spectra were fixed from all points, afterwards there were compared spectral lines intensities, halfwidths. This enabled to estimate films' quality along the surface, their homogeneity.

Fig.3 shows graphs plotted after recording Raman spectra of epitaxial films of different composition. They show dependence of vibration frequency of LO phonons of GaP- and AlP-like sublattices upon implant's compositions. According to these graphs the system $Ga_{1-x}Al_xP$ is attributed to two-mode behavior crystals. By means of these calibration curves the compositions of nanodimensional films $Ga_{1-x}Al_xP$ synthesized by us with two different doses ($2.8 \cdot 10^{16}$ and $2.5 \cdot 10^{17}$ ion/cm^2) of ion implantation, have been defined. It turned out that $x_1 = 0.12$ when implanting with $2.8 \cdot 10^{16}$Al ion/cm^2 and the concentration of synthesized ternary compound $x_2 = 0.24$ at dosage of $2.5 \cdot 10^{17}$ Al ion/cm^2.
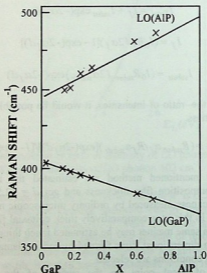
Fig.3. Dependence of the frequency of LO phonons on the composition.

2. MONITORING OF SEMICONDUCTORS GaAs AND GaP MODIFIED BY ION IMPLANTATION

Accelerated ions' penetration depth in substrates at ion implantation is determined by their energies, masses, charge values and substrate parameters. Implantation of substrates GaAs and AlP was carried out by means of charged ions of Ar, B, N, O, As, P, Al. These ions' energies varied in various cases and substrates formed by ions with 40, 60, 70, 100, 110 keV energies were mainly investigated. We had also substrates doped with so-called "distributed dose". In this case in the same substrate the implantation of the same ion with certain dose occurred, energies being changed in the great range. In these cases ion distribution function in substrates sharply differs from distribution function formed at implantation by energy with the same value. As a rule, in this case the layer formed in substrate is thicker, near surface and spreads at comparatively longer distance. It should be noted, that this is not a rule, but depends on choice of energy distribution function. It should be added, that ion implantation technique in semiconductor microelectronics is attractive just because, unlike chemical technologies, in it is possible to vary strictly at request and control to a high accuracy all the parameters of substrate modification. Thus, it is possible to obtain layers of certain thickness and expansion with implantation energy change. On conducting our experiments implantation was carried out at substrate temperatures being about room temperatures, 400^0 and 450^0 C.

With the aid of laser spectroscopy one can carry out sounding of the modified substrate in the depth as well as in any surface direction. Such spatial dispersion is possible only in case of being at experimenter's disposal exciting lasers with a wide variety of wavelengths. In that case substrate skin-layer of laser radiation is proportional to absorption coefficients of the substrate and to modified-layer; if skin-layer is equal to or smaller than the modified-layer, only then occurs sounding of the modified layer and the experimental results show only the layer characteristics. Another approach is also possible: to alter ion implantation energies at fixed Raman spectra exciting wavelengths to obtain modified layers of various thicknesses. The both means are at our disposal; only the second variant will be discussed in the present work.

To receive amorphous films we were dealing with ion implantation of monocrystalline GaP and GaAs targets by Ar, B, N, P, Al, As ions. The target surfaces were of two kinds: (111) and (001) orientations. Ion energies varied from 40 to 110 keV we dealt with amorphous films of various thickness in different depths from the crystalline surface. Implantation was fulfilled with different doses at room temperature as well as at high 400° and 450° C temperatures. For Raman-spectra recording home-made Raman-spectrometer constructed on the basis of double monochromator DFS-12 was used. Argon laser emission wavelengths 514.5 nm, 448.0 nm, 457.9 nm and Helium-Cadmium laser emission wavelength 441.6 nm were used for spectra exciting. The mentioned emission wavelengths were chosen so that we should be able to conduct probing in different depths of target surfaces implanted with various energies.

As is known in Raman scattering in crystal compounds optical phonon is absorbed or illuminated at about $k = 0$. When crystal structure is crushed and because of disappearing far order, the periodicity is lost, then $k = 0$ selection rule loses its sense and in the first order Raman scattering phonons with big k are participating. Such state is originated in amorphous semiconductors, when all vibrational modes are allowed and take part in Raman scattering process. Thus, we conclude that in amorphous semiconductors the first order Raman spectra reflect the general form of distribution of one-phonon density vibrational state. Vibrational state density of amorphous compounds in the first approximation seems to express the extended variant of the proper crystal lattice vibrational state density and $A^N B^5$ group semiconductor Raman spectra as well as IV group have the whole spectrum characteristic structure rather than the narrow bands, which correspond to the zero wave vector phonons which are active in Raman scattering.

Crystalline GaP and GaAs are of cubic symmetry with point group symmetry T_d. Therefore, on the basis of the group theory analyses according to the selection rules, when exciting (001) surface by laser emission, in Raman spectrum only LO phonon is observed, as for the (111) surface, here both LO and TO phonons are observed. For GaP LO=402 cm⁻¹, TO = 365 cm⁻¹; for GaAs LO = 290 cm⁻¹, TO=268 cm⁻¹.

Fig.4 shows Raman-spectrum, which reflects the picture created by phosphorous ion implantation in GaAs. The implantation occured at the room temperature the implantation dosage being 10^{17} ion/cm^2. Two wide bands at about 275 cm^{-1} and 375 cm^{-1} are distinctly seen in the Raman-spectrum. These bands are sharply shifted from α-GaAs and α-GaP characteristic spectra. Their ion syntheses and identification by Raman has been done in our work [9]. Thus the Raman-spectra in Fig.4 characterizes a new compound α-GaPAs, where the band at about 275 cm^{-1} corresponds to Ga-As pair vibration; the band at about 375 cm^{-1} shows Ga-P pair vibration.
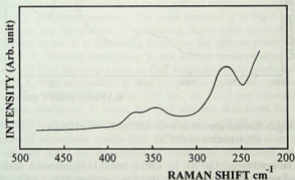
Fig.4. Raman-spectra of α-GaAsP synthesized by ion implantation at room temperature.

During the high temperature (400^{0}C) synthesis, amorphous ternary compound α-GaPAs is obtained; however because of its characteristic spectral bands being slightly narrower and more intensive, we can conclude that in this case radiation defects are probably smaller. That is shown in Fig.5.

When implanting GaP with 70 keV energetic arsenicum ion with 10^{17} ion/cm^2 dose, identification of ternary compound GaPAs had not been managed; neither ternary compound GaPN had been identified when implanting nitrogen in GaP with 10^{17} ion/cm^2 dose. That can be explained by energetically adverse

conditions for these compounds to be synthesized according to the mentioned scheme. Though in the latest period, works, in which ternary compounds GaPN and GaAsN has been synthesized by nitrogen ion implantation in GaP and GaAs and identified, appear [10,11].
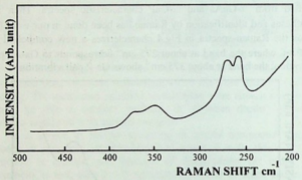
Fig.5. Raman-spectra of α-GaAsP synthesized by ion implantation at 400⁰ C.

To synthesize GaPAl in (001) and (111) oriented GaP we introduced aluminum ions by ion implantation with doses $2.8 \cdot 10^{16}$, $2.5 \cdot 10^{17}$ ion/cm² with 100 and 110 keV energies respectively. Implantation was carried out at 400⁰ C. Ion implantation was carried out also by 60 keV energy aluminum ions with $8.7 \cdot 10^{16}$ ion/cm² dose at 450⁰C.

In all three cases at the GaP surface single-phase ternary compound GaAlP is formed in the amorphous state. The mentioned are proved by two wide spectral bands in RS: one in the 450 cm⁻¹ region which corresponds to Al-P pair vibration and the second, which is in the 400-350 cm⁻¹ region and reflects the Ga-P pair vibration. That is shown in Fig.6 and Fig.7 respectively.

Fig.6 shows Raman spectra of α-AlGaP, when it is synthesized by bombardment GaP substrate with comparatively high-energy, 100

KeV, aluminum ions. Fig.7 shows the characteristic spectrum of α-AlGaP; it was fixed when bombarding GaP substrate with low-energy, 60 KeV, aluminum ions. The spectra presented in Figs.4, 5, 6, 7 have been recorded with the same wavelength 514.5 nm excitation. When implanting GaAs with phosphorus, the ion path with its correction does not exceed 100 nm. That is, the synthesized amorphous α-GaAsP is of the same order. At wavelength of 514.5 nm the skin-layer of GaAs, calculated by absorption coefficient is about 100 nm, whereas for synthesized amorphous layer the absorption coefficient increases still more. So, in that case only nanodimensional amorphous layer is being studied with 514.4nm excitation; therefore only the characteristic layer of amorphous layer without substrate spectrum is manifested in Raman spectrum. The same situation is in Fig.5 and 6. In this case too the picture of monitoring shows only conditions of synthesized layers. It is interesting to analyze the spectra presented in Fig.6 and 7, showing amorphous layers formed by implanting with 100 and 60 KeV aluminum ions in GaP respectively. At implantation with 100 KeV aluminum ions in GaP ion path is about 500 nm, and at implantation with 60 KeV, about 300 nm. At 514.5 nm wavelength absorption coefficient is lower for GaP and the skin-layer for this wavelength is almost 20 mnm. Synthesizing of α-AlGaP causes sharp increase of absorption coefficient. At implantation with aluminum ions of 100 KeV the production of absorption coefficient, α, by thickness of amorphous layer d, that is, $αd$, is of such a size that radiation of 514.5 nm is being entirely absorbed in amorphous layer. Because of this the Raman spectrum is only characteristic of layer as is shown in Fig.6. At implantation with 60 KeV aluminum $αd$ is not of such magnitude to absorb radiation 514.5 nm entirely; it passes through the substrate and stimulates its excitation. As a result, in Raman spectrum both, two wide bands, characteristics of α-AlGaP and a narrow band of LO phonon of substrare GaP, are fixed simultaneously. These are shown in Fig.7. In this case the narrow band of LO phonon is a very good reference point for measuring precisely the frequency shift as well as for estimating thickness of amorphous layer.

In that way, resonance Raman scattering of ternary mixed crystal AlGaP synthesized by liquid-phase epitaxy has been studied. That

193

enables to study fundamental physical properties of thin layers and estimate their thickness. Besides, laser Raman-assisted qualitative and quantitative analyses of nanodimensional layers of GaAs and GaP monocrystal substrates modified by ion implantation have been made. It has been found, that the mentioned nanolayers correspond to amorphous ternary compounds GaAsP and AlGaP.
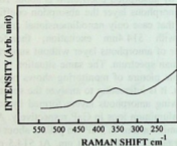
Fig.6. Raman spectra of α-AlGaP synthesized by ion implantation at 400^0 C and at energy of implantation, E = 100 KeV.
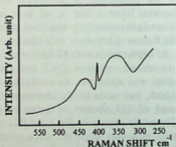
Fig.7. Raman spectra of α-AlGaP synthesized by ion implantation at 450^0 C and at energy of implantation, E = 60 KeV.

REFERENCES

1. K. Suto, T. Kimura and J. Nishizawa. Appl. Phys. lett. **51**, 1987, 1457.

2. H. Sobotta, V. Riede, K. Buchheiser. Czech. J. Phys. **B25**, 1975, 841.

3. B.Kh. Bairamov, V.N. Bessolov, E. Iane, Iu.P. Iakovlev, V.V. Toporkov, Sh.V. Ubaidullaev. Pisma Zh. Eksp. Teor. Fiz. **6**, 1980, 1432.

4. G. Lucovsky, R.D. Burnham, and A.S. Alimonda, Phys. Rev. **B14**, 1976, 2503.

5. S. V. Gotoshia. Bulletin of Georgian Academy of Science. **168**, 2003, 41.

6. S. Gotoshia. Bulletin of Georgian Academy of Science. **159**, 1999, 241.

7. J.M. Rodriguez, G. Armelles and P. Salvador, J. Appl. Phys. **66**, 1989, 3929.

8. R. Loudon, J. Physique. **26**, 1965, 677.

9. S. Gotoshia, L. Gotoshia. Bulletin of Georgian Academy of Science. **160**, 1999, 234.

10. X. W. Lin, M. Behar, R. Maltez, at all. Appl. Phys. Lett. **67**, **(18)**, 1995, 2699.

11. Xizhen Yang, Zhenjin Lin, Zhigang Li, at all, J Appl. Phys. **77**, **(11)**, 1995, 5563.

*Georgian Academy of Sciences
Institute of Inorganic Chemistry and Electrochemistry
**Tbilisi State University

ს. გოთოშია,   ლ. გოთოშია

ლაზერული რამან-სკექტროსკოპიის გამოყენება A^3B^5 ტიპის ზოგიერთი ნახევარგამტარის ზედაპირული თვისებების შესასწავლად

დასკვნა

შრომაში ნაჩვენებია ლაზერული რამან-სკექტროსკო-
პიის მნიშვნელობა და განსაკუთრებული ნახევარგამტარ-
ების ზედაპირული ფენების შესწავლის სფეროში. კერძოდ,
ეს განაპირობებია ნახერხულ, როდესაც რამან-სკექტრო-
ების ამხანაგ წყაროდ გამოიყენებოდა. მაგალითადის ნახევ
განხილულია ჩვენ მიერ სამგავ ზრგავ ნახევარგამტარ
$Ga_xAl_{1-x}P$-ში რეჟიანიანური რამანი გაძევა სხვადასხვა
ლაზერული სხივდასხვა ტალღის სიგრძის ახზნებისას. ახზ-
ლო ტექნიკის სიმაღლეთი შემედუ შემედუ შემედიშესაშ ამ
სისტემის ფუნდამენტური თვისებებისა და შემფასებისა
ფირებისა სისინს.

საინტერესო და მნიშვნელობა ამ მეთოდით A^3B^5
ტიპის ნახევარგამტარებში GaAs და GaP მართალი იოია
მოდიფიცირებულებას ზედაპირული შესწავი და ადგერლი-
კაცი. დავადგინელ, რომ ერთ-ფასული GaAs და GaP ზედა-
პირების ფისტორულ და ალუმინ ორბანა ბოაბაარბაარი
ბისას შესაბამისა, ამავ ზედაპირულე კრისტალურ ფენდ
ტრანსფორმირებულ ამირცულ სტრუქტურებ პირველ
შემოქტებ სარჩიული ზედაპირების წარმოქმნა ამორფუ-
ლებ ერთფასიან სამ და ნაერთა GaAsP, ხოლო მეორე
შემოქტებაში ამორფული GaPAl. ლაზერულ ზონდიურთ
შეგედანის შესაფასით ამ ამოფული სტრუქტურ
ზედაპირიდ გავრცელების სიღრმეებ.

LASER RAMAN SPECTROSCOPY STUDIES OF FREE CARRIERS' INTERACTION WITH OPTICAL PHONONS AND SURFACE SPACE CHARGE EFFECT ON PHONON SPECTRUM IN GAP

S. Gotoshia,* L. Gotoshia**

ABSTRACT. In the present work free carriers' interaction with phonons both with volume and surface excitation has been investigated. Having studied the regularity of plasmon-phonon interaction in GaP, effect of electric field, induced by surface space charge, on phonon spectrum has been revealed. At volume excitation LO phonon's halfwidth is being widen in GaP according to a certain rule as a result of increase of free carriers and the mentioned widening is far distinctly expressed in p-GaP. After surface excitation it was found that on shortening of wavelength of exciting laser LO phonon halfwidth sharply decreases with increase of free carrier's concentration. Such an effect was fixed from (001) surface of GaP. In the process of investigation of (110) surface it has been found that at small concentration of electrons forbidden LO phonon is still observed from (110) surface with sufficient intensity. With increase of electron concentration LO phonon intensity increases pronouncedly and its intensity prevails over intensity of TO phonon. After covering surface (110) of GaP with semitransparent metal film of aluminum intensity of LO phonon increases still more. The observed experimental results we have explained in terms of formation of electron depletion surface layer due to electric field induced by space charge.

When impurities in GaP are in abundance to form free carriers, then interaction between longitudinal optical LO phonons and electric field generated by charge density fluctuation of free carriers takes place. As a result of this interaction a bound state of two fundamental excited particles, LO phonon and plasmon, is formed.

Free carriers in semiconductors display plasma properties with characteristic plasma frequency:

$$\varpi_p = \left(\frac{4\pi Ne^2}{\varepsilon_\infty m^*}\right)^{1/2} \qquad (1)$$

Where N is charge carriers' concentration, e-electron charge, ε_∞- dielectric permittivity of high-frequency, and m^* - charge carriers' effective mass. Plasma vibration is longitudinal wave of charge density. Perturbation caused by this wave, forms electric field interacting with electric field of longitudinal vibrations of crystal lattice in polar semiconductors. Thus, as a result of interaction of longitudinal optical mode LO with plasma vibration, the bound plasmon-phonon vibrations are produced (which include common ion and electron motions) with a new, different frequency.

If damping of plasma vibration is ignored, the solution of equation for plasmon-phonon modes' frequencies will be as follows:

$$(\omega_\pm^0)^2 = 1/2(\omega_{LO}^2 + \varpi_p^2) \pm \frac{1}{2}[(\omega_{LO}^2 + \varpi_p^2)^2 - 4\omega_{TO}^2 \varpi_p^2]^{1/2} \qquad (2)$$

Experimentally observed plasmon frequencies ω_+ and ω_- ($\omega_+ > \omega_{LO}$, $\omega_- < \omega_{TO}$) are in good agreement with theoretical expression (2).

When studying plasmons and polar phonons interaction both conductivity type (n or p) and energy-band structure should be taken into consideration.

On recording and study of characteristic spectrum of plasmon-phonon interaction of other semiconductors of A^3B^5 type, for instance, GaAs, the spectrum shows frequency peaks of LO and TO phonons and simultaneously frequency peaks, ν_+ and ν_-, respectively, of plasmon-phonon interaction of high and low frequency branches, four peaks altogether.

Plasmon-phonon mode frequency ν_+ is closely approximated to LO phonon frequency, ν_{LO}, over the range of possible doping by impurities of GaP ($\sim 10^{16} \div 10^{19}$ electron cm^{-3}). In such a case only

three peaks of v_-, v_{TO}, v_+ are seen in Raman scattering spectrum. With doping order increase (free carriers' number increases) plasmon-phonon peaks' frequencies are displaced towards high frequencies and broadened. For finite value $v_p \to 0$ (undoped gallium phosphide), $v_+ \to v_{LO}$ and spectral band half-width of high frequency branch of plasmon-phonon mode approximates to the half-width of optical phonon band, $\Gamma_+ \to \Gamma_{LO}$. Spectral bands corresponding to low frequency branch has not been detected yet in GaP, probably, because of their too low intensity or due to other physical difficulties.

Plasmon-phonon interaction in GaP has been studied in some papers [1-4]. In all of these papers free carriers interaction with polar phonons has been studied by 632.8 nm wavelength excitation of helium-neon laser. This is equivalent to volume excitation of GaP, when surface and resonant effects do not affect plasmon-phonon interaction.

The purpose of the present paper is to study plasmon-phonon interaction in n- and p-type GaP by 632.8 nm volume excitation as well as plasmon-phonon interaction from near-to-surface layers. Toward this end besides 632.8 nm wavelength of helium-neon laser the following wavelengths of argon, krypton and helium-cadmium lasers have been used to excite Raman spectra: 568.2; 514.5; 488.0; 476.5; 457.9; 441.6 nm. The spectra had been analyzed on lab-type laser Raman spectrometer constructed on basis of double monochromator DFS-24 described in [5].

Gallium-phosphide with electron conduction as well as with hole conduction has been studied. At the same time Raman spectra of high-resistance semi-insulating GaP has been recorded too. One category of n-GaP monocrystals was doped with sulphur, electron concentration being $2 \cdot 10^{17}$ cm^{-3}, the second was doped with tellurium, electron concentration being $2.2 \cdot 10^{18}$ cm^{-3}, the third category of monocrystals was doped specially, it was of n-type with electron concentration in it not exceeding 10^{16} cm^{-3}. A monocrystal of p-GaP was doped with Zn, the hole concentration being $5 \cdot 10^{18}$ cm^{-3}. A compensated monocrystal of GaP, semiinsulating, with conductivity 10^{12}–10^{14} ohmxcm and electron concentration not exceeding 10^{14} cm^{-3} has been also studied. The monocrystal's surfaces were of (001) and

(111) orientations. All the measurements were made at room temperature.

As is well known, GaP is an indirect band gap semiconductor with zinc blend structure. The value of its minimum indirect band gap is 2.26 eV and that of the first direct band gap is 2.79 eV at room temperature. Accordingly, the skin-layer corresponding to the abovementioned exciting wavelengths has different values. Therefore, for wavelengths 632.8 and 568.2 nm GaP is transparent and volume excitation takes place. Through other wavelengths surface layers' (having different thicknesses) monitoring takes place. Besides, for the shortest waves transparence Raman scattering (RRS) takes place as we have shown in [6].

Fig.1 shows Raman spectra of GaP for two different quantities of free carriers. The first crystal is compensated with chromium, semi-insulating, with electron concentration not exceeding 10^{14} cm^{-3}. The second is of hole conduction, doped with zinc impurities, with hole concentration equal to $6.9 \cdot 10^{18}$ cm^{-3}. In both cases Raman scattering spectra were excited by helium-neon gaseous laser emission $\lambda_l = 632.8$ nm. Such an experimental situation enables one to carry out analysis of scattered light from the whole volume rather than from small surface skin-layer.

The spectra in Fig.1 show clearly that in p-type semiconductor with the hole concentration increase, spectral band halfwidth characterizing LO optical phonon increases distinctly becoming $\Gamma_s = 10.5$ cm^{-1}. At the same time this peak is shifted towards high frequencies for about 3cm^{-1} (Fig.1b) from LO optical phonon (characterizing a high-resistance crystal) peak frequency at 402 cm^{-1} (Fig.1a). The mentioned peak is identified, as mentioned in theoretical part of the paper, as plasmon-phonon interaction peak of high-frequency branch. In this case free heavy holes produce plasmon vibrations.

Raman scattering spectra of n-GaP doped with donor-type impurities, sulfur in the first case and tellurium in the second, recorded for $\lambda_l = 488.0$ nm (2.54 eV) excitation of ion laser emission have been studied. The electron concentration was $2 \cdot 10^{17}$ cm^{-3} in S-doped samples and $2.2 \cdot 10^{18}$ cm^{-3} in Te-doped ones. For the purpose of comparison the spectrum of semi-insulating GaP has been also
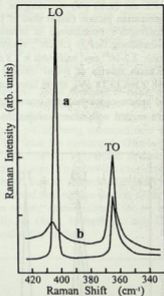
Fig.1. Raman spectra of high-resistance GaP (1a) and GaP with 6.9·10[18] cm^{-3} concentration of holes (1b); excitation 632.8 nm.

recorded with electron concentration not exceeding 10[14] cm^{-3}. The spectra show LO phonon halfwidth increase with electron concentration increase. Peak displacement also takes place though by far less amount than in case of Zn-doping. Peak broadening is also far less than in case of Zn-doping. In this case Raman scattering cannot be considered as volume excitation. The skin-layer is about 15 mmk and therefore it is more reasonable to speak of scattering characterizing near-to-surface layer. Besides, as shown in [6], at excitation with the energy mentioned above, RRS, occurring with direct band gap mechanism, is started. Raman spectra for the same samples have been recorded also in conditions of volume excitation with 632.8 nm

(1.98 eV) and 568.2 nm (2.18 eV) wavelengths. In all three cases plasmon-phonon interaction picture (small shift of LO phonon's peak frequency and halfwidth's broadening) is invariable; LO phonon halfwidth for semi-insulating GaP is 1.8 cm^{-1}, whereas for n-GaP with electron concentration $2.2 \cdot 10^{18}$ cm^{-3} halfwidth is 3.8 cm^{-1}.

Fig.2 shows Raman spectra of p-GaP excited by krypton laser wavelength $\lambda_L = 568.2$ nm (2.18 eV), argon laser emission $\lambda_L = 457.9$ nm (2.708 eV) and helium-cadmium laser wavelength $\lambda_L = 441.6$ nm (2.808 eV). Spectra excited with other wavelengths are not shown in the above figure.
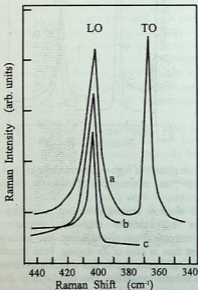
Fig.2. Raman spectra of Zn-doped (p=6.9·10^{18} cm^{-3}) GaP; excitation: a-568.2, b-457.9, c-441.6 nm.

The aforecited experimental spectra show that the halfwidth of plasmon-phonon interaction peak of high frequency positive branch has narrowed by shortening of exciting laser wavelength, i.e. by high energy laser quanta excitation. We were the first to reveal the mentioned effect in GaP [7].

Fig.3 shows a graph plotted on the ground of the above experimental data. It shows clearly the effect we, the first, have revealed in GaP, namely, sharp decrease of halfwidth of LO phonon permitted by Raman scattering selection rule proportionally to exciting laser wavelength shortening. This effect is expressed especially distinctly in p-GaP being enhanced near the first forbidden band E_1 at RRS. We think the mentioned effect to be bound up with electron depletion layer formed by surface electric field induced by surface space electric charge. To prove the consideration, peculiarities of electric field induced Raman scattering (EFIRS) in GaP have been studied. It should be noted that surface electric fields' effect on Raman scattering has been widely studied almost for all semiconductors of A^3B^5 type, especially for GaAs. Exception is only GaP; the reason of it lies in surface peculiarities of GaP.
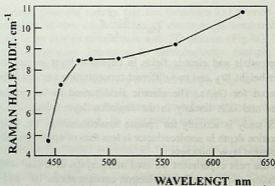
Fig.3. Dependence of LO phonon halfwidth upon exciting laser wavelengths.

Generally at a semiconductor crystal surface always exists internal electric field, which is the result of carrier space charge layer at the surface. One can consider charge carrier depletion layer in the frame of Schottky barrier model. In this approximation interrelation between surface electric field E_s, Schottky barrier's height Φ_B and concentration of current carriers N is determined by the formula

$$E_S = 2 \cdot \left(\frac{2\pi \cdot \Phi_B \cdot N}{\varepsilon} \right)^{1/2}, \qquad (3)$$

where ε is static dielectric susceptibility of semiconductor. In contrast to a dielectric, when it is placed in external electric field, the electric field in semiconductor depletion layer is not constant through the overall width Z_d of depletion layer, which is expressed as

$$Z_d = \left(\frac{\varepsilon \cdot \Phi_B}{2\varepsilon \, e^2 \cdot N} \right)^{1/2}, \qquad (4)$$

and the surface charge is

$$Q_{SC} = \frac{\varepsilon \cdot E_S}{4\pi}. \qquad (5)$$

Potentials and electric fields in depletion layer in case of fixed barrier height Φ_B and two different concentration carriers N has been computed for GaAs. The electric field turned to be maximum at surface and falls linearly in the depletion layer width Z_d. Hence, EFIRS study is actually for opaque semiconductors, i.e. when light penetration depth in semiconductor is less than or approximately equal to depletion layer thickness.

In the next experiment we used monocrystal of n-GaP with (110) orientation and two different electron concentrations 10^{16} and $5 \cdot 10^{17}$; we used 441.6 nm wavelength to excite Raman-spectra and recorded Raman-spectra of these semiconductors at room temperature (Fig.4).
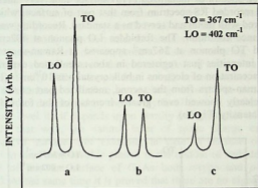
Fig.4. Raman spectrum from (110) surface of GaP at 441.6 nm excitation: a – n = 10^{16} cm^{-3}; b - $5 \cdot 10^{17}$ cm^{-3}; c - $4 \cdot 10^{18}$ cm^{-3}

It is seen from the spectra that the forbidden LO phonon is of weak intensity at low concentration of electrons in semiconductor (10^{16}) and is far less in comparison with TO phonon (Fig.4a). When electron concentration increases in semiconductor (sample with electron concentration $5 \cdot 10^{17}$), its Raman-spectrum shows clearly that the forbidden LO phonon intensity increases sharply (Fig.4b).

Thus, in resonance conditions, when exciting (110) electron-doped surface of GaP, LO phonon forbidden by law of symmetry is observed in Raman spectrum and its intensity increases with electron concentration increase.

Quite different picture is observed when recording Raman-spectra of a p-type GaP at 441.6 nm excitation. In this case, when hole concentration is $4 \cdot 10^{18}$ cm^{-3}, the forbidden LO phonon intensity in Raman-spectra recorded from (110) surface is far weaker, than in case of n-type GaP, when electron concentration is 10^{16} cm^{-3}. That is shown in Fig.4c.

Raman-spectra of metallized (110) surface look very interesting. First we recorded RS-spectrum from that part of surface, which was not covered with metal and served as a standard. Recording was made in resonance condition. The forbidden LO phonon at 402cm⁻¹ and permitted TO phonon at 367cm⁻¹ appeared in Raman-spectra with ratio of intensities just registered in abovementioned experiments, when concentration of electrons in bulk crystal was 10^{16}cm⁻³. (Fig.5a). Then Raman-spectra from the second, metallized part of the (110) surface clearly showed even greater increase of the forbidden LO phonon intensity (Fig.5b).
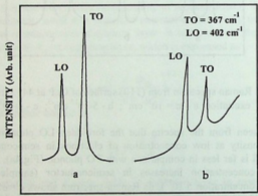
Fig.5. Raman spectrum from (110) surface of GaP at 441.6 nm excitation and free carrier concentration 10^{16} cm⁻³: a-without aluminum covering; b-with aluminum covering.

Thus the experiments we first have carried out for GaP to study surface field effect on the mentioned crystal Raman-spectra, give experimental results as follows: Raman-spectra from (110) surface of n-type GaP hardly show the forbidden LO phonon when electron concentration is equal to 10^{16}cm⁻³; the intensity of the forbidden phonon increases sharply when electron concentration in bulk crystal increases and becomes $5 \cdot 10^{17}$cm⁻³; This intensity increases more when

we cover this surface with semitransparent aluminum layer; in case of a p-type GaP when hole concentration is $4 \cdot 10^{18}$, the intensity of forbidden LO phonon is very small. In all cases the intensity of TO phonon permitted by selection rules is constant; the mentioned effects become apparent clearly only at resonance Raman scattering.

In doped semiconductors the concentration of current carriers at surface generally differs sharply from bulk concentration, which is caused by existence of surface space charge layers. The structure of these layers is determined by the Fermy level state at surface, while the Fermy level itself depends upon density and character of surface states. In that way, the natural layer of space charge expresses properties of surface. For example, in case of surface of GaAs polished in air, Fermi level is pinned in the middle of forbidden gap. Because of this the surface of GaAs both n-type and p-type is depleted. At the same time it is proved that there are no eigen surface states on (110) surface of very pure GaAs, polished or cleaved in high vacuum, which could be arranged in bulk forbidden gap. Band bending is not formed on such surfaces and accordingly there is no pinning of Fermi level at all.

Among A^3B^5 group semiconductors GaP is the only one, surface levels of which may be exist in conditions of high vacuum. Therefore it is rather difficult to interpret EFIRS theoretically for the mentioned semiconductor, but it is necessary to accumulate certain experimental data.

Skin-layer is about 500 nm for 441.6 nm wavelength in GaP. Schottky barrier width in A^3B^5 semiconductors changes from about 2000Å to 150Å when current carriers concentration changes from 10^{16} to $5 \cdot 10^{18}$ accordingly. So, during all of our experiments light penetration distance is much more than depletion layer thickness. The fact has not been found in any EFIRS experiments yet. Our measurements for indirect gap GaP were made in resonance conditions at direct E_1 gap. In such conditions absorption factor α at 441.6 nm is 2000 cm^{-1} and skin-layer accordingly is large. I.e. in fact we are registering resonance Raman-spectra from two layers, one of which is wide, about 500 nm, but LO phonon is forbidden from this layer and there will be no signal. As to the second layer, the width of which is defined from (4) and is various according to carrier

207

concentration but not exceeds a few hundred Angstroems, resonance Raman-spectra are constantly registering forbidden LO phonons of great intensity. Therefore, on the base of abovementioned experimental facts we connect this phonon induction mainly with surface electric field. Sharp increase of forbidden LO phonon intensity from GaP (110) surface covered with aluminum layer speaks in favor of this mechanism.

So, in conditions of Resonance Raman scattering the peculiarities of plasmon-phonon interaction have been studied in GaP. Absolutely new two experimental facts have been fixed for GaP after studying free carriers' influence on GaP phonon spectrum with surface excitation, especially in conditions of resonance Raman scattering: a) above mentioned is manifestation of allowed LO phonon of Raman scattering, non-interacting with free carriers from depletion layer of (001) surface of p-GaP; b) discovering of forbidden LO phonon of Raman scattering in resonance conditions from (110) surface of n-GaP induced by surface electric field of surface space charge.

REFERENCES

1. D. T. Hon and W. L. Faust. Appl. Phys. 1, 1973, 241.
2. M. Giehler and E. Jahne. Phys. Stat. Sol. (b) 73, 1976, 503.
3. V.Kh. Vairamov. Fizika Tverdogo Tela. 19, 1977, 455.
4. G. Irmer, V. V. Toporov, B. H. Rairamov, and J. Monecke Phys. Stat. Sol. (b) 119, 1983, 595.
5. S. Gotoshia. Bull. of Georg. Acad. of Sci. 159, 2, 1999, 241.
6. S. Gotoshia. Bull. of Georg. Acad. of Sci. 171, 3, 2005, 468.
7. S. V. Gotoshia, L. V. Gotoshia. Bull.of Georg. Acad. of Sci. 172, 3, 2005, 442.

*Georgian Academy of Sciences
Institute of Inorganic Chemistry and lectrochemistry
** Tbilisi State University

ს. გოთოშია, ლ. გოთოშია

დენის თავისუფალი მატარებლების ოპზიკურ ფონონებთან ურთიერთქმედებისა და ზედაპირული სიერცით მუხტის ფორონის სპექტრზე ზეგავლენის შესწავლა GaP-ში ლაზერული რამან სპექტროსკოპიით

დასკვნა

პლაზმონ-ფონონური ურთიერთქმედება A^3B^5 ტიპის ნახევარგამტარებში ფართოდაა შესწავლილი. რამოდენიმე შრომაში ეს მოვლენა შესწავლილია GaP-ში, მაგრამ მხოლოდ მოცულობითობი ადგილებში. პლაზმონ-ფონონური ურთიერთქმედება GaP-ში შესწავლილი ზედაპირული ადგილებში, ოანდა - მენანასყრუ პირობებში. ამ მიდგომით, ნაო, რომ პლაზმონს LO - ფონონის ურთიერთქმედების მახასიათებელი სპექტრალური ხილის ნახევარსიგანე, როგიც მოცულობითობ ადგილებისას ფართოდგებით, დენის თავისუფალი მატარებლების კონცენტრაციის ხრდით, ანისაულ დაყოვროდება ადგსილრ ლაზარის ტალდერის სიერცის დამოკიდებილი. ეს ეფუძნა, რომდანვუ ვუურ გამოხდებუ გიხვა რეჭონანსუუ რამანის გაბეგვისას E_1 ზონის მახლობლობაში, ჩვენ პირევდება დღასო ორუკიქართდ GaP-ში (001) ზედაპირიდ.

ჩვენ მოსახსურებაის ხელასაფტ ვენატდ შესასწავლად რამანის გაბახ (110) ზედაპირდანა. ამ შემხვეჭვებაბი პირველ თდეზებია ადმითდიად, რომ GaP-ს (110) ზედაპირ შერბელდ კანანო აკრდაცდელდ LO ფონონის ინტების მკვეთრად გაიხარდა მოცულობითობ დენის თავისუფალ მატარებლების ხდოსია. ეს ეფუძნა განას კვიო ურურ გამლოდებ, როგცისა (110) ზედაპირდ დავამოდათ ნახვდდგამტულდ მეტების მეტ ხეშა დდნ.

ორივე ახალი ახმდნიდ ექსპანდიდებ ფაქტი ადასტრდ ჩვენ მოსახზად, რომ შდშშ უნს ახსნას რამანის გაბებდგ GaP-ს ზედაპირობ სიერცით

მუხტის ფენით ინდუცირებული ზედაპირული ელექტრულად ვეღარ ხdაადgენთ. შედეგად, ზედაპირის გარკვეულ სიღრმეზე წარმოიქმნება დენის თავისუფალი მატერებლების გადარჩება დენა, რაც ბუნებრივია, იწვევს ამ ფენიდან მხოლოდ სუფთა ფორონული ზოლის დაიზრგა, რომლიდც არცა გაფართოებული პლაზმონურ რხევებთან ურთიერთმოქმედებ.

ONE OF THE WAYS OF THE SOLUTION OF SCHRÖDINGER EQUATION FOR THREE PARTICLES SYSTEMS WITH INVERSE SQUARE PAIR POTENTIAL

A. Lomidze

ABSTRACT. In accordance with the solution of Schrödinger equation for three-particle system with inverse square distance dependent pair potential the bound state is not realized at all i.e. the ground state energy equals to -∞, which is physcaly meaningless. The reason of this fact is that the potential is critically singular.

The article studies how to solve Schrödinger equation for three particle system of inverse square distance dependent pair potential by modified hyperspercial function method (MHFM) that gives Hamiltonian corresponding to Schrödinger equation and at the same time includes the similar to the Coulomb potential and critically singular potential. The solution of the Schrödinger equation, which includes this kind potential with corresponding boundary conditions is given in any quantum mechanical book. This solution has been given exact physical results and shown that, in the first approximation binding energy of the system changes monotonically by global quantum number.

However, as we remarked above, in this case similar to the Coulomb potential appeared in Schrödinger equation. So the result does not correspond to the initially studied system (only to the inverse square distance dependent pair potential for three particle system).

1 INTRODUCTION

A number of physical phenomena can be described by singular potentials [1-9], and especially interesting among them is the inverse square distance dependent pair potential (critical singular potential), because it can be used as independently as with the other power singular potentials [10-14] in different areas of physics.

Schrödinger equation for two particle system with such potential has been studied in ref. [15,16].

Solution of Schrödinger equation with critically singular potential can be achieved by renumbering method, which initially had been formed by Wilson [17], when he carried out calculation by the quantum field theory and the renumbering the inverse square potential has become the parameter cutoff. This parameter cutoff used to inverse square potential has got not only physical result [16,18] but also possibility to explain the break of quantum anomaly and its experimental results [19] (where was observed interaction between dipole and electron.). In spite of that the inverse square potential system was limited: 1) by two particle systems in ND space, when N ≥ 1; 2) by three and multi-particle systems in 1D space.

So the investigation of three particle-system as independent critical singular potential and with its other power singular potentials in 2D and 3D spaces will extend knowledge and it will be more precise definition about this potential and also will extend the sphere of use of this potential.

2 FORMULATION OF THE PROBLEM

We considered the potential of inverse square distance dependence (critical singular potential):

$$V(r) = a \cdot r^{-2}. \qquad (1)$$

The radial parts of Schrödinger equation with two-particle system (1) is following:

$$R'' + \frac{2}{r}R' + \frac{\lambda}{r^2}R + k^2R = 0, \qquad (2)$$

where R is a radial part of a wave function:

$$\lambda = \frac{2\mu\beta}{\hbar^2} - \ell(\ell+1)$$

and if $V(r) \sim 1/r^2$ was in whole space, then bound state was not realized in case of - $\lambda < 1/4$ at all. And when $\lambda > 1/4$, a particle "falls into the center" (ground state energy equals to $-\infty$) and so it is physically meaningless [15,16].

In ref. [20,21] three particle system has been studied with pair of interaction of the same expression (1) between particles. Hyperspecial function method has been used [22]. However, after using this method we obtained system of the coupled differential equations. Let us consider one equation from this system for the hyperradial wave function in 2D [20] and it is expressed as follows:

$$\left(\frac{\partial^2}{\partial \rho^2} + \frac{3}{\rho} \frac{\partial}{\partial \rho} - \left[\chi^2 + \frac{K(K+2)}{\rho^2} \right] \right) \chi_K(\rho) = \frac{2\mu}{\hbar^2 \rho^2} J_K \chi_K(\rho), \quad (3)$$

where K – is the particles hypermoment.

$$\chi^2 = -\frac{2\mu}{\hbar^2} E$$

if define λ as follows:

$$\lambda = -K(K+2) - \frac{2\mu}{\hbar^2} J_K$$

(3) and (2) are analogous. If $V(r) \sim 1/r^2$ is in the whole space then bound state is not realized in case of $\lambda < 1$ at all. And when $\lambda > 1$ a particle "falls into the center" (ground state energy equals $-\infty$) and so it is physically meaningless.

From [21] paper is clear that after using this method only in the first approximation from infinitely continued equation system for the hyperradial wave function in 3D is as follows:

$$\left(\frac{\partial^2}{\partial \rho^2} + \frac{5}{\rho} \frac{\partial}{\partial \rho} - \left[\chi^2 + \frac{K(K+4)}{\rho^2} \right] \right) \chi_K(\rho) = \frac{2\mu}{\hbar^2 \rho^2} J_K \chi_K(\rho), \quad (4)$$

213

if we define λ as follows:

$$\lambda = -K\left(K + 4\right) - \frac{2\mu}{\hbar^2} J_K,$$

(4) and (2) are analogous. But if $V(r) \sim 1/r^2$ was in the whole space then bound state was not realized in case of $\lambda < 4$ at all. And when $\lambda > 4$ then a particle "falls into the center" (ground state energy equal to ∞) and so it is physically meaningless.

So despite existence of solutions of (3) and (4) equations characterized the solution of Schrödinger equation corresponding to two-particle systems we have got for them an unbound system or physically meaningless.

So the problem solution by Schrödinger equation for three-particle system which contains (1) potential where the non-model approach can be used must be very interesting.

It has been investigated three particle system with the same potential using of modified hyperspherical function method [4-6] (see chapter 3) that gives Schrödinger equation with corresponding Hamiltonian including the same Coulomb potential. So as a result of using MHFM on three-particle system in 2D space with first approximation the following equation was obtained:

$$\left(\frac{\partial^2}{\partial \rho^2} + \left(\frac{3}{\rho} - W_2'\right)\frac{\partial}{\partial \rho} + \frac{3W_2' + W_3'}{\rho} + \right.$$
$$\left. + \left(x^2 + W_6'\right) - \frac{2\mu}{\hbar^2}\frac{K(K+2) + J_0}{\rho^2}\right)\psi(\rho) = 0 \quad (5)$$

(all quantity is given in chapter 3).

From (5) it is clearly seen that it includes the same Coulomb potential (the third component in the bracket).

Analogically MHFM on three particle system in 3D space was used and as a result we have got:

214

$$\left[\frac{\partial^2}{\partial\rho^2}+\left(\frac{5}{\rho}-W_2'\right)\frac{\partial}{\partial\rho}+\frac{3W_2'+W_3'}{\rho}+\right.$$
$$\left.+\left(\kappa^2+W_6'\right)-\frac{2\mu}{\hbar^2}\frac{K(K+1)+J_0}{\rho^2}\right]\psi(\rho)=0 \quad (6)$$

(all quantities in equation have been explained in chapter 3).

Also from (6), it is clearly seen that it includes the same Coulomb potential (the third component in the bracket).

Corresponding to boundary conditions solution of Schrödinger equation with Coulomb potential is given in any quantum mechanical book. Solutions of (5) and (6) equations are given in [20,21].

The solution had taken into account asymptote behavior of solution. In particular, when $\rho \to 0$ the solution has been found with $\Psi \sim \rho^\sigma$:

$$\sigma=-2+\left[(K+2)^2-\frac{2\mu}{\hbar^2}J_0\right]^{1/2} \quad \text{in 3D space;} \quad (7)$$

$$\sigma=-1+\left[(K+1)^2-\frac{2\mu}{\hbar^2}J_0\right]^{1/2} \quad \text{in 2D space.} \quad (8)$$

Here and later on (for (18) and (19) the same expressions are being obtained) it should be taken into account that interaction constants in three particle system is negative when $a_{ij}<0$, (calculation of Jo in 2D and 3D spaces given in [20,21]). As seen from appendix, Jo was negative for any negative value of a_{ij}. Though in (7) and (8) equations the expression under root will be positive for any negative values of a_{ij}. The expressions of bound state energy of system was as following:
in 2D space

$$E_N=\frac{\hbar^2}{8\mu}\left[\left(\frac{12W_2'+4W_3'-W_2'^2(3+2\sigma-2N)}{3+2\sigma-2N}\right)^2-W_2^2+4W_6'\right] \quad (9)$$

and in 3D space

$$E_N = -\frac{\hbar^2}{8\mu}\left[\left(\frac{12W_4' + 4W_5' - W_2'(2\alpha + 5 - 3N)}{2\alpha + 5 - N}\right)^2 - W_2'^2 + 4W_6'\right]:\quad (10)$$

The solution obtained from (9) and (10) by Schrödinger equation, in first approximation, has shown that binding energy of the system changes monotonically according to global quantum number.

Although bound state energies of three-particle system obtained using MHFM are finite and not meaningless, the question is how real they are.

3 PROBLEM SOLUTION

The main idea of the modified hyperspherical function method (MHFM) [4-6] is that the wave function is Ψ presented as the product of two functions, where the first is the main hyperspherical function and the second is the "correlation function" - $\zeta = \exp(f)$ that defined by singularity and clustering properties of the wave function and it is equal to:

$$f = -\sum_{i=1}^{3}\gamma_i r_i,\quad (11)$$

where r_i is a distance between the particles and γ_i is determined according to physical considerations. Considering relation between the three different sets of the given in [22] Jacob's coordinates, (11) could be rewritten as following:

$$\sum_{i=1}^{3}\gamma_i z_i = \rho(G_1\cos\alpha + G_2\sin\alpha),\quad (12)$$

where

$$G_1 = \gamma_1 + \gamma_2\cos(\phi_{23} + \phi_{31}) - \gamma_3\cos\phi_{31};$$

$$G_2 = \gamma_2\sin(\phi_{23} + \phi_{31}) - \gamma_3\sin\phi_{31}.\quad (13)$$

ϕ_{23}, ϕ_{31} — angles were defined by [22]. Taking into account the above and simple transformations we obtained Schrödinger equation in 2D space (5), where

$$W_2' = (G_1 - G_2) \cdot \frac{21\sqrt{6}}{8}; \qquad W_6' = G_1^2 + G_2^2;$$

$$W_3' = W_2' + 21\sqrt{6}\,(0.25G_1 + G_2) \qquad (14)$$

and in 3D space (6), where

$$W_2' = (G_1 - G_2) \cdot \frac{4}{15}; \qquad W_6' = G_1^2 + G_2^2;$$

$$W_3' = G_1 \left(\frac{4}{15} - \frac{3\pi}{8} \right) - \frac{42}{105} G_2. \qquad (15)$$

As we already have denoted, application of hyperspherical function modified method for three particle-system carried out with (1) type pair interaction (as it is given in previous chapter for 2D and 3D spaces) gives Schrödinger equations that are similar with effective Hamilton potentials including the potential similar to Coulomb's potential.

[23] was regards in 3D space with pair interaction:

$$\left(\frac{a}{r^2} + \frac{b}{r} \right). \qquad (16)$$

This equation can be exactly solved by Schrödinger equation without MHFM.

Without MHFM, bound energy in 2D and 3D space is obtained analytically:

$$E = -\frac{\hbar^2}{2m} \left(\frac{V_c}{2N + 2\lambda} \right)^2, \qquad (17)$$

where

217

$$\lambda = \frac{1}{2} + \sqrt{(K+1)^2 + W_1} \; ; \quad \text{(in 2D space)};$$

$$\lambda = \frac{1}{2} + \sqrt{(K+2)^2 + W_1} \; , \quad \text{(in 3D space)};$$

$N = (\lambda + W/(2\chi)); \; V_c$ and W_1 are the values of the calculating results the similar of the Coulomb potential and the square inverse potential related with an angular (arc) integral.

Using MHFM for (16) potential the Schrödinger equation of three particles system with pair interaction between particles has been obtained in 2D space

$$\left(\frac{\partial^2}{\partial \rho^2} + \left(\frac{3}{\rho} - W_2' \right) \frac{\partial}{\partial \rho} + \frac{3W_2' + W_3' - V_c}{\rho} + \right.$$
$$\left. + \left(\chi^2 + W_6' \right) - \frac{2\mu}{\hbar^2} \frac{K(K+2) + J_0}{\rho^2} \right) \Psi(\rho) \qquad (18)$$

and in 3D space [23]

$$\left(\frac{\partial^2}{\partial \rho^2} + \left(\frac{5}{\rho} - W_2' \right) \frac{\partial}{\partial \rho} + \frac{3W_2' + W_3' - V_c}{\rho} + \right.$$
$$\left. + \left(\chi^2 + W_6' \right) - \frac{2\mu}{\hbar^2} \frac{K(K+1) + J_0}{\rho^2} \right) \Psi(\rho) = 0, \qquad (19)$$

where the marks explained in (14) and (15) and $V_c = \frac{2\mu}{\hbar^2} \chi$; Behavior of (18) and (19) were still defined by (7) and (8), where the expression under root was did not depend on b, because b depends only on J_1. J_1 — is the value of the calculation result of an angular (arc) integral related to the second component of expression (16):

$$J^{l_1 l_2 l_3}_{K K' L L' M M'} = \int \Phi^{* l_1 l_2}_{KLM} (\Omega_1)(b_{12} \eta_{12}^{-1} + b_{13} \eta_{13}^{-1} + b_{23} \eta_{23}^{-1}) \Phi^{l_1 l_2}_{K' L' M'} (\Omega_1) d\Omega$$

in the first approximation.

In solution of (18) and (19) account has been taken of an asymptote behavior of the solution, in particular when $\rho \to 0$. Then solution has been found with $\Psi \sim \rho^\sigma$ where σ in 2D and 3D spaces expressed by (7) and (8) relationships. From (7) and (8) it is clearly seen that the expression under root does not depend on constant (b_{ij}).

Solution of (18) and (19) equations gives some of the bound expressions in 2D space:

$$E_N = -\frac{\hbar^2}{8\mu}\left[\left(\frac{12W_2' + 4W_3' - 4V_C - W_2'(3 + 2\sigma - 2N)}{3 + 2\sigma - 2N}\right) - W_2' + 4W_6'\right] \quad (20)$$

in 3D space:

$$E_N = -\frac{\hbar^2}{8\mu}\left[\left(\frac{4(3W_2' + W_3' - V_c) - W_2'(2\sigma + 5 - 3N)}{2\sigma + 5 - N}\right)^2 - W_2' + 4W_6'\right] \quad (21)$$

Bound energy calculated from (17), (20) and (18), (21) [21] related on global quantum number is shown in Table (see Table).

In result it was assumed that all particles' masses equal to the mass of electron. Parameter of correlation - $\gamma_i = 0.01$ (i = 1,2,3), the constants of interaction are the same, so $a_{ij} < 0$ and $b_{12} = b_{13} < 0$, $b_{23} > 0$, and various from 1 to 0.001 does not give qualitatively new results.

The results entered in table are true for a_{ij} in (-1, -0.001) interval. Pair' potential of the inverse square of the distance with repulsion interaction constants between particles (when $a_{ij} > 0$) was not considered in this paper and needs research in future. As regards to b_{ij} calculation had been made in case when they change according with modules in (1; 0.001) interval and satisfy the conditions: $b_{12} = b_{13} < 0$, $b_{23} > 0$. For other values are not studied and needs research in future too.

	2D space		3D space	
N	-E(compar.unit) formula (17)	-E (compar.unit) formula (20)	-E(compar.unit) formula (17)	-E(compar.unit) formula (21)
0	4.866238	4.7093248	3.3156439	0.304168
1	2.415242	2.3599785	0.1264723	0.123532
2	1.439093	1.413575	0.067679	0.066523
3	0.954168	0.9403576	0.042062	0.041494
4	0.678661	0.6703626	0.0286507	0.028331
5	0.507292	0.5019224	0.0207633	0.020566
6	0.393497	0.3898247	0.0157354	0.015605
7	0.314101	0.3114802	0.0123351	0.012244
8	0.256518	0.2545822	0.0099287	0.009863

Results obtained by calculation let us think that Schrödinger equation with (16) potential does not change its character by using MFHM. However, it can be used for the Schrödinger equation of these particle system for (16) pair interaction and not for (1) interaction. So we can give the answer to the equation in chapter two: 1) yes, only for (16) potential when a_{ij} is changing in (-1; -0.001) interval and satisfied $b_{12} = b_{13} < 0$, $b_{23} > 0$ condition; 2) no, for (1) potential. So the values of bound state energy of three particle system when we used MFHM is real and has physical meaning only for (16) potentials.

4 CONCLUSIONS

The solution of three particles system of Schrödinger equation has given the following results:

1) Similar to (16) expression the pair interaction between the particles with MFHM and without MFHM (in first approximation) show that the binding energy of system dependence on the global quantum number in both cases are equal with great precision (therefore MFHM does not change quality of Schrödinger equation) when a_{ij} coefficients change interval is (-1; -0.001) and b_{ij} coefficients change interval is (1; 0.001) with condition $b_{12} = b_{13} < 0$, $b_{23} > 0$;

2) In order to obtain physically meaningful solution MFHM is applied to only two types of pair potentials: I. Critically singular

potential; II. The sum of critically singular and Coulomb like potentials.

We have obtained that the calculated binding energy monotonously depends on the global quantum number.

3) By similar to (16) pair interaction between particles studied using MFHM in 2D and 3D spaces it was shown that with application of MFHM the solution of Schrödinger equation containing corresponding Hamiltonian to obtain the solution with physical meaning is possible.

4) By similar to (1) pair interaction between particles studied by MFHM in 2D and 3D spaces it was shown that solution of Schrödinger equation containing Hamiltonian is possible, but during solution there appears a component similar to Coulomb potential. Hence, we should not think that the obtained results correspond to the initially given investigated system (only inverse square distance dependent pair potential three-particle system).

5. APPENDIX

Jo included in conditions (7) and (8) (similar to those obtained for (18) and (19)) represents the following expression:

$$J_o = \frac{\sqrt{3}}{2}\left(a_{12}J_{12} + a_{13}J_{13} + a_{23}J_{23}\right). \tag{d1}$$

As for J_{12}, the analogous have the others) it equals to:

$$J_{12} = \int \Phi_K^*(\Omega)\Phi_K(\Omega)(\cos\alpha)^{-2}\,d\Omega, \tag{d2}$$

where

$$\Phi_K(\Omega) =$$
$$= N_K^{l_1,l_2}\cos^{l_1}\alpha.\sin^{l_2}\alpha \; P_n^{l_1+1/2,l_2+1/2}(\cos 2\alpha) \; Y_{l_1m_1}(x)Y_{l_2m_2}(y) \; \delta \tag{d3}$$

$P_n^{l_1,l_2+1}(\cos 2\alpha)$ –Jacob polynomial; $Y_{l_1m_1}(x)$ –spherical function;

$$N_K^{l_1 l_2} = \left(\frac{2n!(K+2)(n+l_1+l_2+1)!}{\Gamma(n+l_1+3/2)\Gamma(n+l_2+3/2)} \right)^{1/2} ; \quad n = \frac{K-l_1-l_2}{2}$$

putting (d3) in (d2), and taking into account that the work considers only the first approximation ($K = K' = 0$, $l_1 = l'_1 = l_2 = l'_2 = 0$), some transformations give:

$$J_{12} = \frac{20!21!}{[\Gamma(3/2)\Gamma(3/2)]} \left[\frac{\Gamma(3/2)}{\Gamma(1)\Gamma(3/2)} \frac{\Gamma(3/2)}{\Gamma(1)\Gamma(3/2)} \right]^2$$

$$2^0 (-1)^2 \frac{1}{2} \frac{\Gamma(3/2)\Gamma(1/2)}{\Gamma(2)} \qquad (d4)$$

(d4) shows that, $J_{12} > 0$ (J_{13} and J_{14} are analogous). It follows from the (d1) J_s sign depends on the sign of constants of interaction between panicles. In the paper only the case, when constant of interaction $a_{ij} < 0$ is considered, also notes that the work considers the case $J_s < 0$.

ACKNOWLEDGEMENT

REFERENCE:

1. A. Galindo and P. Pascual, Quantum Mechanics I, Springer-Verlag, Berlin, Germany, 1990.

2. R. Jackiw, in M. A. B. B'eg Memorial Volume, A. Ali and P. Hoodbhoy, eds. World Scientific, Singapore, 1991.

3. S. Albeverio, F. Gesztesy, R. Høegh-Krohn, and H. Holden, Solvable Models in Quantum Mechanics. Springer-Verlag, New York, 1988.

4. M.I.Haftel and V.B.Mandelzweig. Ann. Phys. 189, 1, 1989, 29.

5. Fabre de la Ripelle, Ann. Phys. 147, 2, 1982, 281.

6. A.M.Gorbatov, A.V.Bursak, Yu.N.Krilov, and B.V.Rudak. Yad. Fiz. **40**, 1984, 233.

7. W.M.Frank, D.Land, R.M.Spector. Rev. Mod. Phys. **I.43**, 1971, 36.

8. D. Emin, T. Holstein. Phys. Rev. Lett. **36**, 1976, 323.

9. S. Coleman, "Aspects of Symmetry" selected Erice Lectures (Cambridge Univ. Press, Cambridge, 1988), 234.

10. N.F. Johnson, L.Quiroga. Analytic rezults for N particles with $1/r^2$ interaction in two dimensions and an external magnetic field. (cond-mat/9504025).

11. Shi-Hai Dong, Zhong-Qi Ma, Giampiero Esposito. Phys.Lett. **12**, 1999, 465, (quant-ph/9902081).

12. A. Khare, R. K. Bhaduri. J. Phys. **A27**, 1994, 2213, (hep-th/9310103).

13. B. Basu-Mallick, K. S. Gupta. Phys. Lett. **A292**, 2001, 36, (hep-th/0109022).

14. P. K. Ghosh, K. S. Gupta. Phys.Lett. **A323**, 2004, 29, (hep-th/0312376).

15. P.M. Morse, H. Feshbach. Methods of Theoretical Physics. **I**, **II**. New York McGraw-Hill. 1953.

16. K.G.Gupta, S.G.Rajeev. Phys. Rev. **D48**, 1993, 5940. (hep-th/9305052)

17. K. G. Wilson. Phys. Rev. **B4**, 1971, 3174.

18. B. Basu-Mallick, Kumar S. Gupta. Phys.Lett. **A292**, 2001, 36, (hep-th/0109022).

19. H. E. Camblong, L. N. Epele, H. Fanchiotti, and C. A. Garcia Canaf. Quantum anomaly in molecular physics, (hep-th/0106144).

20. A.Lomidze, Sh.Tsiklauri. Proceedings of I. Javakhishvili Tbilisi state university. Physics. **38**, 2002, 154.

21. A.M. Lomidze, Sh. M. Tsiklauri. Bulletin of the Academy of Sciences of the Georgia. **159**, 1, 1999, 52.

22. R.I.Jibuty and N.B.Krupennikova. The Hyperspherical Functions Method in Few - Body Quantum Mechanics. Mecniereba, Tbilisi, 1984, (Russian).

23. A.Lomidze. Proceedings of I. Javakhishvili Tbilisi State University. Physics, **39**, 2004, 192.

ა. ლომიძე

მანძილის კვადრატის უკუპროპორციული წყვეული პოტენციალით შემავალი სამნაწილაკოვანი სისტემის შრედინგერის განტოლების ამოხსნის ერთ-ერთი გზის შესახებ

მანძილის კვადრატის უკუპროპორციული წყვეული პოტენციალის მქონე სამნაწილაკოვანი სისტემის შრედინგერის განტოლების ამოხსნის ამ ჯგუფისა, რომ ბაუ ... მდგომარეობის საერთოდ არ ხორციელდება ამ ძირითადი მდგომარეობის ენერგია ტოლია - ∞, რაც ფიზიკურად უაზროა. ამის მიზეზი არის ის, რომ პოტენციალი კრიტიკულ- და სინგულარულია [1-3].

ნაშრომში შესწავლილია მანძილის კვადრატის უკუ-პროპორციული წყვეული პოტენციალით შემავალი შრე-დინგერის განტოლების ამოხსნის ჰიპერსფერული ფუნქცი-ის მოდიფიცირებული მეთოდის (მ)თ) ამოყენებით [4-6]. რომელიც საზღვდებოდთავსე შრედინგერის განტოლების შესაბამისი ჰამილტონიანის შეიცავს კრიტიკულად სინგუ-ლაართა პოტენციალის ცრის კულონისებრს მსკავდი პოტენციალი, ასეთი პოტენციალით შემავალი შრედინგე-რის განტოლების ამოხსნა შესაბამისი სასაზღვრო პირო-ბების მოცემულ კვადრატში მექანიკის ხუხისთვილ ... სა უ უ ... მ ... ... ამოხსნა იძლევა ხუზუ ფიზიკურუ ფეუდს და მიიღება, რომ ... პოტენციალის სისტემის მსგა ... ...

უუსა რ ... ... უ ... ...

მოცემულ შესასწავლ სისტემას (მხოლოდ მანძილის კვადრატის უკუპროპორციული წყვდიური პოტენციალის მქონე სამნაწილაკიან სისტემას).

CONTENTS

n. 1/63